On-Chip Frequency Control in THz Quantum Cascade Lasers

Inaugural-Dissertation
zur Erlangung des Doktorgrades
der Mathematisch-Naturwissenschaftlichen Fakultät
der Universität zu Köln

Vorgelegt von

MARC RUBEN MERTENS

aus Bergisch Gladbach

I. Physikalisches Institut
Universität zu Köln
2023

Gutachter:
Prof. Dr. Jürgen Stutzki
Prof. Dr. Markus Grüninger

Tag der Disputation: 23.02.2023

Abstract

Several attempts have been made to build terahertz Quantum Cascade Lasers with the capability for frequency tuning exceeding the range accessible by variation of temperature and current, but so far, no technique has been widely adopted. This work investigates a novel approach based on mechanical manipulation of the resonator length. This on-chip approach requires no external optics and could be implemented in a compact setup with micromechanical actuators. A combination of a classical metal-metal QCL with attached waveguide structures based on a benzocyclobutene substrate allows the construction of a movable reflector. In the course of the thesis, lasers are initially designed and simulated using a computer model. After fabrication, the real-world performance is evaluated and compared to simulation results. It is shown that this technique is generally feasible with the best performing device achieving a full free spectral range of continuous tuning (25 GHz) plus another 5 GHz accessible by current tuning. Possible points of improvement are identified, and a second generation of lasers is designed and fabricated. Unfortunately, the second-generation devices suffer from unexpected laser modes that prevent tuning. Nevertheless, in the course of this thesis, the possibility of translating mechanical resonator tuning - usually seen in much larger lasers - to the chip level of semiconductor devices is successfully demonstrated.

Contents

List of Figures

Chapter 1.

Motivation

Astronomical observations at high spectral resolution play an indispensable role in the study of the physical and chemical dynamics of the universe. The ability to identify and resolve atomic and molecular lines in the spectra of celestial objects represents an important piece in the puzzle to understand the processes involved for example in molecular clouds, photon dominated regions, star formation and the interstellar medium in general, but also the investigation of planetary atmospheres, circumstellar outflows or the kinematics and composition of galaxies becomes possible. The parts of the electromagnetic spectrum known as the submillimeter and terahertz regions feature a remarkable abundance of molecular and atomic transitions that drive a strong effort towards the development of astronomical instrumentation for these frequencies.

Heterodyne astronomy is a way to reach unprecedented spectral resolution and is pursued by research groups worldwide, among them the I. Physics Institute of the University of Cologne and the CRC 956[1] therein. A central task in addition to data analysis, laboratory astrophysics and computational simulation is the development of instrumentation, currently focused on by several work groups at the institute. One of the instruments developed, maintained and operated in collaboration with Max Planck Institute for Radio Astronomy is the German Receiver at Terahertz Frequencies (GREAT). Deployed at the Stratospheric Observatory for Infrared Astronomy (SOFIA), the low-frequency channel of this instrument provides the currently only possibility worldwide to observe transitions of [CII], [OI] and other terahertz sources from 1.8 THz to 2.05 THz with velocity-resolved spectral resolution.

A core component of any heterodyne receiver is the local oscillator, a radiation source close in frequency to the observed emission from the astronomical target. Two different sources are currently used in GREAT; the Low-Frequency Array operating around 1.9 THz uses a solid-state multiplier chain based on Schottky diodes that provide

[1] Collaborative Research Centre 956 - a research program funded by Deutsche Forschungsgemeinschaft (DFG).

the required frequency through harmonic upconversion of an amplified synthesizer signal while the High-Frequency Array operating at 4.7 THz takes advantage of the superior output power of a Quantum Cascade Laser (QCL) at such high frequencies. The development of the 4.7 THz Cologne QCL local oscillator is the result of a long and successful cooperation with the Quantum Optoelectronics Group of J. Faist at ETH Zürich, where significant effort was undertaken to provide QCLs of the required frequency and operating parameters. This cooperation also allows the exploration of QCLs intended for the low-frequency channel and makes the work presented here possible. The objective is to provide a more powerful local oscillator source to replace the currently used multiplier chains, removing a bottleneck in the system to improve instrument performance.

Although a QCL local oscillator has already proven successful in the 4.7 THz channel, only the [OI] 63 µm transition is observed there. Therefore a few GHz tuning accessible by current and temperature variations of the laser is enough to cover the redshift and radial velocity of many astronomical targets. This is insufficient for the low-frequency channel since several molecular species with different transitional energies are observed during each flight, so a larger tuning range is required. Such a widely tunable, continuous wave, single mode terahertz QCL has not been demonstrated so far, but the highly valuable observation time with SOFIA justifies a significant effort directed towards this goal.

Apart from the scientific rationale, my personal motivation to pursue this topic also stems from my work in the team of researchers and engineers of GREAT and SOFIA. During my Master's thesis[1] I had the opportunity to be involved in the development of the 4.7 THz Cologne QCL LO[2]. Since its first SOFIA flight in 2018, I have spent many hours in the air and the laboratory, operating and working on the instrument together with scientists from University of Cologne, Max Planck Institute for Radio Astronomy and the Institute of Optical Sensor Systems at DLR [3]. Not as a direct part of, but related to this dissertation in a more general sense, I was able to contribute to the successful observation of astronomical sources investigated within various projects, many of them already published or accepted for publication at the time of finishing this thesis: Okada et al.[4], Schneider et al.[5], Mookerjea et al.[6], Higgins et al.[7], Tiwari et al.[8], Kabanovic et al.[9] and Schneider et al.[10]. On that basis, I believe I am in an excellent position to transfer the gained knowledge to my work on a tunable QCL that fulfills the requirements imposed on a local oscillator for a heterodyne receiver.

Chapter 2.

Introduction

2.1. Quantum Cascade Lasers in the Field of Terahertz Technology

Embedded between the millimeter and infrared part of the electromagnetic spectrum, the terahertz region's potential has been relatively untapped for a long time. Its recent prospering stems mostly from technological progress, since for the longest time, it has been neither accessible to electronic signal processing used to great extents at lower frequencies nor to the optical techniques used in the visible to the mid-infrared regime. Physical constraints often limit these established approaches, and pushing the boundaries into the terahertz region requires the development of new methods. Extension of microwave designs to THz frequencies results in tiny antenna and waveguide dimensions, and even the fastest semiconductors – usually Schottky diodes or high-electron-mobility transistors – become unfeasibly inefficient at high frequencies, with the limit nowadays being at ca. 2000 GHz [11]. Refractive optics at terahertz frequencies have to deal with challenges arising from the optical properties of available materials, notably high losses in dielectrics. Experiments often require additional effort in dealing with environmental difficulties, mainly absorption in the air caused by molecular rotational water vapor lines. The natural variation of air humidity can easily cause an order of magnitude of fluctuation in a THz signal in an open experimental setup if the relevant frequencies are close to a water vapor transition. Encapsulation of the entire beam path in a vacuum vessel is often necessary. The trade-off between small focus spot size and high beam divergence in long wavelength Gaussian optics means that beam-shaping components are often physically large, especially in the lower frequency part.

Overcoming the technological limitations has been a gradual process that brought together diverse physical disciplines, and what is known today as **terahertz science** has a strong footing in the aspiration of researchers worldwide to develop and refine

their available tools to tackle fundamental questions.

This science-driven development of terahertz technology as a compound of various research demands and purposes is reflected in the sometimes blurred definition of the associated spectral range itself. The exact numbers change depending on author and publication, but a reasonable value for definition is 100 GHz to 30 THz [12]. On a side note, also the name given to this region changed over time: Initially it was commonly called sub-millimeter waves or the Far Infrared until more recently the literature seems to have settled on the label *terahertz*.

The physical phenomena observable in the terahertz range are manifold, including rotational (and sometimes vibrational) molecular transitions [13], hydrogen bond resonance [14], thermal radiation from cold interstellar dust, phonon excitation in solids [15], control of Rydberg states in semiconductors [16] and antiferromagnetic spin waves [17].

A term encountered in the field recently is *filling of the terahertz gap* which describes its delayed catch-up compared to the historically faster progress in the surrounding parts of the electromagnetic spectrum. Technological advancements and breakthroughs, especially in the area of sources and detectors, now enable experimental techniques formerly exclusive to infrared or radio frequencies, including time domain sampling, heterodyne detection and laser sources. The growth of knowledge from laboratory research or astronomical observations and our understanding of the underlying physical processes and conditions - e.g. chemical composition and velocity distribution in astronomical sources - is enabled predominantly by this technological advance.

Many steps in the effort to close this "terahertz gap" in a way that allows for widespread adoption in academic research and commercial application have only been done after around 1990, but naturally, experiments have been performed long before that and sophisticated methods for generation and detection emerged soon after the concept of electromagnetic waves gained acceptance. At the turn of the century, the most prominent figure in the field was probably Heinrich Rubens, who focussed on extending experimental data into the far infrared. Notably, his work on the measurement of blackbody radiation at long wavelengths contributed to one of the most pivotal moments in the history of quantum mechanics, when Max Planck found his well-known radiation law after discussing the discrepancy of measurements performed by Rubens and Wien's law of radiation [18]. Another helpful observation made around this time was that a mercury discharge lamp emits blackbody radiation due to the high plasma temperature at far longer wavelengths than just the visible spectrum, reaching even into the terahertz. In fact, this type of lamp is still used today as a broadband source in diffractive spectrometers. The available detectors used at this time were simple bolometers, often made from thin metallic wires [19], and later also thermopiles [20]. Thermal sources

remained the only way to conduct long-wavelength research from an optical approach. Military interest during the second world war pushed vacuum tube technology for radar applications and improved high-frequency performance dramatically, e.g. with magnetrons [21], reaching several hundred GHz in their higher harmonics [22].

Arguably the most impactful development occurred at the beginning of the information age in the 1960s when semiconductors found their way into commercially available computer systems. It had been known at least since the Michelson interferometer, that a spectrum can be reconstructed by Fourier transform of the interferogram from a variable path difference interferometer [23]. Unfortunately, this transform is too computationally expensive to be done by hand for large spectra and therefore could initially only be carried out for a handful of wavelengths in a reasonable amount of time. Recognized from early on as a powerful tool, the development of solutions to speed up the involved calculations drew attention. Purpose-built hardware based on early semiconductors, electron tubes or even ingenious mechanical machines were applied successfully and while still very limited, allowed a glimpse at the future of this technology. Two advancements enabled this method to become widely used in spectroscopy and other signal processing tasks: the publication of a *Fast Fourier Transform* algorithm by Cooley and Tukey in 1965[24] and the advent of advanced semiconductor logic and universal computers. With the computational bottleneck removed, it was possible from now on to effortlessly obtain spectral information without the drawbacks of diffractive optics. Even though the complete spectrum recovery would still be time-consuming on early-day computers, the superior resolution, throughput and bandwidth of a *Fourier Transform Spectrometer* justified this investment. Benefiting directly from all subsequent advancements in detector and computer technology, FFT systems remain the workhorse of far-infrared spectroscopy today. Apart from the mechanical variation of interferometer path length to produce interferograms, it is also possible to directly sample signals in the time domain and perform the Fourier transformation on the digital data. This dFFTS is bandwidth-limited by the sampling rate and processing power and frequency-limited by detector time constants and conversion speed. It is therefore not suitable for infrared radiation but finds application e.g. in radio astronomy where either directly sampled signals are processed this way or heterodyne techniques are used. Several GHz of instantaneous bandwidth is possible using modern FPGAs. The calculation of a spectrum from 32k data points is carried out in microseconds, a task that would have taken a lifetime of manual calculation in the early stages of Fourier transform spectroscopy.

In this era, the choice of sources was extended by the first traveling-wave tubes[25], backward wave oscillators[26] and gyrotrons[27], but regarding the application of a

previously untapped principle it is the terahertz gas laser that stands out the most. These lasers make use of adequate transitions in the wide choice of rotational lines in a molecular gas such as water vapor [28], HCN or CH3CN and later also CO2, CH3OH and N2O [29]. The first continuous-wave THz laser built in 1964 was an electrically excited water vapor design with 4 m cavity length emitting around 1 mW of power at several wavelengths between 28 and 118 µm[30]. Because of the high output power in a focussed, coherent beam these gas lasers evolved to become an essential element of THz research in the following decades. Their disadvantage is enormous power draw, large size and heavy weight, limiting applications primarily to stationary laboratory settings. Relying on molecular transitions, the emitted wavelength is almost fixed with little room for tuning.

Terahertz Quantum Cascade Lasers avoid many drawbacks of gas lasers. They are compact sources with a power consumption low enough to be considered for the restrictive environments of space- or airborne missions and the inherently large gain bandwidth enables the implementation of frequency tuning mechanisms.

2.2. Historical Development of QCLs

The history of quantum cascade lasers is entangled with research on semiconductor heterostructures, and while it is hardly possible to point at a single Eureka moment, there have been some key ideas and advancements that eventually led to the first working devices. Throughout their evolution from proof-of-principle to mature technology, QCLs have expanded into many fields and are now positioned as state-of-the-art laser sources for many applications.

One of those key steps at the beginning would be the theoretical work of Esaki and Tsu in 1970 on semiconductor superlattices[31] where they predict the appearance of minibands and suggest that it should be possible to create a novel class of semiconductor materials with selectable electronic properties.

The proposal of optical amplification with a superlattice by Kazarinov and Suris[32] dates back to 1971. It is generally considered the first serious attempt at a theoretical foundation of what would later become quantum cascade lasers. Although their proposed structure suffered technical shortcomings that would have prevented it from lasing, the work inspired many scientists to pursue the idea further.

Demonstrated shortly after the initial theoretical work using the revolutionary technology of molecular beam epitaxy (MBE), thin-film semiconductor heterostructures quickly became a topic of interest not only because of the novelty but also the prospect of application in the fast-growing semiconductor industry. An excellent review of the-

oretical and experimental development up to 1975 is given for example in [33]. At this point, optically pumped laser oscillation was already observed in such multilayer structures by van der Ziel et al.[34].

As the theoretical framework became refined with further significant contributions by Bastard[35], Ando[36] and many other authors it did not take long for experimentalists to catch up. In 1985 the first observation of intersubband absorption in epitaxially grown quantum wells by West and Eglash took place[37], and in 1989 Helm et al. were able to detect an electro-luminescence spectrum from intersubband transitions in a metalorganic vapor-phase epitaxy (MOVPE) grown GaAs/AlGaAs superlattice[38].

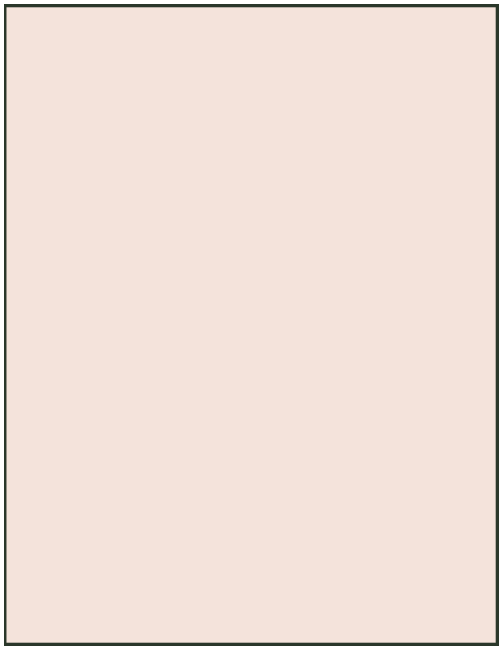

Figure 2.2.1.: Front cover of Science Vol 264, Issue 5158 on 22 April 1994 with an artistic impression of a quantum cascade laser multi-well structure.

This progress finally culminated in the first quantum cascade laser presented by Faist et al. in 1994[39]. After this breakthrough, the technology improved quickly, with new milestones reached in short succession, including room temperature operation[40] and extension to terahertz frequencies[41]. Today after many exciting developments that pushed the boundaries of QCL performance[42], they are the go-to solution for high-powered sources over large parts of the mid-IR and terahertz region.

Current topics of ongoing research on THz QCL include improvement of temperature performance, increasing tunability, output power and wall-plug efficiency, as well as new concepts such as broadband sources and frequency combs.

2.3. Basic Principles of QCLs

Every laser is based on the combination of a gain medium with an optical resonator, and quantum cascade lasers are no exception. While this fundamental principle is immutable, the actual way of building the active medium could not be more different among laser

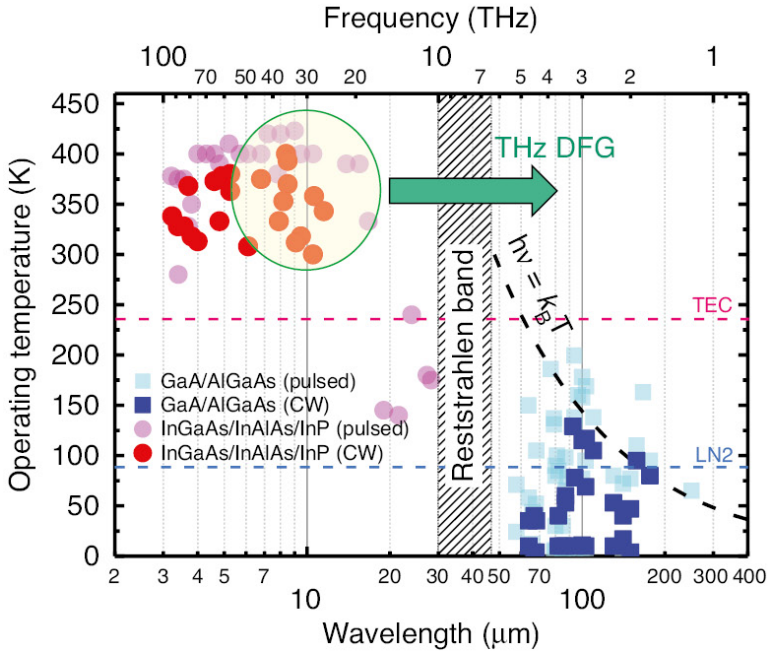

Figure 2.2.2.: A comparison of operating temperatures of QCLs at different wavelengths in 2018. While mid-IR QCLs routinely operate well above room temperature, Peltier-cooled continuous wave THz QCLs are still an active field of research. Indicated is also THz generation by difference frequency generation(DFG). Reproduced from[43]

types. The general idea in most cases is amplification by stimulated emission (excluding special cases, e.g. free electron lasers). This emission occurs through photon-induced electronic transitions from a higher energy level to a lower one. The necessary energy levels can be provided by excited states of atoms, molecules or semiconductors. Vital to the laser principle is the achievement of population inversion, i.e. the energetically higher state must be populated by more carriers then the lower one to yield a net gain between absorption and stimulated emission. This is fundamentally impossible in a two-level system in thermal equilibrium, but this is no longer true if more levels are involved, as is the case in every practical laser. In conventional lasers the involved energies are predetermined by the used materials or, more precisely, by the energies of electronic states inherent to atoms and molecules or the bandgap energy in semiconductors. Many characteristics of the laser, especially the possible range of emission wavelengths, are then primarily controlled by the material and can not be easily altered.

While the coulomb potential of an atom or the band structure of a given semiconductor is fixed, other possibilities exist to create electron bound states and control their energies. One is to use quantum wells created by stacking thin layers of different semiconductors. The conduction band edge of these semiconductors will be offset by a material-specific energy value and form quantum wells that contain electron wave functions with discretely

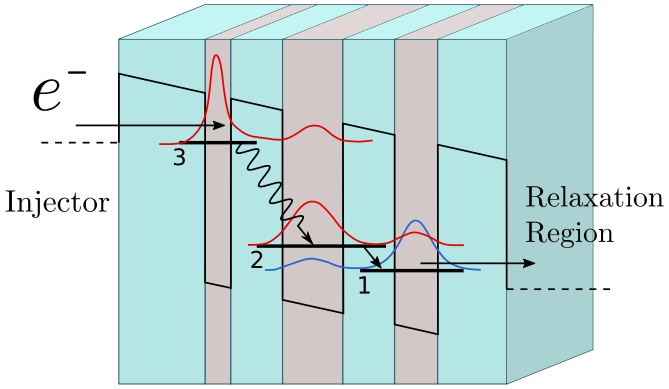

Figure 2.3.1.: Exemplary working principle of a QCL active region. Depicted is the layered heterostructure and the resulting quantum wells with applied voltage. Electrons are injected on the left and undergo a radiative transition from energy level 3 → 2. The lower laser level is efficiently depopulated by LO phonon-mediated scattering to level 1, ensuring population inversion. The square of the envelope function is indicated in red for the laser states and in blue for the relaxation state.

quantized electronic energy levels. This splitting of the semiconductor band continuum into discrete levels within the quantum wells is the basic idea behind quantum cascade lasers. Variation of the width of wells and barriers within the sequence lets us engineer the desired states in such a way that a population inversion can be achieved when a bias current is applied. This is done by not only controlling the energy of each level but also the transition rates between them, for example by allowing a fast, phonon-mediated depopulation channel of the lower laser level or increasing upper level lifetime by reducing the spatial overlap with the lower level.

One complete period of all the wells and barriers necessary to produce the intended electron states usually requires between two and ten quantum wells for the involved transitions. At the same time, additional injection and relaxation layers are often necessary to provide a defined potential for the carriers to enter and exit each period. An advantage of QCLs is that many periods can be stacked on top of each other, recycling the electrons at each step. The ratio of volume taken up by the gain medium within the waveguide can be maximized in this way which benefits the overall performance.

2.4. Heterodyne Terahertz Astronomy

The principle of astronomical heterodyne receivers closely links detection and generation of terahertz radiation. The idea of this principle is to shift the frequency of an observed signal to a much lower frequency enabling UHF signal processing techniques for spectral decomposition and power detection or even interferometry since the phase is preserved. The element capable of this conversion is called a frequency mixer and is based on a nonlinear process involving two time-variable signals. The nonlinearity leads to terms

that involve a multiplication of the two input signals, and it is easily shown with trigonometric theorems that in quadratic order this generates new components at the sum and difference frequencies:

$$f_{out} = |f_1 \pm f_2| \tag{2.1}$$

In reality, the nonlinearity of the mixing element is often not only quadratic. Semiconductors with a step-like IV curve, such as Schottky diodes are frequently used, especially when room-temperature operation is required. Terms of third and higher order produce further intermodulation products that are generally unused or even disruptive in a heterodyne system.

In a receiver, one of the input signals is a monochromatic wave at a fixed frequency called the local oscillator (LO). Consequently, the difference component $f_{IF} = |f_1 - f_{LO}|$, called the intermediate frequency (IF), satisfies precisely the idea behind heterodyne detection by shifting the detected ("sky-") signal to a lower frequency band. With the use of fast mixers, typically superconductor-insulator-superconductor (SIS) junctions or hot-electron bolometers (HEB), it is possible to downconvert an astronomical signal at several terahertz to a much lower frequency in the GHz range.

A direct consequence of this is the reduction of spectral resolution (relative to the IF bandwidth) needed to resolve molecular lines or similar features. A typical [CII] emission observed in a source like the Orion Nebula has a linewidth on the order of $5\,\mathrm{km\,s^{-1}}$ caused by Doppler broadening, with thermal contributions amounting to ca. $0.3\,\mathrm{km\,s^{-1}}$ at typical temperatures of 200 K and the rest originating from spatially unresolved turbulence. This corresponds to 32 MHz at 1.9 THz observed sky frequency, requiring at least R≈200 000 for a basic resolution of the line shape. The same line shifted to a typical intermediate frequency bandwidth of 4 GHz now requires only R≈400 to yield the same information, a task that is fulfilled far easier. Of course, for some sources, the linewidth can be dramatically different; observations of nearby galaxies can yield values above $100\,\mathrm{km\,s^{-1}}$ due to differential rotation and varying line-of-sight velocities while a cold, optically thin foreground observed in absorption against a background source is the opposite with a linewidth that can be below $0.1\,\mathrm{km\,s^{-1}}$.

The second consequence is the gained ability to digitally sample the IF, which is out of reach for THz frequencies. With purpose-built Fast-Fourier Transform spectrometers it is possible to cover a bandwidth of several GHz in the IF band with a few tens of kilohertz resolution. This enables measurements at an unrivaled spectral resolving power that allows us to identify emission lines from molecular rotational and atomic fine structure transitions and determine lineshapes in velocity-resolved observations.

Heterodyne detection in an astronomical context substantially motivated the advancement of continuous-wave sources to the THz region driven by demand for local oscillators.

Heterodyne detection at submillimeter wavelengths has been developed since the '70s, with astronomy and atmospheric sciences as the main driving force, initially using Schottky diodes [44]. Heterodyne systems come with an impressive spectral resolution, high enough to resolve line shapes and conduct Doppler shift analysis for cold, low-density gas in astronomical research and atmospheric sciences. It quickly became one of the main pillars of research focused on the interstellar medium (ISM) today.

Improving on Schottky mixers, a major leap in the sensitivity of heterodyne setups was achieved with the advent of superconducting devices. The superconducting tunnel junction, or superconductor-insulator-superconductor (SIS) junction, performs at low noise and pushed the frequency limits above 100 GHz at their first realisation[45][46]. This element is the most extreme example of a step-like IV curve that is unique in its nonlinearity. Nowadays, SIS mixers approach the fundamental quantum limit for coherent detection[47]. Another approach to terahertz mixing is, quite interestingly, a thermal detector. Historically bolometers tended to be slow, but to use them as mixing elements, they would need to respond fast enough to modulate at the intermediate frequency of the heterodyne system. This can be achieved with superconducting materials since below critical temperature their heat capacity is minimal while thermal conductivity is maximal, which leads to time constants on the order of picoseconds for a sufficiently small detector volume coupled to a thermal bath. Such a mixer design covers an IF bandwidth of several GHz and is called a superconducting hot electron bolometer (HEB), first demonstrated in 1990[48]. One feature of bolometric mixing is the inherently quadratic nature of the nonlinearity since the absorbed power is proportional to the square of the electric field strength.

The starting signal for the race towards heterodyne detection of astronomical gas lines at frequencies pushing towards the terahertz was probably fired in 1970 with the publication of a detection of the CO $1 \rightarrow 0$ 115 GHz line in the Orion Nebula by Wilson et al. using a receiver based on Schottky mixers[49].

Better noise performance was achieved with bolometers at helium temperatures, e.g. in a receiver built at Bell Labs for the NRAO 11 m telescope, based on an InSb hot electron bolometer mixer operating in the 90-140 GHz band[50]. As a non-superconductive bolometer, the IF bandwidth was limited to only a few MHz. Nevertheless, it was possible to detect a CO line at 115 GHz in various galactic objects, the famous Orion Nebula among them. By 1978 the list of detected interstellar molecules had already increased to 46 with hundreds of lines between 0.8 GHz and 345 GHz[51]. These

discoveries took place at observatories worldwide, including NRAO, Parkes Observatory, OSO, ARO, the Effelsberg 100-m Telescope and many more. The richness of detectable lines provoked investment into further development of heterodyne technology, with a clear focus on reaching higher frequencies and decreasing system noise, which was achieved predominantly with improvements in SIS technology[52][53]. The addition of the superconducting HEB to the instrument pool with the goal to increase the frequency range beyond the intrinsic limit of SIS junctions at double their superconductor bandgap it was possible already by 1992 to observe at frequencies as high as 2.5 THz[54] including the bright [CII] hyperfine transition at 1.9 THz, an important cooling line of the interstellar medium that falls into the spectral range covered by early heterodyne instruments e.g. a Schottky mixer heterodyne spectrometer developed by Max Planck Institute for Radio Astronomy and deployed to the Kuiper Airborne Observatory (KAO) since 1985[55].

The richness of molecular rotational lines at mm-wave frequencies is higher than in any other spectral region and is often referred to as the molecular fingerprint region. While higher rotational energy levels are less easily populated and consequently this abundance of lines is thinning out with increasing frequency, the terahertz region still contains a wealth of observable transitions. Knowledge of chemical components, isotopic ratios and velocity profiles allows a deep insight into the conditions and processes in celestial objects. Consequently, molecular transitions in the ISM are of high interest to the research on conditions and impact of star formation at I. Physikalische Institut der Universität zu Köln and the work groups of the SFB 956, where this thesis was carried out. Star-forming regions are the main focus, especially photodissociation regions (PDRs, [56]). One of the most luminous emission lines in those regions is the $^2P_{3/2} - ^2P_{1/2}$ [CII] fine structure line at 1.9005 THz (158 µm) originating from the cold neutral medium. As one of the fundamental cooling lines[57] it is a key factor in PDR energy dynamics and used as a tracer of the $H^+/H/H_2$ transition from the atomic to the molecular interstellar medium. As a result, the [CII] 158 µm line is an indirect tracer for the star formation rate[58][59]. Similarly, the [OI] atomic oxygen 63 µm line is a good tracer for massive star formation, where conditions for thermal excitation are met through PDR heating by UV fields[60].

Development of heterodyne instrumentation capable of observing these emissions has been carried out at the institute for many years in close collaboration of instrument scientists and astronomical work groups. In the course of this, several highly successful projects have evolved. Within the extended scope of KOSMA (Kölner Observatorium für Submillimeterastronomie) this includes several ground-based facilities - the original Gornergrat KOSMA Telescope and NANTEN 2 - as well as the HIFI instrument on

the HERSCHEL satellite and GREAT for the airborne platform SOFIA, both with a focus on the 1.9 THz [CII] transition but also capable of observing other molecular and atomic lines.

The institute's most recent contribution to heterodyne instrumentation is the development of the *German Receiver At Terahertz Frequencies* (GREAT)[3] together with Max Planck Institut für Radioastronomie. It is flown on board the *Stratospheric Observatory For Infrared Astronomy* (SOFIA), a heavily modified Boeing 747SP housing a 2.5 m telescope. At cruising altitudes of 38,000 to 43,000 ft, the atmospheric transmission is good enough for observations at the target frequencies. In its standard configuration, GREAT features a hexagonal 7-pixel array in the 1.9 THz band with two HEB mixers for each pixel enabling measurements in both polarizations[61] and a second similar array for the 4.7 THz band in a single polarization. The local oscillator system employs a quantum cascade laser in the high-frequency array (HFA) and Schottky multiplier chains in the low-frequency array (LFA). The low continuous tunability of THz QCLs (~5 GHz) so far discourages their use in the LFA, although the superior output power compared to multiplier chains would increase system performance. Therefore, the development of widely, continuously tunable THz QCLs is highly desired in this context. The requirements for a QCL local oscillator are continuous-wave, single mode operation with low-frequency drifts and phase noise.

Figure 2.4.1.: The Boeing 747sp aircraft turned into the airborne observatory SOFIA. Photo: M. Mertens

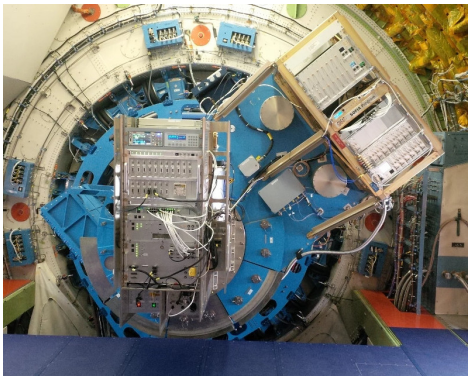

Figure 2.4.2.: GREAT installed on the SOFIA telescope flange. Photo: Bernd Klein, MPIfR.

2.5. Other Applications of Terahertz Sciences

Apart from astronomy, a variety of more earthly application fields also use terahertz radiation.

One of those fields are meteorology and geologic sciences, where terahertz spectroscopy and continuum measurements help to determine the composition of the atmosphere, in particular the water vapor content[62]. As one of the main greenhouse gases alongside CO2 and methane, reliable data on its abundance is an important input for climate models and weather forecasts. Terahertz instrumentation on Low Earth Orbit satellites is capable of providing this data with high accuracy in real time nowadays[63].

Biomedical applications for non-ionizing radiation capable of penetrating tissue are numerous[64]. Since the medical fields have an enormous social and economic impact, often driven by new developments, there has been a traditionally high interest in medical terahertz applications. Research comprises imaging techniques[65][66], protein structural analysis[67] or characterization of genetic material[68] and others.

As a tool of noninvasive testing and inspection of food products, terahertz probing can detect toxic compounds, residual antibiotics, foreign objects and quality degradation[69], although this area of application is relatively new and improvements in cost and speed are required to compete in the economically optimized food industry.

In the security domain, terahertz screening devices found widespread use either as an alternative to X-ray based scanners that are frequently seen at airports and other sensitive areas due to their ability to penetrate fabric and many other nonmetallic materials or as a means of spectroscopic substance identification, especially the detection of explosive compounds and drugs[70].

Finally, wireless communication as a cornerstone of the information age is steadily approaching data transfer rates that will require terahertz frequency carrier signals in the near future to meet bandwidth requirements. The highest frequencies of currently deployed 5G equipment already reach 26 GHz and are often referred to as "mmWave technology" by telecommunication companies. However, the corresponding wavelength is still slightly longer than 1 cm. Extending wireless networking technology into the THz frequency range could theoretically enable data transmission rates on the order of terabits per second, although atmospheric absorption quickly reaches $100\,\mathrm{dB\,km^{-1}}$ above 1 THz[71], even away from distinct absorption lines.

Chapter 3.

Theoretical Background of QCLs

3.1. Introduction

The theoretical framework to describe quantum cascade lasers has a deep rooting in solid state physics of semiconductors. To understand the working principles and the behavior of a QCL one needs to investigate the microscopic dynamics of the charge carriers, photons and phonons within a quantum mechanical description of the semiconductor structure. A good starting point is certainly to study the origins of subbands by extending bulk semiconductor theory to heterostructures with a spatial band gap discontinuity. Electronic transitions between those subbands are the foundation on which the optical gain necessary to build a laser can be achieved. In order to build a functioning active region one needs to calculate the coupling strength of the optical transitions to the electromagnetic field and ensure a stable population inversion between the laser states, which means that non-optical scattering mechanisms have to be factored in and techniques for efficient filling and depletion of upper and lower laser state have to be found. A sophisticated multi-quantum well arrangement can satisfy these requirements by utilizing phonon interactions and tunneling effects. Finally, to build a working laser device, waveguiding and beam shaping are required, which, especially for THz frequencies, can pose a significant challenge due to subwavelength dimensions and free carrier losses.

3.2. Semiconductor Quantum Well Heterostructures

The fundamental novelty that makes quantum cascade lasers such a fascinating innovation is the utilization of band structure engineering in semiconductor quantum wells to build a system of energy eigenstates capable of achieving optical gain without the dependency on intrinsic material properties that is characteristic of conventional semiconductor lasers. The foundation on which any band engineering can happen is a

quantum mechanical framework that allows the calculation of the involved electronic wave functions. An excellent overview of the required tools to model QCLs can be found in Faist[72], while Bastard[73] is a good source for methods employed in the theory of general semiconductor heterostructures.

Effective Electron Mass As with many problems of solid state physics one possible first step to model the band structure is to find the effective electron mass m^*. This is usually done by solving the so-called $\mathbf{k}\cdot\mathbf{p}$ approximation[74] and originates from the idea to numerically extrapolate Γ point energy gaps to the entire Brillouin zone assuming sufficient optical matrix elements are experimentally known. A derivation is available in many textbooks at a varying degree of depth[75][76].

Here the one-electron Schrödinger equation is

$$H\Psi_{n\mathbf{k}}(\mathbf{r}) = E_n(\mathbf{k})\Psi_{n\mathbf{k}}(\mathbf{r}) \tag{3.1}$$

with Bloch functions $\Psi_{n\mathbf{k}}(\mathbf{r})$ of the form

$$\Psi_{n\mathbf{k}} = e^{i\mathbf{k}\cdot\mathbf{r}}u_{n\mathbf{k}}(\mathbf{r}). \tag{3.2}$$

The cellular functions $u_{n\mathbf{k}}(\mathbf{r})$ are periodic for each unit cell. The Hamiltonian used for a crystal includes a periodic crystal potential $V(\mathbf{r})$ and the spin-orbit term:

$$H = \frac{p^2}{2m_0} + V(\mathbf{r}) + \frac{\hbar}{4m_0^2c^2}(\sigma \times \nabla V)\cdot\mathbf{p} \tag{3.3}$$

Substituting this into equation 3.1 and neglecting the spin-orbit term leads to the Schrödinger equation in $u_{n\mathbf{k}}(\mathbf{r})$:

$$\left(\frac{p^2}{2m_0} + \frac{\hbar}{m_0}\mathbf{k}\cdot\mathbf{p} + \frac{\hbar^2k^2}{2m_0} + V(\mathbf{r})\right)u_{n\mathbf{k}}(\mathbf{r}) = E_n(\mathbf{k})u_{n\mathbf{k}}(\mathbf{r}) \tag{3.4}$$

The idea behind the $\mathbf{k}\cdot\mathbf{p}$ - approximation is now to treat the $\mathbf{k}$-dependent terms as perturbations and expand a solution $u_{n\mathbf{0}}(\mathbf{r})$ for $\mathbf{k} = 0$ of equation 3.4 into $\mathbf{k}$. Such a solution to

$$\left(\frac{p^2}{2m_0} + V(\mathbf{r})\right)u_{n\mathbf{0}}(\mathbf{r}) = E_n(\mathbf{0})u_{n\mathbf{0}}(\mathbf{r}) \tag{3.5}$$

is much easier to find than a general electronic Schrödinger equation - even in mean-field approximation - since the periodicity of $u_{n\mathbf{k}}(\mathbf{r})$ can be exploited. One way to calculate the perturbation is to assume that the band energy has a nondegenerate extremum at the Γ point[75] and expand $u_{n\mathbf{k}}(\mathbf{r})$ and $E_n(\mathbf{k})$ to second order in k:

$$u_{n\mathbf{k}} = u_{n\mathbf{0}} + \frac{\hbar}{m_0} + \sum_{m\neq n} \frac{\langle u_{n\mathbf{0}}|\mathbf{k}\cdot\mathbf{p}|u_{m\mathbf{0}}\rangle}{E_{n\mathbf{0}} - E_{l\mathbf{0}}} \tag{3.6}$$

$$E_{n\mathbf{k}} = E_{n\mathbf{0}} + \frac{\hbar^2 k^2}{2m_0} + \frac{\hbar^2}{m_0^2} \sum_{m\neq n} \frac{|\langle u_{n\mathbf{0}}|\mathbf{k}\cdot\mathbf{p}|u_{m\mathbf{0}}\rangle|^2}{E_{n\mathbf{0}} - E_{m\mathbf{0}}} \tag{3.7}$$

Because $E_{n\mathbf{0}}$ had been assumed an extremum, the terms linear in $\mathbf{k}$ vanish. It is now possible to define the electron effective mass m^* for each band with

$$E_{n\mathbf{k}} = E_{n\mathbf{0}} + \frac{\hbar^2 k^2}{2m^*} \tag{3.8}$$

Comparison with equation 3.7 yields the conventional expression for the calculation of m^* in the $\mathbf{k}\cdot\mathbf{p}$ approximation:

$$\frac{1}{m^*} = \frac{1}{m_0} + \frac{2}{m_0^2 k^2} \sum_{m\neq n} \frac{|\langle u_{n\mathbf{0}}|\mathbf{k}\cdot\mathbf{p}|u_{m\mathbf{0}}\rangle|^2}{E_{n\mathbf{0}} - E_{m\mathbf{0}}} \tag{3.9}$$

The $\mathbf{k}\cdot\mathbf{p}$ approximation holds as long as the kinetic energy term $\hbar^2 k^2/(2m^*)$ (see eq.3.8) is negligible with respect to the bandgap at the Γ point. But this might not be the case at a given $\mathbf{k}$ for a low effective mass m^* and a small band gap, most notably for InSb. One could either resort to higher order approximation beyond the quadratic term, or use a technique proposed by E.Kane[77][78] that represents the solutions $u_{n\mathbf{k}}(\mathbf{r})$ for any $\mathbf{k}$ by expansion into solutions at $\mathbf{k} = 0$:

$$u_{n\mathbf{k}}(\mathbf{r}) = \sum_m c_m^{(n)}(\mathbf{k}) u_{m\mathbf{0}}(\mathbf{r}). \tag{3.10}$$

The number of bands m that are calculated in the sum determine the accuracy and are normally limited to the most relevant ones. In a very simple model only the conduction band and the valence band may be considered. Equation 3.7 leads to the dispersion for the conduction band:

$$E_c(k) = E_c(0) + \frac{\hbar^2 k^2}{2m_0} + \frac{\hbar^2 k^2}{m_0^2} \frac{|\langle u_{c0}|p|u_{v0}\rangle|^2}{E_g} \tag{3.11}$$

With the definition of the Kane energy E_P it is common to shorten the expressions for the conduction band energy dispersion and effective mass:

$$E_P = \frac{2}{m_0} |\langle u_{c0}|p|u_{v0}\rangle|^2 \tag{3.12}$$

$$E_c(k) = E_c + \frac{\hbar^2 k^2}{2m_0} \left(1 + \frac{E_P}{E_g}\right) \tag{3.13}$$

$$m^* = m_0 \left(\frac{E_g}{E_g + E_P}\right) \tag{3.14}$$

It should be noted that the Kane energy is relatively uniform over the III-V semiconductors (ca. 23 eV) and $E_g \ll E_P$. Consequently, the effective mass is small and generally proportional to the bandgap.

The Envelope Function Approximation For a heterostructure consisting of many layers of different materials - such as in a QCL - a number of ways exist to calculate the electronic wave functions, the most popular ones being the empirical tight-binding model, the pseudo-potential formalism and the envelope function approximation. The tight-binding model often yields the most accurate results and is valid over the entire Brillouin zone, but quickly becomes computationally inefficient. For QCLs most often the envelope function approximation is used for its intuitive physical assumptions and has proved reliable and computationally efficient in calculating electronic states in semiconductor heterostructures. Fundamentally it comes down to a further development of the the $\mathbf{k} \cdot \mathbf{p}$ approximation to accommodate the effects of the alternating potential along the growth axis. Since the periodic term of the Bloch function $u_{n\mathbf{k}}(\mathbf{r})$ has the periodicity of the crystal lattice, but the lattice does not extend infinitely in all directions as in a bulk material, it seems natural to modulate it by an envelope function instead of a plane wave $e^{i\mathbf{kr}}$. For each layer of the structure made from either material A or B it is assumed, that the wave function can be expanded in the periodic part $u^{(A,B)}_{n\mathbf{k_0}}(\mathbf{r})$ of the band edge Bloch functions at a wave vector $\mathbf{k_0}$ of the bulk material.

Formally this is written as

$$\Psi(\mathbf{r}) = \sum_l f_l^{(A,B)}(\mathbf{r})\, u_{l\mathbf{k_0}}^{(A,B)}(\mathbf{r}) \tag{3.15}$$

and comes with a set of conditions. Firstly the envelope function $f_l^{(A,B)}(\mathbf{r})$ must be slowly-varying compared to $u_{l\mathbf{k_0}}^{(A,B)}(\mathbf{r})$. Additionally, the two layers cannot be too different, which means more precisely that $u_{l\mathbf{k_0}}^{(A,B)}(\mathbf{r}) = u_{l\mathbf{k_0}}(\mathbf{r})$ must be the same in both materials.

In order to describe the electronic states we must determine the functions $f_l^{(A,B)}(\mathbf{r})$. The boundary conditions at the interface between the materials A and B have to guarantee the continuity of $\Psi(\mathbf{r})$, therefore

$$f_l^{(A)}(\mathbf{r}_\parallel, z_0) = f_l^{(B)}(\mathbf{r}_\parallel, z_0) \tag{3.16}$$

where z_0 is the position of the interface and $\mathbf{r}_\parallel = (x, y)$. Since the crystalline structure is not changing within the layers, the system is invariant under translations, and the $f_l^{(A,B)}$ factorizes into an in-plane wave and an envelope function in the growth direction

$$f_l^{(A,B)}(\mathbf{r}_\parallel, z) = \frac{1}{\sqrt{S}}\, e^{i\mathbf{k}_\parallel \mathbf{r}_\parallel}\, \chi_l^{(A,B)}(z) \tag{3.17}$$

with the sample area S and $\mathbf{k} = (k_x, k_y)$. Following [79], the total heterostructure Hamiltonian can be written as

$$H = \frac{p^2}{2m_0} + V_A(\mathbf{r})\, Y_A + V_B(\mathbf{r})\, Y_B \tag{3.18}$$

where $Y_{A/B}$ are unity for all $\mathbf{r}$ within the respective layer A or B and zero everywhere else. By letting H act on Ψ one finds after a rather long calculation (which can be found in [73]) the following set of differential equations:

$$D^{(0)}\left(z, -i\hbar\frac{\partial}{\partial z}\right)\boldsymbol{\chi} = \varepsilon\boldsymbol{\chi} \tag{3.19}$$

with the matrix elements

$$D_{lm}^{(0)}\left(z,-i\hbar\frac{\partial}{\partial z}\right)=\left[\varepsilon_{l,0}^{(A)}Y_A+\varepsilon_{l,0}^{(A)}Y_A+\frac{\hbar^2k_\parallel^2}{2m_0}-\frac{\hbar^2}{2m_0}\frac{\partial^2}{\partial z^2}\right]\delta_{lm} + \frac{\hbar\mathbf{k}_\parallel}{m_0}\langle\, l\,|\,\mathbf{p}_\parallel\,|\,m\,\rangle-\frac{i\hbar}{m_0}\langle\, l\,|\,p_z\,|\,m\,\rangle\frac{\partial}{\partial z} \tag{3.20}$$

where $\langle\, l\,|\,p_z\,|\,m\,\rangle = \int_\Omega u_{l0}^*\,\mathbf{p}\,u_{m0}\,d^3r$ and $D^{(0)}$ is a $N\times N$ matrix, where N is the number of band edge Bloch functions that are used in the initial approximation in equation 3.15. The results obtained by solving equation 3.19 will become more accurate if one considers additional bands. It is established practice to limit the calculation to 8 bands, which means that only states that belong to the Γ_6, Γ_7 and Γ_8 bands of the materials are included since these bands are typically relevant for optical and transport mechanisms in III-V and II-VI semiconductors[79]. It turns out that this description is sometimes insufficient to model the valence band correctly and one has to include remote bands by a perturbative approach. All this considered, the ultimate equation system (sometimes referred to as the *Pidgeon-Brown model*[80]) that has to be solved to calculate the envelope functions $\chi_l(z)$ is

$$\begin{aligned}\sum_{m=1}^{8}\Bigg[&\left(\varepsilon_{m_0}^{(A)}+V_m(z)+\frac{\hbar^2\mathbf{k}_\parallel^2}{2m_0}-\frac{\hbar^2}{2m_0}\frac{\partial^2}{\partial z^2}\right)\delta_{lm}-\frac{i\hbar}{m_0}\langle\, l\,|\,p_z\,|\,m\,\rangle\frac{\partial}{\partial z}\\ &+\frac{\hbar\mathbf{k}_\parallel}{m_0}\langle\, l\,|\,\mathbf{p}_\parallel\,|\,m\,\rangle-\frac{\hbar^2}{2}\frac{\partial}{\partial z}\frac{1}{M_{lm}^{zz}}\frac{\partial}{\partial z}-\frac{i\hbar^2}{2}\sum_{\alpha=x,y}\left(k_\alpha\frac{1}{M_{lm}^{\alpha z}}\frac{\partial}{\partial z}+\frac{\partial}{\partial z}\frac{1}{M_{lm}^{a\alpha}}k_\alpha\right)\\ &+\frac{\hbar^2}{2}\sum_{\alpha,\beta=x,y}k_\alpha\frac{1}{M_{lm}^{\alpha\beta}}k_\beta\Bigg]\chi_m=\varepsilon\chi_l,\qquad 1\le l\le 8\end{aligned} \tag{3.21}$$

and requires some further knowledge about the material system, particularly the band offsets V_l, which often have to be determined experimentally when working on a specific heterostructure[81][82]. Without precise knowledge of the band offsets, it would be impossible to build QCLs since the energy levels of the bound quantum well states directly depend on them. In many cases though, it is sufficient to solve the less intricate equation 3.19 for several bands, in some cases even only two or three.

Finally, in addition to $\boldsymbol{\chi}$ being continuous at $z=z_0$, we find the following boundary conditions by integrating over the interfaces:

$$A^{(A)}\boldsymbol{\chi}^{(A)}(z_0)=A^{(B)}\boldsymbol{\chi}^{(B)}(z_0) \tag{3.22}$$

where A is a $N \times N$ matrix with elements

$$A_{lm} = -\frac{\hbar^2}{2m_0}\left[\left(\delta_{lm} + \frac{m_0}{M_l^{zz}}\right)\frac{\partial}{\partial z} + \frac{2i}{\hbar}\langle\, l \,|\, p_z \,|\, \delta_{lm}\,\rangle + i\sum_{\alpha=x,y}\frac{m_0}{M_{lm}^{z\alpha}}k_\alpha\right] \tag{3.23}$$

A simple model illustrating this is the **Ben Daniel-Duke model**[83], a simple one-band model. In this case, equation 3.19 simplifies to the Schrödinger equation

$$\left(-\frac{\hbar^2}{2m^*}\frac{\partial^2}{\partial z^2} + \frac{\hbar^2 k_\parallel^2}{2m^*} + V(z)\right)\chi(z) = E\,\chi(z) \tag{3.24}$$

with twofold spin-degenerate solutions while the boundary conditions become

$$\chi^{(A)}(z_0) = \chi^{(B)}(z_0) \tag{3.25}$$

$$\frac{1}{m^*_{(A)}}\frac{\partial}{\partial z}\chi^{(A)}(z_0) = \frac{1}{m^*_{(A)}}\frac{\partial}{\partial z}\chi^{(B)}(z_0) \tag{3.26}$$

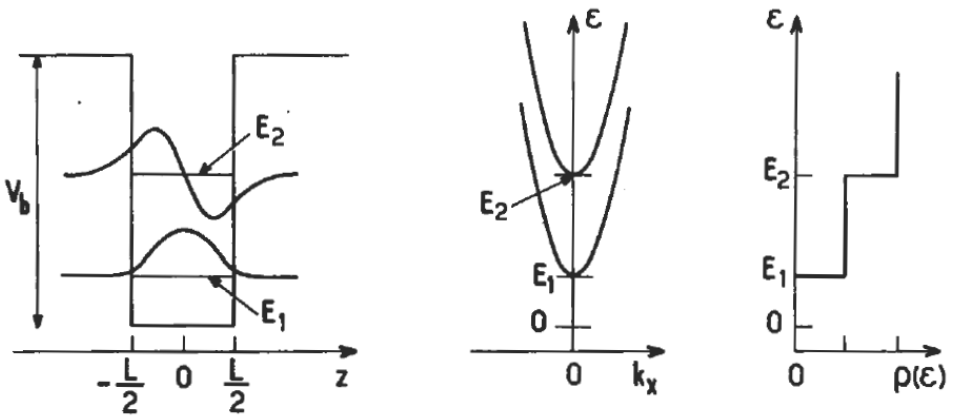

Figure 3.2.1.: a) A conduction band edge quantum well with the envelope functions of the first two bound states at energies E_1 and E_2 as calculated with the Ben Daniel-Dukes model; **b)** In-plane dispersion relation; **c)** Density of states. Reproduced from [73]

This can be easily solved and already decently describes the lowest conduction band state for thick QWs in material systems where the band gap is sufficiently large, as well as the solitary heavy hole levels, but is not suited for QCL development since higher energy states are required as well.

A better approximation incorporates a valence band in addition to the single conduction band. This valence band assumes a separated heavy-hole band and combines

light-hole and split-off bands into an effective valence band. Equation 3.19 in this two-band model simplifies for $\boldsymbol{k}_{\parallel} = 0$ to

$$\begin{pmatrix} V_C(z) & -\frac{i\hbar}{m_0} p_{cv} \frac{\partial}{\partial z} \\ -\frac{i\hbar}{m_0} p_{cv}^* \frac{\partial}{\partial z} & V_v(z) \end{pmatrix} \begin{pmatrix} \chi_c \\ \chi_v \end{pmatrix} = E \begin{pmatrix} \chi_c \\ \chi_v \end{pmatrix} \tag{3.27}$$

which can be solved for the conduction band envelope functions:

$$-\frac{\hbar^2}{2} \frac{\partial}{\partial z} \frac{1}{m^*(E,z)} \frac{\partial}{\partial z} \chi_c + V_c(z)\chi_c = E\chi_c \tag{3.28}$$

with an effective mass dependent on both the energy and the z coordinate defined by

$$\frac{1}{m^*(E,z)} = \frac{1}{m_0} \frac{E_P}{E - V_v(z)} \tag{3.29}$$

where $E_P = \frac{2}{m_0}|p_{cv}|^2 = \frac{2}{m_0}|\langle u_{c0}|p|u_{v0}\rangle|^2$ is the Kane energy (see eq. 3.12). This energy-dependant effective mass alters the energy dispersion $E_C(\boldsymbol{k}) = \frac{\hbar^2 k^2}{2m^*}$ which now is not purely parabolic any more. This non-parabolicity shifts the energy states in a QW, where the discrepancy between a one-band and a two-band model becomes increasingly apparent for higher energies (see figure 3.2.2).

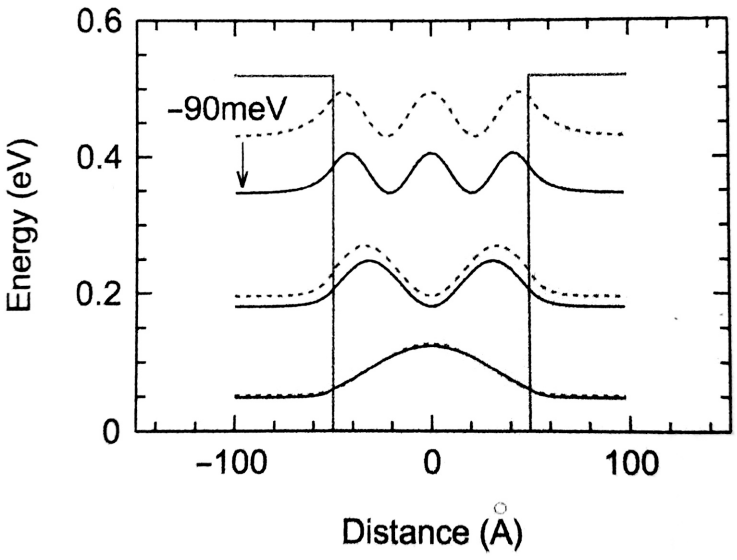

Figure 3.2.2.: Effect of non-parabolicity on energy states in a quantum well. The two-band model (dashed) is significantly shifted for higher energies compared to the one-band model (solid). Reproduced from [72].

3.3. Optical Intersubband Transitions

Contrary to standard semiconductor laser diodes the photonic process within a QCL involves *intersubband transitions* instead of *interband transitions*. They are very different in nature and produce unique phenomena as is shown in this section.

The light-matter interaction can be treated as a perturbation by adding an interaction term H' to the Hamiltonian such that $H = H_0 + H'(t)$ with $H' = (e/m^*)(\boldsymbol{A} \cdot \boldsymbol{p})$ in the dipole approximation[84] where the vector potential $\boldsymbol{A}$ is linked to the electric field by $\boldsymbol{E} = -\partial \boldsymbol{A}/\partial t$ and can be written as

$$\boldsymbol{A} = \frac{iE_0\hat{\boldsymbol{e}}}{2\omega} e^{i\boldsymbol{q}\boldsymbol{r}-\omega t)} \tag{3.30}$$

with polarization vector $\hat{\boldsymbol{e}}$.

Using Fermi's Golden Rule, it follows that the transition rate from state $|i\rangle$ to $|j\rangle$ is

$$W_{if} = \frac{2\pi}{\hbar} \frac{e^2 E_0^2}{4m^{*2}\omega^2} \left| \left\langle \Psi^{(i)} \middle| \hat{\boldsymbol{e}} \cdot \boldsymbol{p} \middle| \Psi^{(j)} \right\rangle \right|^2 \delta(E_f - E_i \pm \hbar\omega) \tag{3.31}$$

Proceeding with the simple picture of an electron confined to a single band ν with wave function $\Psi^{(i,j)}(\boldsymbol{r}) = f^{(i,j)}(\boldsymbol{r}) u_{(\nu,\nu')}(\boldsymbol{r})$ (see eq. (3.15)) the matrix element between state i and j is

$$\begin{aligned} \left\langle \Psi^{(i)} \middle| \hat{\boldsymbol{e}} \cdot \boldsymbol{p} \middle| \Psi^{(j)} \right\rangle &= \hat{\boldsymbol{e}} \cdot \left\langle f^{(i)} u_\nu \middle| \boldsymbol{p} \middle| f^{(j)} u_{\nu'} \right\rangle \\ &= \hat{\boldsymbol{e}} \cdot \left\langle f^{(i)} \middle| \boldsymbol{p} \middle| f^{(j)} \right\rangle \delta_{\nu\nu'} + \hat{\boldsymbol{e}} \cdot \left\langle f^{(i)} \middle| f^{(j)} \right\rangle \langle u_\nu \,|\, p \,|\, u'_\nu \rangle \end{aligned} \tag{3.32}$$

where the first term corresponds to the intersubband transition and the second to the interband transition. Now decoupling the in-plane wave from the envelope function $f_i(\mathbf{r}_\parallel, z) = S^{-1/2}\, e^{i\mathbf{k}_\parallel \mathbf{r}_\parallel}\, \chi_i(z)$ (eq. (3.17)) the matrix element in the dipole approximation becomes

$$\hat{e}_{x,y} \cdot \langle f_i \,|\, p_{x,y} \,|\, f_j \rangle = \frac{1}{S} \hbar k_{x,y} \hat{e}_{x,y} \delta_{\boldsymbol{k}_\parallel \boldsymbol{k}'_\parallel} \delta_{i,j} \tag{3.33}$$

where $\hat{e}_{x,y}$ is the polarization vector component in x or y direction. These matrix elements are zero for all transitions between states with nonidentical subband index ν or any change in $\boldsymbol{k}$. It is therefore the z-component matrix element

$$\langle \chi_i \,|\, p_z \,|\, \chi_j \rangle = \int dz\, \chi_i(z) p_z \chi_j(z) \tag{3.34}$$

that controls the intersubband transitions between states $\langle i \rangle$ and $\langle j \rangle$ [73]. This shows two important properties of optical intersubband transitions: The in-plane wave vector is conserved, and only the electric field component in z-direction couples to the transition. This important selection rule largely holds for more sophisticated models, and experimentally observed absorption data in GaAs/GaAlAs heterostructures is in good agreement with theory[85].

For practical applications, the absorption coefficient is often a more directly accessible property than the transition rates and is expressed as α_{2D} for a two-dimensional layer and vertically incident radiation by summing over all combinations of initial and final states under the assumption that the occupation probability is governed by the Fermi-Dirac distribution $F(E)$ and taking into account stimulated emission:

$$\begin{aligned} \alpha_{2D} = \frac{\hbar\omega}{IA} \sum_{i,j} \sum_{k_\parallel} \frac{2\pi}{\hbar} \left| \left\langle i \left| \frac{e}{m^*} \boldsymbol{A} \cdot \boldsymbol{p} \right| j \right\rangle \right|^2 \Big(F(E_{i,\boldsymbol{k}_\parallel}) - F(E_{j,\boldsymbol{k}_\parallel}) \Big) \\ \cdot \delta(E_{j,\boldsymbol{k}_\parallel} - E_{i,\boldsymbol{k}_\parallel} - \hbar\omega) \end{aligned} \tag{3.35}$$

From here, it is now possible to derive a much simpler expression valid for parabolic in-plane dispersion using the polarization selection rule and conservation of the wave vector $\boldsymbol{k}_\parallel$. After integrating, the absorption coefficient now reads:

$$\alpha_{2D} = \frac{e^2 kT}{2\epsilon_0 c \eta \hbar} \sum_{i,j} f_{i,j} \cdot ln \left[\frac{1 + e^{(E_F - E_i)/kT}}{1 + e^{(E_F - E_j)/kT}} \right] \frac{\Gamma \pi^{-1}}{(E_j - E_j - \hbar\omega)^2 + \Gamma^2} \tag{3.36}$$

where c is the speed of light, η the refractive index, E_F the Fermi energy and Γ the HWHM of the Lorentzian [86] that replaced the δ-function to take broadening of the line due to scattering processes (often dominated by interface roughness scattering [87]) into account. Finally $f_{i,j}$ is the widely used oscillator strength:

$$f_{i,j} = \frac{2}{m_0} \frac{|\, \langle \psi^{(0)} | P | \psi^{(0)} \rangle \,|^2}{E_i - E_0} \tag{3.37}$$

An important result here is that the $\boldsymbol{k}_\parallel$-dependence of the energy terms has vanished due to the parabolic dispersion. As a significant difference to interband transitions, this is the cause of narrow linewidths observed in QCLs compared to conventional diode

lasers.

Absorption and gain are closely related; in fact the rate of stimulated emission in a two-level system with total population inversion is identical to the absorption in the case of zero upper-state population. Consequently, the same derivation as for the absorption can be used for the gain by simply defining gain as negative absorption:

$$g(\omega) = -\alpha(\omega) \tag{3.38}$$

Of course, equation (3.35) is not valid for a pumped laser since the state population is not Fermi-Dirac distributed, and in a real-world implementation the gain volume within a waveguide is not a two-dimensional sheet containing a single quantum well. Instead, a more general volume electron density N_i of electrons spatially located within the quantum well or wells is used to describe the number of electrons in state i within a given volume. The expression for $\alpha(\omega)$ then is

$$\alpha(\omega) = \frac{2\pi e^2 \left|\langle \chi_i \,|\, z \,|\, \chi_j \rangle\right|^2 (N_i - N_j)}{\varepsilon_0 \eta \lambda} \frac{\Gamma}{(E_j - E_i - \hbar\omega)^2 + \Gamma^2} \tag{3.39}$$

with dipole matrix element $z_{ij} = \langle \chi_i \,|\, z \,|\, \chi_j \rangle$.

Closely related as a measure for the maximum attainable gain at the resonant wavelength ($\hbar\omega = E_j - E_i$) is the *peak material gain*[88], given for a Lorentzian line shape by

$$G_P = \frac{4\pi e^2}{\varepsilon_0 \eta \lambda} \frac{|z_{ij}|^2}{2\Gamma} (N_j - N_i) \tag{3.40}$$

which emphasizes that high output powers depend on a narrow line profile and efficient population inversion.

The last effect to finally complete the set of radiative processes is spontaneous emission, whose rate is given in the dipole approximation by

$$\frac{1}{\tau_{spon}} = \frac{e^2 \eta}{3\pi c^3 \varepsilon_0 \hbar^3} E_{ij}^3 \left|\langle \chi_i \,|\, z \,|\, \chi_j \rangle\right|^2 \tag{3.41}$$

and can be calculated by means of quantum field theory e.g. in the framework of Wigner-Weisskopf theory.

3.4. Scattering Processes

Scattering processes as nonradiative transitions between quantum states, either intra- or intersubband, are a the main obstacle every QCL design has to overcome. Some of these processes are intrinsic to the quantum well system and cannot be avoided, while others are caused by manufacturing imperfections such as impurities or crystal defects. While the attainable gain is limited through scattering events since they reduce upper-state lifetimes, they play an essential role when it comes to maximization of the attainable population inversion since lower states can be efficiently depopulated with resonant phonon designs. For mid-infrared QCLs, two effects are crucial: optical phonon emission and interface roughness scattering. The picture is more complicated at longer wavelengths, especially for THz-QCLs, since the energy level separation is below the optical phonon energy and additional scattering processes become relevant.

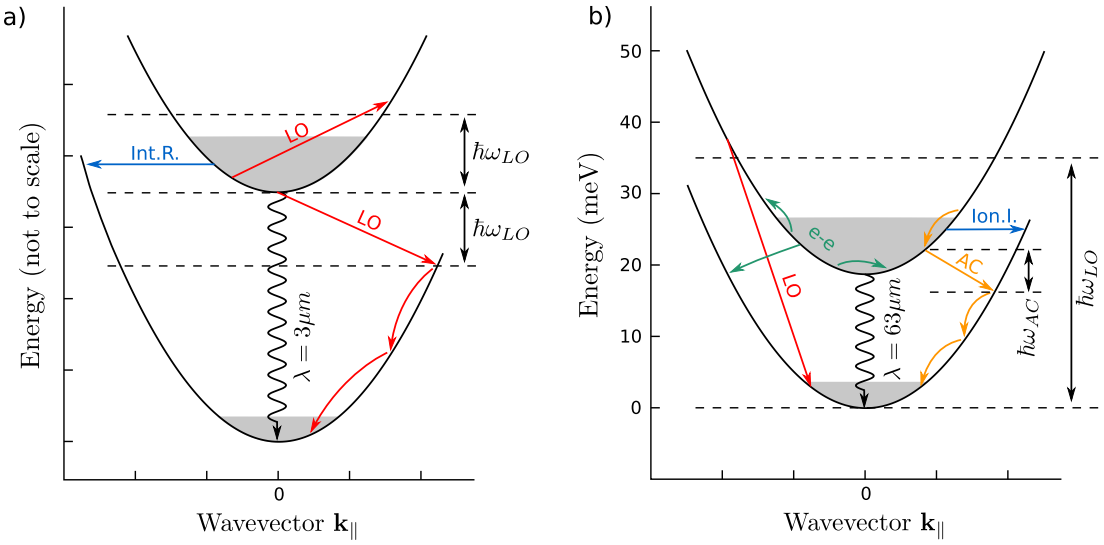

Figure 3.4.1.: Contributing inter- and intraband scattering channels in **a)** mid-IR QCLs ($E_{21} \geq \hbar\omega_{LO}$). For energy separation larger than the longitudinal optical phonon energy, their emission and absorption are the dominant nonradiative processes with scattering times on the order of 1 ps (LO). Interface roughness scattering (Int.R.) occurs in short wavelength lasers ($\lambda \lesssim 5\,\mu m$). When **b)** $E_{21} \leq \hbar\omega_{LO}$ as in THz-QCLs LO scattering is reduced and acoustical phonon (AC), electron-electron (e-e) and ionized impurity (Ion.I.) scattering determine a significant share of the electron dynamics. Adapted from [72]

Of all nonradiative scattering processes involved in a QCL, *longitudinal optical phonon emission* stands out due to its exceptionally low scattering times on the order of 1 picosecond for intersubband transitions and hundreds of femtoseconds for intrasubband relaxations[89]. The calculation of τ_{ij} for any scattering process is possible again through Fermi's golden rule

$$\frac{1}{\tau_{ij}} = \frac{2\pi}{\hbar} \left|\langle \Psi_i \,|\, H_{sc} \,|\, \Psi_j \rangle\right|^2 \delta(E_j - E_i - \hbar\omega_{LO}) \tag{3.42}$$

with the scattering Hamiltonian H_{sc}. For phonon-mediated intersubband scattering described by the Frölich Hamiltonian[90] and assuming bulk electrons at $\boldsymbol{k}_{\parallel} = 0$ this gives

$$\frac{1}{\tau_{ij}} = \frac{m^* e^2 \omega_{LO}}{2\hbar^2 \epsilon_P q_{ij}} \int dz \int dz' \chi_i(z)\chi_j(z) e^{-q_{ij}(z-z')} \chi_i(z')\chi_j(z') \tag{3.43}$$

where q_{ij} is the exchanged in-plane momentum

$$q_{ij} = \sqrt{\frac{2m^*(E_{ij} \pm \hbar\omega_{LO})}{\hbar^2}} \tag{3.44}$$

for emission $(-)$ or absorption of an LO phonon $(+)$. There are two important conclusions: First, the scattering time is minimal when the subband spacing matches the optical phonon energy. For GaAs $\hbar\omega_{LO}$ is 36 meV and the corresponding τ_{ij} is around 0.25 ps. Second, τ_{ij} depends on the effective mass through $\tau_{ij} \propto (m^*)^{-1/2}$, which means the choice of the material system has an influence on the state lifetime since m^* generally decreases with a smaller band gap.

This LO phonon prevalence is not present when the energy separation is smaller than $\hbar\omega_{LO}$ since the optical phonon emission is forbidden at $T = 0$. Consequently, these devices exhibit significantly longer electronic state lifetimes limited mainly by acoustic phonon scattering[90][91], but also thermally activated LO phonon emission[92] (i.e. by "hot" electrons in the upper laser level gaining enough energy to be separated by $\hbar\omega_{LO}$ from a lower level they can then transition to by LO phonon emission), electron-electron interaction, alloy disorder and ionized impurity scattering play a non-negligible role.

A comprehensive overview is given by Unuma et al.[87] based on Ando's theory[93]. In total, the scattering rates of all involved mechanisms add to

$$\frac{1}{\tau_{total}} = \frac{1}{\tau_{AC}} + \frac{1}{\tau_{LO}} + \frac{1}{\tau_{Ion.I.}} + \frac{1}{\tau_{e-e}} + ... \tag{3.45}$$

Unfortunately, an accurate calculation of τ_{total} is not feasible for terahertz transitions[94]. Measurements reveal typical lifetimes for transitions below LO phonon energy between 30 and 300 ps[95][96] at low temperatures and <10 ps when thermally enabled LO phonon emission prevails[97].

3.5. Rate Equations

In the previous sections, the microscopic modeling of the intersubband transitions involved in the emission process yielded expressions for the state lifetimes τ. Even though the calculation of τ is difficult for THz QCLs[94], one can gain helpful insight into the interplay of state lifetime, optical losses, gain cross section and pumping current on the basis of rate equations.

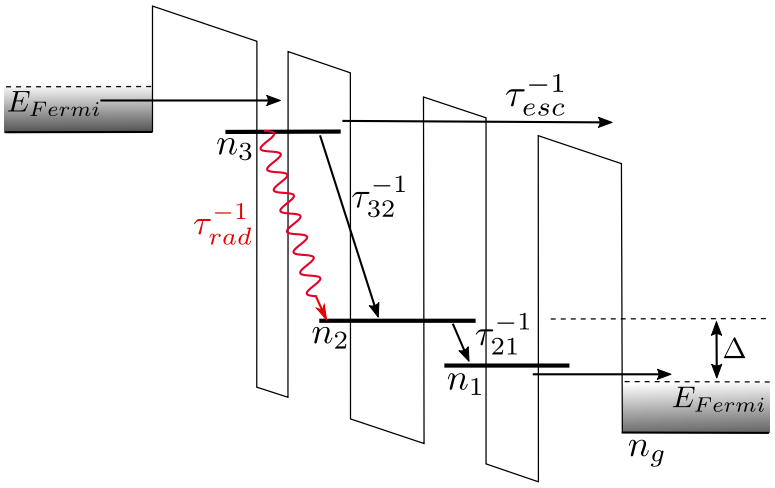

Figure 3.5.1.: Energy states and electron transitions in a basic three QW system. Adapted from [72]

These equations couple the dynamics of upper and lower laser level carrier density n_i and the photon flux S. For a three-level system, the rate equations are (see [98]):

$$\frac{dn_3}{dt} = \frac{J}{q} - \frac{n_3}{\tau_3} - Sg_c(n_3 - n_2) \tag{3.46}$$

$$\frac{dn_2}{dt} = \frac{n_3}{\tau_{32}} + Sg_c(n_3 - n_2) - \frac{n_2 - n_g e^{-\Delta/kT}}{\tau_2} \tag{3.47}$$

$$\frac{dS}{dt} = \frac{c}{n}\left[S(g_c(n_3 - n_2) - \alpha) + \beta\frac{n_3}{\tau_{sp}}\right] \tag{3.48}$$

For simplicity, the lowest laser level $n = 1$ is omitted here, and the ground state of the injector/relaxation region is considered instead. The upper level $n = 3$ is continuously populated by a current density J. The carriers in this state have a lifetime τ_3 before they scatter non-radiatively into other states or the above-barrier continuum, therefore the level is depopulated at a rate n_3/τ_3. In addition, stimulated emission occurs at a

rate proportional to the population inversion $(n_3 - n_2)$ times photon density S and gain cross section g_c.

This is similar for the lower level $n = 2$: population channels are scattering from the upper level into the lower one at a rate $n_3/\tau_3 2$ and the stimulated emission, now with a positive sign. The last term includes the scattering out of level 2 at rate n_2/τ_2 and accounts for the so-called "backfilling", a thermal population of level 2 from the ground level where T is the electron and lattice temperature, both of which are assumed to be identical in the injector region and Δ indicates the energy difference between the Fermi level in the relaxation region and level 2.

Finally, the change in photon density S takes into account that the amplification is counteracted by the total losses α and includes a term for the spontaneous emission with a factor β to restrict the rate to only photons emitted into the considered lasing mode. This factor is typically small ($\beta \approx 0.001$) and can mostly be neglected.

With this groundwork, it is now possible to give an expression for the threshold current, at which the gain overcomes the losses and S suddenly rises. The way to do this is to set $dn_{1/2}/dt = 0$ and $S = 0$ to obtain

$$J_{th} = \frac{q}{\tau_3} \frac{\left(\frac{\alpha}{g_c} + n_2^{therm}\right)}{1 - \frac{\tau_2}{\tau_{32}}} \tag{3.49}$$

where $n^{therm} = n_g e^{-\Delta/kT}/\tau_2$ is the thermal backfilling rate.

This rate equation approach is not exclusive to QCLs. In a more or less similar form, they can be applied to any laser; further reading can be found e.g. in [99].

3.6. Design of the Gain Medium

The active region is the heart of a QCL, and its design profoundly impacts the device's characteristics. Improvement of output power and operating temperature is usually the focus of development, although sometimes more nuanced aspects influence the design, e.g. Stark effect tunability or broadband gain. The peak material gain (see eq. 3.40) is proportional to the square of the intersubband dipole matrix element $|z_{ij}|^2 = |\langle\phi_i|z|\phi_j\rangle|^2$ and the population inversion $\Delta n = (n_i - n_j)$. Both of them are targets for optimization.

The first decision to be made before any development is done on the band structure, is the choice of the material system. In the mid-infrared several well-studied compositions based on III-V-semiconductors have been established, primarily based on InGaAs/AlInAs structures. This system was also used in the first-ever demonstrated QCL [39] and offers

beneficial properties such as low effective electron mass improving the intersubband dipole matrix element and a Γ-point conduction band offset of more than 500 meV which is preferable to minimize electron escape into the above-barrier continuum.

GaAs/AlGaAs QCLs were first realized at 9.4 µma few years later[100]. However, their performance is not as good as for InGaAs/AlInAs devices due to higher effective electron mass and lower conduction band offset (≈ 390 meV). A promising alternative is the InAs/AlSb combination that theoretically yields excellent results, although despite demonstration of working lasers[101] they are not yet competitive due to fabrication and growth difficulties.

At terahertz frequencies, QCLs are usually fabricated on GaAs/AlGaAs material systems which exhibit superior performance compared to others, especially concerning the maximum operating temperature, including InGaAs/InAlAs, InGaAs/InAlGaAs and InGaAs/GaAsSb[103][104].

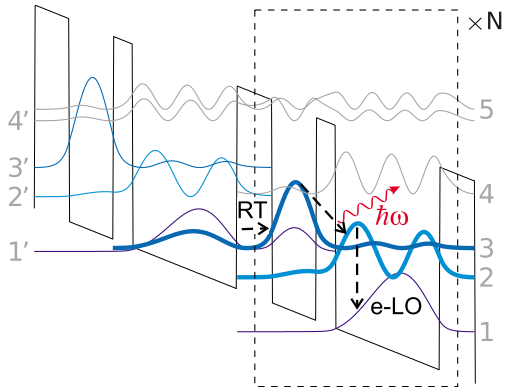

Figure 3.6.1.: Conduction band diagram of a 4.6 THz two-well design with diagonal transition by Kumar et al.[102]. Only two quantum wells and three energy levels are needed to attain a high enough population inversion for operation up to 121 K.

Active region heterostructures for THz QCLs are generally categorized into three different schemes: Resonant-phonon, bound-to-continuum and chirped-superlattice designs.

The **resonant phonon** design is usually implemented as a two-, three- or four-well system.

The general design challenge at terahertz frequencies is the low photon energy, which is smaller than the optical phonon energy in contrast to mid-IR QCLs. In addition, the thermal energy is significantly closer. The most simple case, the two-well design without further injection or relaxation regions[102] is an excellent example to demonstrate the basic working principle of population inversion through resonant phonon extraction. The involved electronic states are reduced to the absolute minimum of three levels, namely an upper (3) and a lower (2) laser level and an injector level (1) that serves to both extract electrons from the lower laser level and inject them into the upper level of the adjacent cascade. The transition $2 \rightarrow 1$ is longitudinal optical phonon-mediated since the energy separation is $\Delta E_{21} = \hbar\omega_{LO} = 37\,\text{meV}$ resulting in sub-picosecond carrier state lifetimes. Injection from level 1 into the upper laser level of the following cascade occurs by resonant tunneling through the well barrier.

By the addition of a third quantum well above the 2-well structure, the injection effi-

ciency can be improved by extending the wave function further into the injection barrier, e.g. used in the first QCL design[39] or, depending on the thickness, creates a vertical laser transition with the associated improved upper state lifetime[105]. Three-well THz QCLs have also been developed as a simplification of four-well constructions[106].

A four-well system, such as first developed by Hofstetter et al.[107] for short wavelengths, improves the population inversion by adding an additional anti-crossed state below the lower laser level. This helps the efficient carrier extraction from this level since backfilling is reduced and is called the double phonon resonance design. A different reason to add a fourth QW is the suppression of parasitic current in THz QCLs due to direct phonon-mediated scattering from the upper level to an extractor state bypassing the lower laser level. Interposing the fourth well spatially separates the wave functions and decreases their overlap, thereby reducing J_{para}.

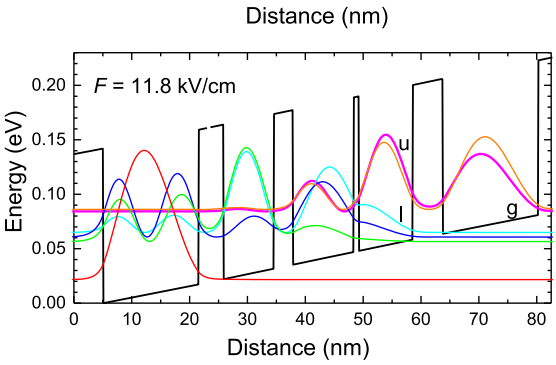

Figure 3.6.2.: Conduction band diagram of a 4.7 THz four-well design by Ohtani et al.[2]. A fourth QW is inserted between the laser-active wells and the extraction well to reduce parasitic current.

Chirped superlattice QCLs involve more quantum wells, typically 7-9, arranged so that their individual states are close enough to form so-called "minibands" due to their intrinsic broadening. The radiative transition then occurs at the "minigap", i.e. between the lowest state of the upper and the highest state of the lower miniband. Population inversion at the miniband edges emerges naturally without resonant phonon scattering because intra-miniband scattering is much faster than scattering between them. The chirping is not necessary for the appearance of minibands but compensates for the electric field under operating conditions.

Bound to continuum active regions improve on the chirped superlattice design by using a miniband edge as the lower laser state but replacing the upper band edge in the radiative transition with an additional state that lies within the minigap. This state is created by adding a quantum well directly after the injection barrier. This serves two purposes: First, the injection process is more similar to a two- or three-well design in that coupling from the injector states to the upper laser state can be engineered to occur through a more selective tunneling process since the spatial extension of the BTC upper laser state into the injection barrier is much higher than the miniband states. Secondly, the radiative transition becomes more diagonal, reducing the spatial overlap of the laser active states. While this leads to decreased oscillator strength, the upper

state lifetime benefits from this, which can improve temperature performance[108][92]. This design first found application in the mid-IR[109] and has also been extended to the THz[110].

The active regions discussed above are usually cascaded on the order of 100 times in a typical THz QCL and around half of that in mid-IR QCLs with the goal of maximizing the overlap factor of the active region and the waveguide mode. One aspect that has not been mentioned so far is doping. While any doping raises free carrier waveguide losses and promotes ionized impurity scattering, and is therefore kept to a minimum wherever possible, it can not be dropped entirely[111]. The reason for this is electric stability and uniformity of the field, which is not given in Superlattices where electric field domains tend to form. Doping prevents this by compensating the negative charges and additionally enables operation of the device at a stable point of the I-V curve[98].

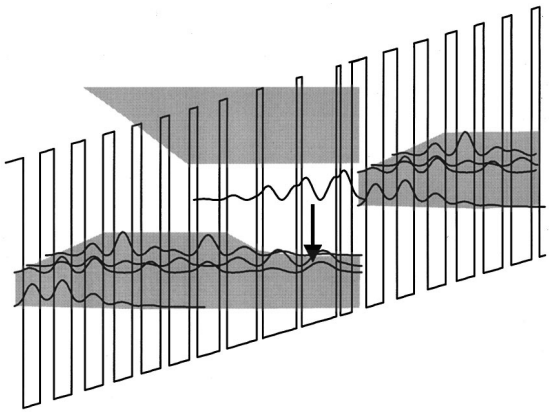

Figure 3.6.3.: Conduction band diagram of a 9.1 µm bound-to-continuum design by Faist et al.[109].

3.7. Terahertz QCL Waveguides

A crucial part of any laser is the waveguiding structure that confines the optical mode and provides a resonant cavity for amplification. The properties of this resonator, such as electromagnetic losses, confinement factor and free spectral range naturally have a high impact on the macroscopic laser characteristics, in particular threshold current, output power and efficiency, beam quality and frequency.

Semiconductor lasers operating at visible or mid-infrared wavelengths commonly employ dielectric waveguides consisting of a ridge with refractive index n_1 surrounded by a different material with refractive index $n_2 < n_1$. Because of total internal reflection at the dielectric interface, the mode is contained mostly within the ridge except for a small evanescent field outside. Dielectric losses are typically low at high frequencies, and this type of waveguide can be manufactured without additional metalization steps.

At terahertz frequencies on the other hand, this setup is unfavorable. It is necessary to use highly doped materials in the electrical contact layers on top and bottom of the active region, which would lead to unacceptably high free carrier losses that scale

with the wavelength squared. The solution is to use metallic waveguides, whose losses decrease with lower frequency.

The calculation of the fields confined by these waveguides is done by solving Maxwell's equations. If the considered volume is assumed to be source free, non-magnetic and nonconducting and the field dependency in propagation direction is given by $\exp(ik_x x - i\omega t)$ the Maxwell equations can be combined into Helmholtz wave equations[112] for $\boldsymbol{E}$ and $\boldsymbol{H}$

$$\begin{aligned} \nabla^2 \boldsymbol{H} + \frac{n^2\omega^2}{c^2}\boldsymbol{H} &= i\omega\varepsilon_0(\nabla n^2) \times \boldsymbol{E} \\ \nabla^2 \boldsymbol{E} + \frac{n^2\omega^2}{c^2}\boldsymbol{E} &= -\nabla\left[\frac{1}{n^2}(\nabla n^2)\cdot\boldsymbol{E}\right] \end{aligned} \tag{3.50}$$

where $n = \sqrt{\varepsilon\varepsilon_0}$. This can be extended to include perfect electrical conductors by implementing the respective boundary conditions, but dealing with dispersive metals requires significantly more work.

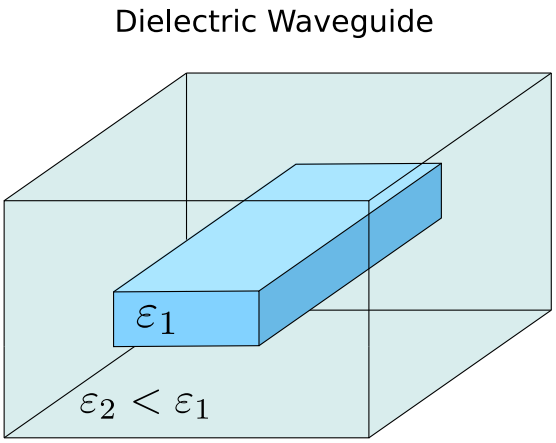

Figure 3.7.1.: A simple dielectric waveguide often preferable at visible and near-infrared wavelengths due to its easy fabrication and low losses at these frequencies. The necessarily high doping of the cladding material makes this arrangement unfavorable for THz QCLs because of free carrier losses.

In general, THz QCLs use two different waveguide types: Plasmonic waveguides and double metal waveguides[113]. The plasmonic types come in a few varieties, but mostly the *semi-insulating surface plasmon* form is used. *Double metal* waveguides on the other hand are essentially microstrips with the active material ridge as the dielectric. Common to both is the excellent mode confinement factor Γ, which allows avoiding a large overlap with lossy, highly doped regions leading to low losses compared to mode guiding by doped cladding layers.

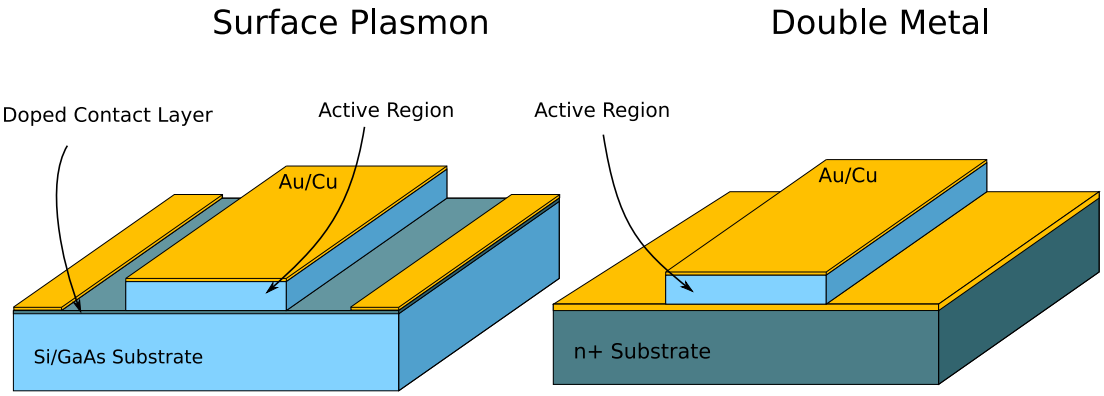

Figure 3.7.2.: a) Semi-insulating surface plasmon waveguide. **b)** Double metal waveguide

The SI-surface plasmon waveguide was used in the design of the very first THz QCL by Köhler et al.[41]. This approach is based on the fact, that gold (and other metals, in particular noble metals) have a large negative real part of the dielectric constant below the plasma frequency, as explained by the Drude model. At the interface between such a material and another one with a positive dielectric constant (e.g. GaAs below a certain doping concentration), the formation of *surface plasmon polaritons* is possible, electromagnetic surface waves traveling along the interface. Similar behavior is seen in heavily doped GaAs[114]. This way, a gold strip on top of the active region together with a buried so-called plasma layer made from GaAs doped in excess of $1 \times 10^{18}\,\mathrm{cm}^{-3}$ can confine the mode. At the same time, the latter acts as a current path to bias the active region. Free carrier losses are kept low when the plasma layer thickness stays significantly below the field penetration depth. The mode then extends into the semi-insulating substrate and has a low overlap with the doped region. This construction is popular because of the reduced fabrication complexity since the structure can be built from bottom to top by growth and etching steps with a single metalization process.

Another type of terahertz waveguide, called double metal or metal-metal waveguide, is more complex to fabricate but expected to have lower losses and a better confinement factor. Its working principle is similar to a microstrip resonator known from HF electronics. The active region is sandwiched between a metalized surface and another metallic layer on top of the laser ridge. The modal overlap with the active region is higher than with any other waveguide type ($\Gamma \geq 0.9$), while the remaining losses are primarily due to the non-perfect conductivity of the metal layers and the doping necessary in the injector and the ohmic contacts. Eventually, the good thermal conductivity of the metal is desirable to efficiently transport heat away from the active region, which is particularly beneficial to the effort to push for Peltier-cooled solutions. Double-metal cladding layers made of copper instead gold enable some of the highest operating temperature QCLs

due to optimized thermal conductivity and improved losses[115][116]. Altogether these favorable attributes enable some of the best-performing devices regarding threshold current, operating temperature and output power, especially for the lower end of QCL frequencies. As opposed to surface plasmon structures, this buildup requires a sensitive wafer bonding step since the active region can not be grown directly on a gold surface.

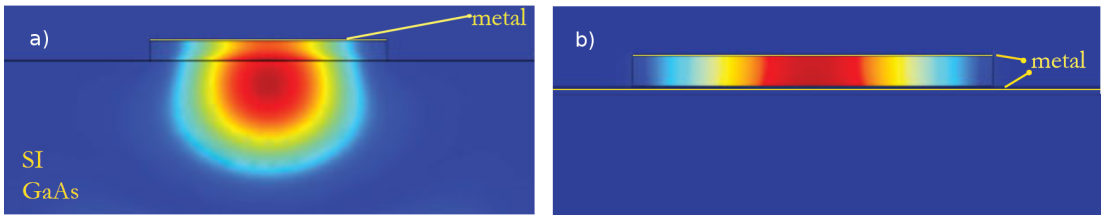

Figure 3.7.3.: Electric field strength calculated for **a)** surface plasmon waveguide and **b)** double metal waveguide. Reproduced from [94]

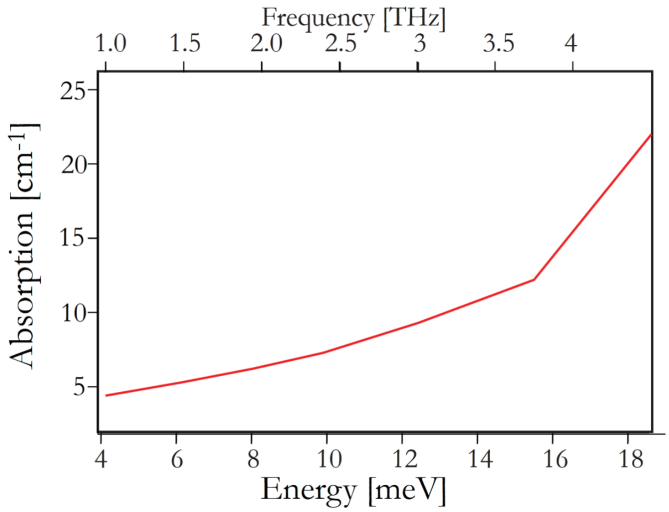

Figure 3.7.4.: Frequency dependent losses calculated for a double metal waveguide excluding the active material. Reproduced from [94]

One problem concerning practical applications of double metal QCLs is the beam pattern of the outcoupled light that arises from the sub-wavelength output facet dimensions, often resulting in patterned and highly divergent far fields. Additionally, this leads to high reflection at the outcoupling facet, which can be detrimental to the total power output. Several solutions have been proposed, including external arrangements like silicon lenses or horn antennas directly attached to the output facet and on-chip patch antennas[117] or Vivaldi antennas[118].

3.8. Mode Control in QCLs

The radiation field in a laser is determined by the resonator or laser cavity. For a laser design where oscillation occurs between two reflectivities, such as mirrors for gas lasers or facets in the case of semiconductor lasers, the emission wavelength is predominantly selected by the gain profile of the active medium and the position of the longitudinal Fabry-Perot modes. The cavity modes intrinsically satisfy the first condition for the appearance of lasing: after one round trip within the cavity, the phase delay is $2\pi n$ to produce constructive interference. The second condition is that the considered mode reaches threshold gain, which means that the amplification of the wave is able to overcome the total losses while traveling back and forth in the resonator. This can be written as

$$g_m = \alpha_i + \alpha_m = \alpha_i - \frac{1}{2L}\ln(R_1 R_2) \tag{3.51}$$

where g_m is the modal gain, $R_{1/2}$ are the mirror reflectivities, α_i is the internal loss and α_m is the loss from outcoupling at the mirrors. The second equality follows from the steady-state condition

$$\sqrt{g_{RT}} = R_1 R_2 e^{(g-\alpha_i)L} = 1 \tag{3.52}$$

since the roundtrip gain above threshold is always unity after equilibrium has been reached. Since the gain profile is not uniform, the cavity mode closest in frequency to the maximum of this curve will arrive at threshold first and start to oscillate when the bias current (or any other laser pumping method) increases during startup. This mode will then saturate the gain, which means the photon density increases while population inversion is reduced through stimulated emission until a balance is found and the process stabilizes[119]. If other effects are neglected, this gain saturation induces single mode operation and is referred to as gain competition or mode competition. This mode suppression effect can also be observed in dual-wavelength lasers where two different gain regions share the same resonator[120]. In reality, achieving single mode operation is often difficult because the interaction is more complex. One significant effect is *spatial hole burning*. The field density inside the gain medium is not uniform but modulated by the standing wave nodes forming the active mode. Therefore, gain saturation occurs only localized. Another mode with low enough spacial overlap does not experience the gain competition necessary to prevent it from lasing and a stable multimode regime can

exist[121].

The precise control of the laser-active modes is often required of lasers operated in spectroscopy, communication or metrology environments for two reasons: For one, many applications work with an isolated wavelength and perform poorly or not at all with multi-mode lasers. In addition, the wavelength must be strictly specified, e.g. in difference-frequency setups or cold matter excitation experiments. Normally any mode-instability is therefore undesired.

It is not surprising that the shape of the gain profile and its peak, which ultimately depends on the energy of the intersubband transitions, might change under variable operating conditions of the laser. The applied bias voltage distorts the quantum wells and shifts the state energies, producing a large quantum-confined stark effect[122]. The shift of the gain profile with increasing voltage is seen in the electro-luminescence spectrum[123] and change of active modes[124]. This can induce mode jumps when the peak of the gain profile shifts far enough to align with the next cavity resonance. Typically a hysteresis in the selection of the active modes is observed when the voltage is changed.

A widespread approach to promote single-mode operation at a selectable wavelength is a *distributed feedback* structure (DFB)[125][126]. Here the laser resonator features a periodic change in the effective refractive index of the waveguide, which acts as a frequency-selective element. Periodic optical structures have gained traction in the physical community, partly because of their intriguing similarity to solid state electron physics, under the name "photonic crystals". A DFB laser can be considered a one-dimensional photonic crystal in this context.

Similar in design and purpose to DFB structures are Bragg reflectors (DBR)[127], the difference being that the periodic refractive index modulation is not spread over the entire laser ridge. Instead, one or both end mirrors are constructed as periodic structures conceptually similar to dielectric mirrors used at Vis/IR wavelengths. Reflection occurs only within a defined frequency band, enhancing the Q-factor of any mode within this range while modes outside experience losses from transmission through the DBR.

DFB and DBR designs both aim to fix the active laser mode to a given frequency and concurrently suppress any mode jumps. A more flexible approach, although not as universally applicable, are coupled cavities. If one of the cavities is slightly longer than the other, their individual modes line up at wavelengths corresponding to the "beat" of the free spectral ranges and determine the lasing mode. With a slight change in refractive index, e.g. due to heating, this *vernier effect* shifts to align the adjacent two cavity modes and separate the previous ones, which then cease lasing. This way, combining single mode operation with dynamic wavelength selection over a broad range

is sometimes possible.

A particular case with great potential for spectroscopic applications is mode-locked operation. In this state, several longitudinal modes are active simultaneously, but unlike normal multimoding, their phase relationship is fixed in such a way that a wave packet travels back and forth within the laser. The laser emission consists of a pulse train, where the delay between pulses corresponds to the cavity roundtrip time. The spectrum of such a pulse train resembles a frequency comb, i.e. many intensity peaks of precisely equal distance. For passive mode locking, a saturable absorber within the resonator is often used. This concept is technologically mature at optical and infrared wavelengths, where Ti:sapphire or fiber lasers have found widespread application. Mode-locked terahertz QCLs, on the other hand, are more challenging to realize. The low upper state lifetime and consequentially fast repopulation are detrimental to the formation of a pulse in the cavity. Active mode-locking techniques based on injection of an HF signal in resonance with the cavity round trip frequency have been demonstrated[128][129].

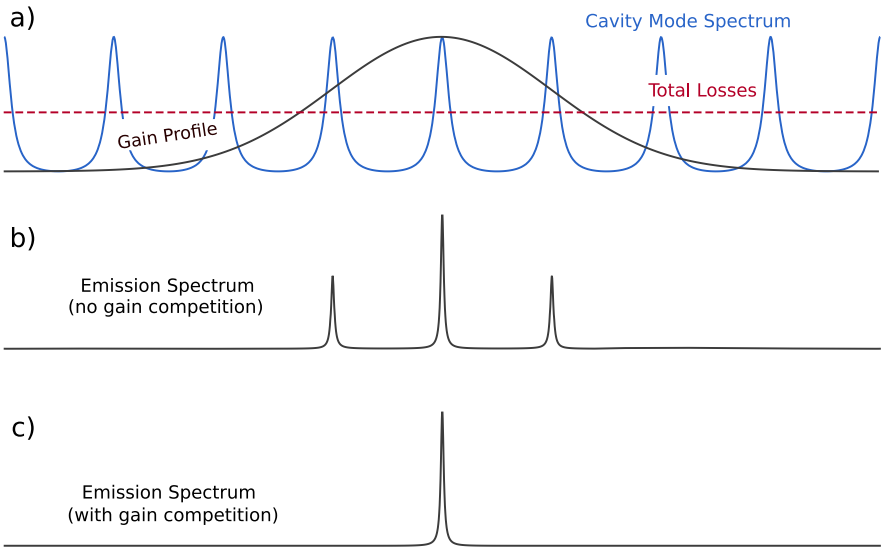

Figure 3.8.1.: A simplified overview of the contributions from the cavity mode spectrum and the gain profile to the above-threshold emission spectrum of a laser. It is common to apply further frequency selective structures to achieve single-mode emission.

Chapter 4.

Tuning of THz QCLs

Dynamic control of the emitted wavelength of a coherent radiation source such as a laser is often desired. The most obvious applications include scanning through a spectrum to record absorption spectra or excite radiative transitions in emission spectroscopy. When used in a heterodyne system, the frequency is usually fixed, but adjusting the local oscillator frequency is necessary to define the observed frequency window. Even for applications that only require lasers at a very specific frequency, tuning capability is not pointless. External influences such as optical feedback, temperature changes or aging processes can negatively impact stability on all timescales and often require a control mechanism, e.g. with a phase-locked loop. Finally, the exact wavelength of a finished laser is not entirely predictable due to manufacturing tolerances. There is little room for deviation in many cases, e.g. when measuring a molecular absorption line. The ability to tune the laser reduces the number of unusable devices in a production run. Not all tuning requirements are equal, and no tuning mechanism can satisfy all of them. While a frequency scan is often done comparably slowly, it can require large tuning ranges. External cavity lasers are one possibility to achieve that. A phase-locked loop on the other hand needs a fast response of the oscillator to tuning inputs while tuning range requirements are less demanding. This can be provided e.g. by current tuning. Ease of implementation or robustness in rough environments can also limit available choices.

Tuning of THz QCLs has proven difficult in the past. After more than 20 years of development, no widely adapted approach to this problem has been found that provides a large tuning range with a continuous wavelength map while keeping the structure simple with a minimum of external parts or moving elements. A short overview is given here as background and for comparison to the on-chip tuning approach investigated in this work.

4.1. Current and Temperature

Changing the bias current or the chip temperature is the easiest way to tune a QCL, and works with any device, although the effectiveness is not always the same.

Temperature tuning is based on two independent effects, specifically the change in refractive index with temperature dn/dT and the thermal expansion or contraction of the cavity. The refractive index temperature coefficient of GaAs is always positive[130], which means that the optical length of the cavity increases with temperature. The thermal expansion coefficient is also positive, adding to the effect. This cavity optical length increase leads to a movement of the cavity modes towards lower frequencies (since the mode spacing decreases) when the temperature rises[131].

Similarly, tuning by current is multicausal as well. Obviously, a higher current will increase the active region temperature, leading to the effects described above, but besides that, two more fundamental current tuning mechanisms are present in QCLs. The first is caused by the change in gain, which can be treated as a change in the extinction coefficient κ of the complex refractive index $\tilde{n} = n + i\kappa$. The real and imaginary parts are intertwined by the Kramers-Kronig relations[99], and therefore a variation of the gain induces a change in the real part of the refractive index[132].

The second contribution results from the Stark effect[122]. This effect causes a shift of the intersubband transition energies and consequently of the gain profile maximum[133]. Repositioning the gain profile maximum again changes the refractive index and the dispersion through the Kramers-Kronig relations. If the shift is large enough, mode jumping will occur.

4.2. Coupled Cavities

Two coupled cavities of different lengths can provide an intriguing dynamic mode selection mechanism. The underlying principle is based on the frequency and phase matching requirement of the two longitudinal cavity modes if the coupling is strong enough. In an appropriate design, this is the case only for a single mode combination of the two cavities before the active medium gain roll-off prevents lasing, thereby selecting a single active coupled-cavity mode, sometimes referred to as Vernier resonance. This approach is not unique to QCLs and has been used in other lasers. A gap can be added to an existing semiconductor laser ridge with focused ion beam milling to create the coupled cavities[134][135]. If both cavities are of the same length, then the emission frequency can be electrically or thermally tuned similarly to a single cavity. If the optical length is different (or the cavities can be independently biased or heated), this small

tuning range of the individual cavities can be combined to select the resulting coupled lasing mode within a much larger bandwidth by aligning two other resonances of the two cavity mode spectra. A discrete tuning bandwidth of more than 100 GHz has been demonstrated this way in THz QCLs [136]. On the downside, the continuous tuning range is reduced in this setup. A model of the mode interactions using a scattering matrix method and reduced rate equations is given in [137].

4.3. External Cavity

EC semiconductor lasers are used extensively to produce large tuning bandwidths by mechanical manipulation of the oscillator from laser diodes that are insufficiently tunable under normal circumstances. Here one of the laser facets is anti-reflective coated, and a separate mirror placed at a distance acts as the second reflector. The cavity length and emission frequency can then be changed by the position of this mirror. Of course, the FSR of such an extended cavity is small; therefore, lasing often occurs simultaneously on many longitudinal modes. Achieving single mode operation can be difficult. An improvement are the Littrow or Littman configurations [138] that use grated mirrors to provide further wavelength filtering. In the predominantly used Littrow configuration the external mirror provides wavelength dependent feedback controlled by the grating angle. If the anti-reflection coating is good enough it becomes possible to tune the emission to any EC mode within the gain bandwidth. With a significant residual facet reflectivity the setup behaves similar to a coupled cavity where only EC modes close to the Fabry-Perot modes of the laser chip are accessible. Translational movement of the grating mirror enables the continuous shift of the emission frequency within one FSR.

4.4. Lateral Cavity Mode Manipulation

Variable positioning of the resonators is not the only way to mechanically manipulate the effective laser cavity length. The electromagnetic field will extend into the surroundings of any waveguide structure that does not completely encapsulate the active medium in a conductive material. This is also the case for metal-metal QCLs and opens up the possibility of manipulating the mode laterally. This approach has been demonstrated with remarkable success on wire-laser geometries, i.e. lasers with comparatively thin and long ridge dimensions that promote a substantial lateral leaking of the electromagnetic field. By bringing a metal plunger close to the ridge sidewall, the field is "squeezed" into the active region's high permittivity material, increasing the effective refractive

index experienced by the laser mode. Tuning ranges of 330 GHz have been observed [139] [140].

4.5. Optical Excitation of the Semiconductor Substrate

A change of the refractive index in semiconductors can be induced through the injection of free carriers by illumination with photons exceeding the band gap energy[141]. This principle can be used to change the optical length of a semiconductor laser resonator by adding an external light source. The high radiance necessary for robust tuning requires light sources such as laser diodes. Published experiments on QCLs designed for 3.1 THz achieved 2.8 GHz tuning with a 760 nm laser diode mounted on the same carrier and illuminating the back facet of the QCL in CW mode[142]. Improvement is possible with fiber-coupled laser diodes that allow more accurate placement of the radiative power on the QCL. Particularly good results were accomplished by illuminating the non laser active substrate of a surface plasmon QCL enabling 40 GHz of tuning[143]. The method allows fast tuning and can be used for stabilization feedback loops for frequency and optical power output[144].

Chapter 5.

On-Chip Tuning using a Movable Reflector

This chapter introduces a novel tuning approach based on a movable cavity reflector. The underlying idea and its advantages over previously published tuning mechanisms is outlined.

The computer model used to perform simulations is presented. The results from it lead to the initial laser design by providing the optimal dimensional parameters of the structure. The model is further used to evaluate the impact of given manufacturing capabilities and the requirements regarding tolerances and mechanical accuracy.

The key components of the new laser are investigated separately and optimized for an ideal functional interaction. The experimental setup used for subsequent measurements on the fabricated devices is shortly summarized.

5.1. Introduction

The cavity design of the THz QCLs used by our workgroup in the past is hardly responsive to attempts at mode manipulation from the outside since the metal-metal design and the flat ridge result in minimal electromagnetic field leakage. The fundamental idea of the tuning mechanism is the extension of the intracavity mode to a tuning section that leaks substantially more in the lateral direction and allows the setup of a reflector at a selectable position. This is hardly possible with the gold-covered GaAs structures that usually are the building blocks of metal-metal QCLs due to the high refractive index of GaAs that implicates a high confinement factor. The Benzocyclobutene (Cyclotene 3022-5) planarization process successfully used in other patch antenna designs [117][145] opens up a new angle to tackle this problem since the refractive index of BCB is lower

compared to GaAs[146], thereby reducing the confinement factor. This allows the construction of the tuning section.

For a successful design, the following main questions must be answered: First, the construction of the tuning section regarding its shape and size must be determined such that a movable reflector has access to the electric field with sufficient overlap. Then the form of the reflector and its mechanical properties can be worked out. Finally, a solution for the transition from the GaAs ridge to the BCB-based tuning section must be found that minimizes unwanted reflections at this point.

The most simple tuning section is a narrow "microstrip" on the BCB layer. As the impedance mismatch between the laser ridge and this microstrip is large, a wideband matching structure is necessary to allow a reflection-free transition of the laser mode to the tuning section. This can be provided by a continuous, tapered top metallization and a triangular shape in the GaAs laser medium beneath it (see Fig. 5.1.1). These general design ideas are modeled in CST Microwave Studio™ and iteratively improved with regard to performance, simplicity and robustness until a satisfying solution is found.

The movable reflector consists of several gold stripes perpendicular to the tuning section that are lithographically etched onto a thin silicon membrane. The membrane can be put in position with a piezoelectric 3-axis stage by mounting it at a downward angle and allowing the material to bend when the membrane is lowered onto the QCL. This way, the contact pressure is always controlled, and damage to neither the laser nor the membrane can occur.

When this thesis was started, the concept of tunable QCLs had been explored for some time within the workgroup and the concept of on-chip tunable devices first was conceived by M. Justen when the BCB planarization process became available at ETH Zürich[147]. The first-generation lasers investigated in chapter 6.1 had been manufactured in the Quantum Optoelectronics Group of Jérôme Faist at ETH Zürich together with the first 1.9 THz patch-antenna devices presented in Justen et al.[117]. The basic design is therefore identical to these lasers, with the addition of the tuning structures. The silicon membranes with the reflector structures were made at this time in the cleanroom facilities of I. Physikalisches Institut of the University of Cologne.

From this inital work basic CST models of the tuning section and the patch antenna were available. Aside from this, the QCLs had not been tested in any way at this point and the findings presented in this thesis are the first results for this tuning approach. Early results obtained from the first available tunable QCL have been presented at ISSTT 2019[1]. Based on this foundation, the work done by the author involves the

[1]Talk, M. Mertens: A Double-Metal QCL with Backshort Tuner. Abstract available in ISSTT 2019 Proceedings Book, p. 221

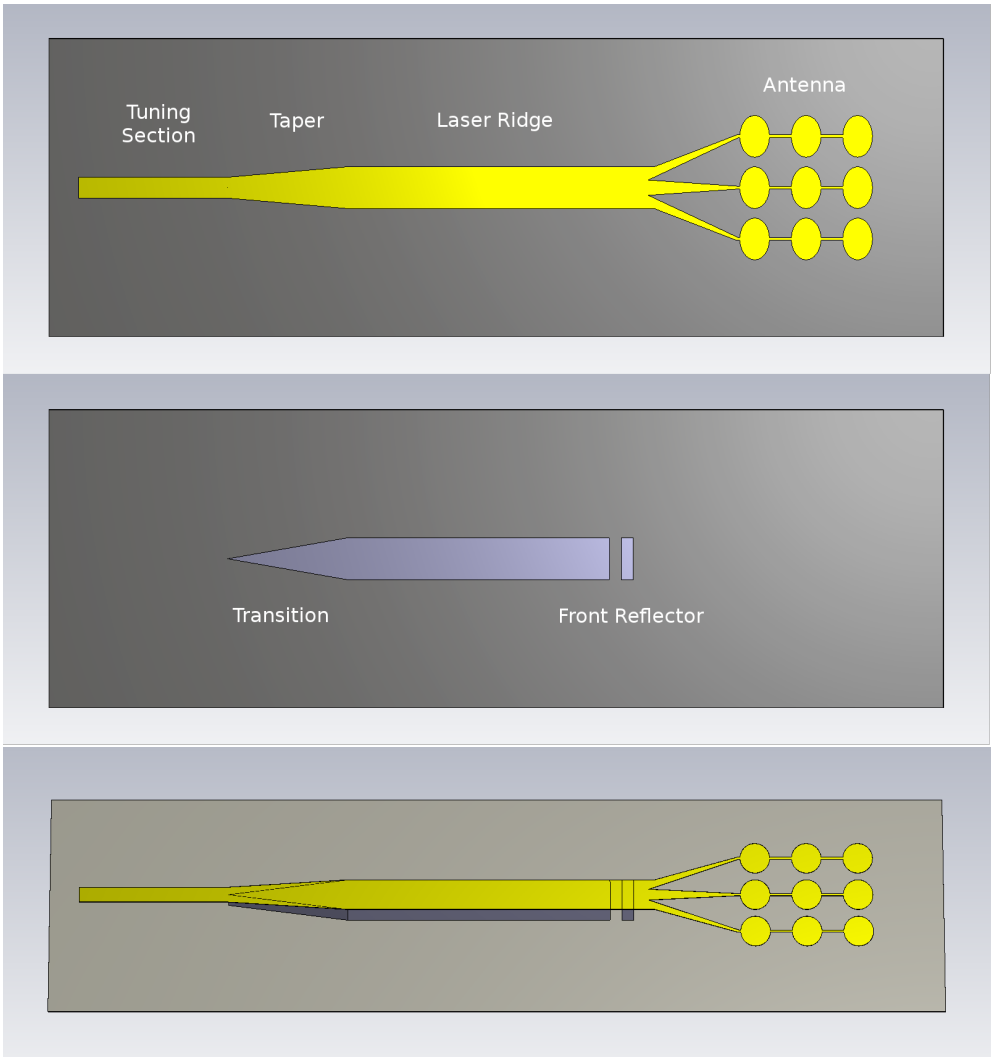

Figure 5.1.1.: Top: Top view of the basic design. Visible is the gold structure that covers the GaAs laser ridge. **Middle:** The same view without top metallization shows the underlying GaAs ridge, triangular transition and front reflector. **Bottom:** Angled view of the device. Not shown is the BCB layer that is planarized with the GaAs and supports the antenna and the tuning section. Dimensions are not to scale.

following:

1. Extension and validation of the pre-existing computer models, including aspects of reflector membrane misalignment and manufacturing deviations. This is done with CST Microwave Studio, a modeling software and field solver used successfully for several years by the instrumentation workgroups at the institute.

2. Implementation of a measurement setup that allows the evaluation of the QCLs. This includes the mechanical and optical structure, the metrology system, programming automation software with Qt5 to conduct the tuning experiments and writing Matlab scripts to assess the large amount of data produced.

3. Characterization of all presented QCLs concerning tuning performance and coherence with expectations from the simulations. In addition, potential issues are identified and analyzed in the measurement data.

4. Finding possible causes of the unexpected measurement results from several devices with available methods, e.g. microscopy and white light interferometry. The CST models are refined to calculate the impact of the identified or hypothesized issues. A consistent explanation for the phenomena observed in the first-generation QCLs is worked out by supplementing the computer model with an analytical explanation.

5. Proposing solutions to the identified issues. Based on that, the second generation of QCLs is designed by the author and manufactured at ETH Zürich. The new devices are evaluated in a similar way to the first generation.

5.2. Design and Simulations

The numerical simulations of the individual components of the devices are carried out with CST Microwave Studio, a commercially available 3D field solver[2]. The software package incorporates several solving methods, of which the time domain solver is the most appropriate one in our case regarding efficiency and accuracy. The simulated structure is excited through 2-dimensional waveguide ports with a time domain pulse that contains all frequencies within a given bandwidth. The calculation is carried on until the energy contained in the system is diminished through absorption, radiation or transmission through any of the ports below a defined threshold value. The possible lateral modes for each port are automatically determined by satisfying the Helmholtz

[2]https://www.3ds.com/de/produkte-und-services/simulia/produkte/cst-studio-suite/

equation for the distribution of metals and dielectrics within the port plane. Only the fundamental quasi-TEM mode characteristic of microstrip-like structures is considered in the initial design process. This mode has the highest spatial overlap with the laser-active material and was expected to experience the highest gain, favoring it over higher-order lateral modes.

The reality of manufacturing also imposes another general requirement on all parts of the design: robustness against deviations from the model due to process tolerances. These deviations can change the outcome significantly in some circumstances and must be considered during the design phase. They include:

- The etching process is not perfect and can produce over/underetching and non-vertical walls
- Small features such as corners tend to be rounded or truncated during etching
- Dimensional precision of the lithography
- Misalignment of the GaAs and gold layers
- Planarization of the GaAs structures and the BCB layer is never perfect
- Sputtered gold tends to perform worse than ideal because of impurities and crystal defects

During the design, these issues are considered and solutions that are overly sensitive to one or more of them are not pursued further. For the later design of the second generation lasers, the previously neglected BCB planarization offset was treated with a high priority.

5.2.1. Tuning Section

Starting with the numerical solution for the electric field density in the laser ridge it becomes clear that the electric field distribution is highly concentrated within the active medium, and coupling to it from the outside is inefficient (see Fig. 5.2.1). In comparison, the field extends significantly above the microstrip of the tuning section that is purely based on the BCB dielectric so that a properly designed distributed reflector on top of the section can easily terminate the cavity. While the choice of dielectric has the most impact, the field leakage is further increased by lowering the aspect ratio of the microstrip, i.e. choosing a smaller width while maintaining the height.

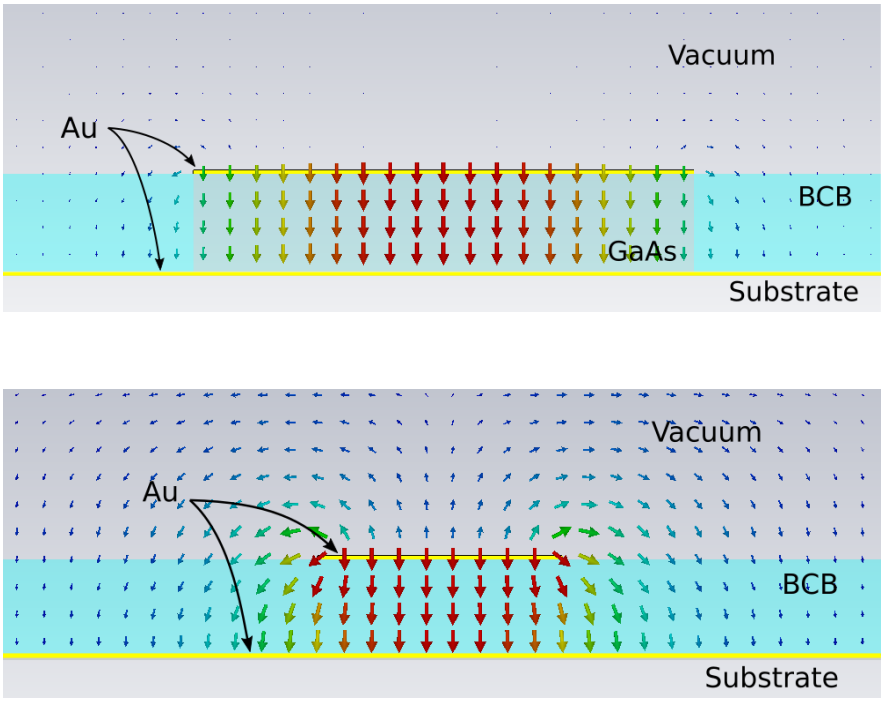

Figure 5.2.1.: Top: Electric field within the GaAs laser ridge, cut perpendicular to the longitudinal axis. Since the field extending above the ridge is weak, coupling to external structures is difficult. **Bottom:** The same electric field cut for the BCB-based tuner section. The difference in field strength outside the structure is clearly discernible.

5.2.2. Transition from Laser Ridge to Tuning Section

The transition from the GaAs laser ridge to the tuning section on BCB substrate is crucial to the concept. Reflections at this point would lead to a coupled-cavity effect and scattering of power into higher-order lateral modes could deteriorate the effectiveness of the reflector and cause overall lowered gain. A well-balanced design must be found by varying the length and angle of the tapered gold layer, the dimensions of the GaAs triangle underneath it and the width of the tuning section microstrip. The width of the laser ridge is fixed at 70µm which, as a result of prior experience, is a good value concerning optical output power and thermal dissipation.

The taper section is modeled as a 2-port device (see Fig. 5.2.2) to determine reflections and losses in the transition. Port 1 is excited by the fundamental q-TEM mode supported by the metal-metal QCL ridge. The fraction of power that arrives at port 2 at the end of the tuning section (S21) and the fraction reflected back to port 1 (S11) are evaluated to find an optimally performing solution.

The criterion to evaluate the quality of the transition design is first and foremost the reflection parameter. Nevertheless, several additional aspects must be taken into consideration. Residual reflections in the frequency band from 1.8 THz to 2.0 THz where

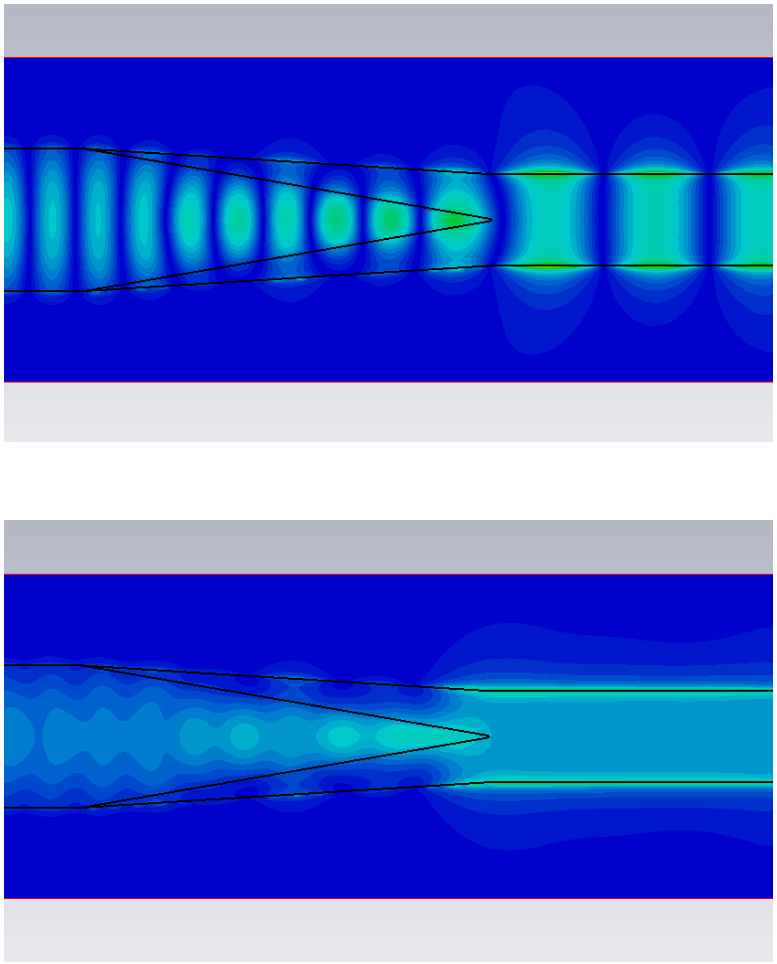

Figure 5.2.2.: Absolute value of the fundamental mode electric field at the taper section directly below the top gold layer. The instantaneous field (top) and average field (bottom) are depicted, both for the condition of total absorption at the far end. The field concentration in the GaAs triangle and at the edge of the tuner section microstrip is visible in the average field plot.

the gain is high enough to sustain oscillation would have a negative impact, such as power modulation during tuning due to phase matching conditions, impaired tuning range as a result of the formation of two coupled cavities when the reflection is high enough or in the worst case no tunability at all. In addition, a further requirement is low radiative losses to maximize the power transferred to the tuning section and the reflector and prevent surface waves from coupling to adjacent structures on the same chip.

Generally, this is achieved with a slow and gradual transition, i.e. a very long taper. Unfortunately, it can not be made arbitrarily long for two reasons. The longitudinal mode spacing decreases with a longer cavity, making it more challenging to maintain singlemode operation. Shortening the ridge to compensate for this would reduce the

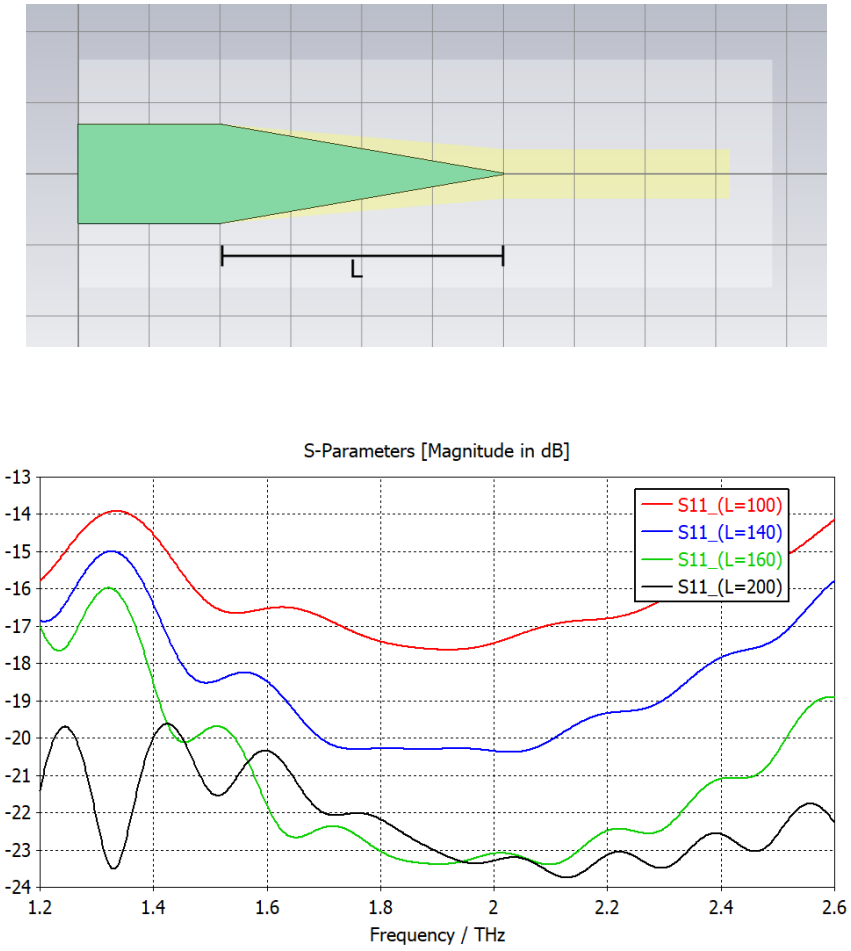

Figure 5.2.3.: Top: View on the tapered transition section with the triangular GaAs shape highlighted. **Bottom:** Length of the taper has a large influence on the reflection properties. A minimum of the S11 parameter for the 1.8 THz to 2.0 THz range is approached at around 180 µm, increasing the taper length beyond this does not significantly improve the performance.

cavity gain since the taper saturates more quickly due to field concentration and adds less amplification on the same length. The other reason is a lower limit to the angle of the GaAs triangle since a reasonable ratio of height to wall thickness must be kept for manufacturing reasons.

As it turns out, a taper length of 200 µm is a good choice. At this point, the improvement regarding reflections by further increasing the length is diminished, while at the same time, the dimensions are still within reasonable limits (see Fig. 5.2.4). The reflection coefficient simulates at better than -20 dB magnitude, low enough to suppress the aforementioned side effects.

A precondition for this is a relatively sharp GaAs wedge tip. The electric field tends to concentrate in this tip before the wave continues to the tuning section; therefore, a truncation of a few micrometers results in considerable reflection (see Fig. 5.2.4). A tip

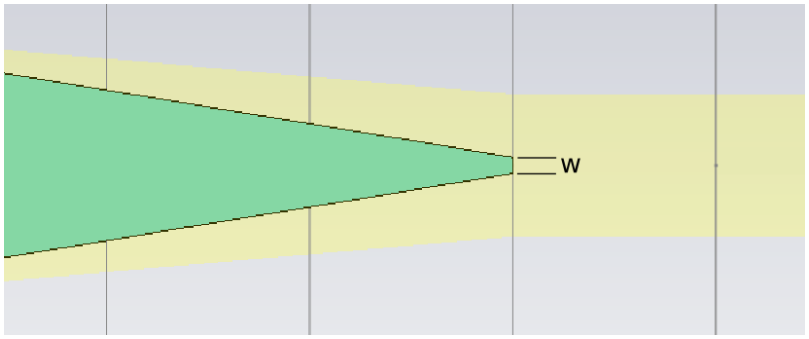

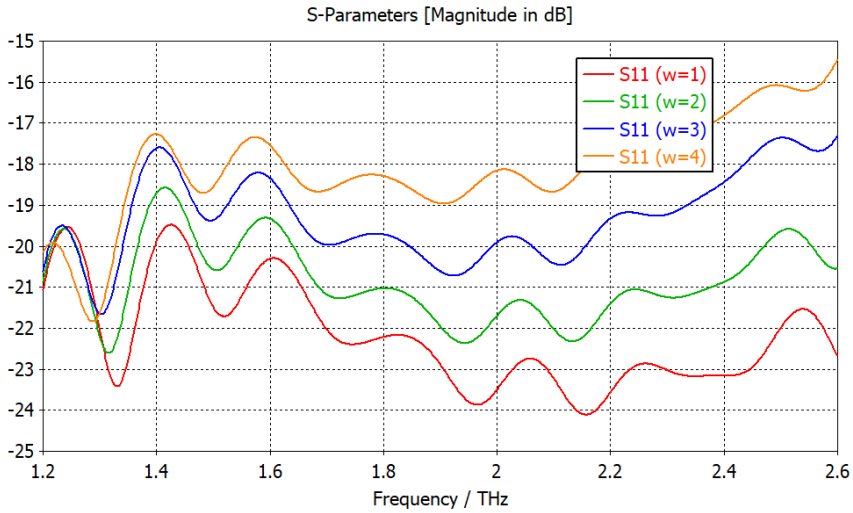

Figure 5.2.4.: The "sharpness" of the GaAs triangle tip, defined here by the width w in µm, is an important parameter for the performance. As a consequence of the field concentration in this part, manufacturing imperfections greatly impact the reflections.

of 1 µm is expected to be feasible, although this parameter might vary from device to device, even on the same wafer.

5.2.3. Movable Reflector

The heart of the tuning mechanism is a movable reflector that acts on the stray field of the tuning section, thereby controlling the cavity length to determine the frequency of the longitudinal modes. This can be achieved with an arrangement of metallic stripes perpendicular to the laser that act as a Bragg reflector when the phase condition for constructive interference in reflection is satisfied.

The dimensions and positions of the reflector stripes are determined iteratively, starting with half-wavelength spacing between stripes and using the trust-region framework implemented in CST to find an optimal solution. As it turns out, it is beneficial for

response flatness and operating bandwidth to require an increasing stripe width as a condition for the algorithm instead of searching a much higher dimensional parameter space for independent dimensions.

The choice of mechanical support for the metal strips must adhere to requirements such as mechanical stability, precise positioning and insensitivity to tolerances. As a result, an unsupported metal structure is not feasible since it is hard to manufacture and even harder to position without an unacceptable large air gap on the tuning section since any contact would either damage the device or the reflector.

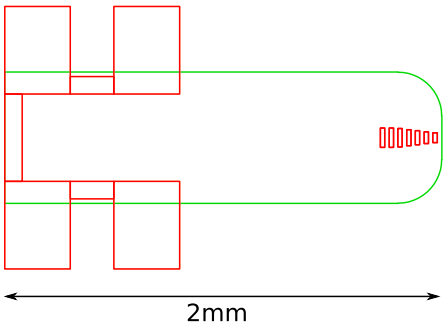

Figure 5.2.5.: Lithography mask for the reflector membrane. Silicon membrane outlined in green, gold Bragg reflector stripes in red. Also visible are free-standing gold attachments intended for easier adhesion to the positioning platform.

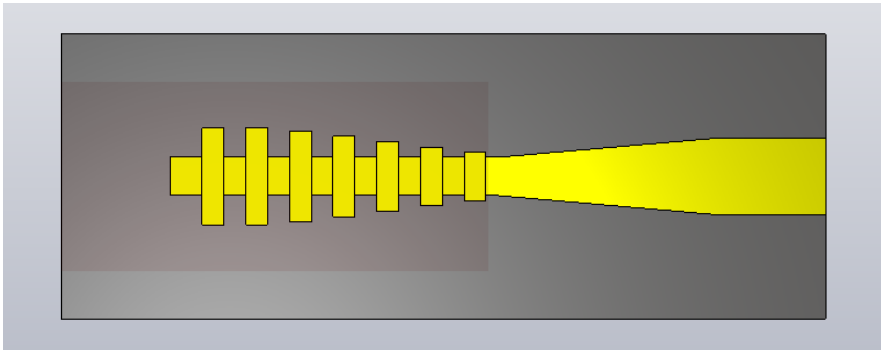

Figure 5.2.6.: Tuning section with Bragg reflector stripes on top.

A suitable solution is a 2 µm thin silicon membrane with lithographically created gold stripes. The inherent flexibility of the silicon allows bringing the membrane into contact with the laser without causing damage since the maximum surface pressure is limited by the membrane's elastic force. The membrane is fixed at its far end to a 3D positioning system based on piezo slip-stick stages that provide nanometer-resolution movement capability. The membrane initially points downwards at an angle of approximately 30° and begins to increasingly bend after the tip touches down on the device during

adjustment of the z-axis until the entire area with reflector stripes lies flat on the tuning section.

With the membrane also positioned correctly laterally, tuning is now possible by moving it along the x-axis to change the cavity length. The phase of the reflected wave has to be modulated by 2π to scan a full FSR, which is achieved with a membrane movement of a half-wavelength (ca. 54 µm), see figure 5.2.8.

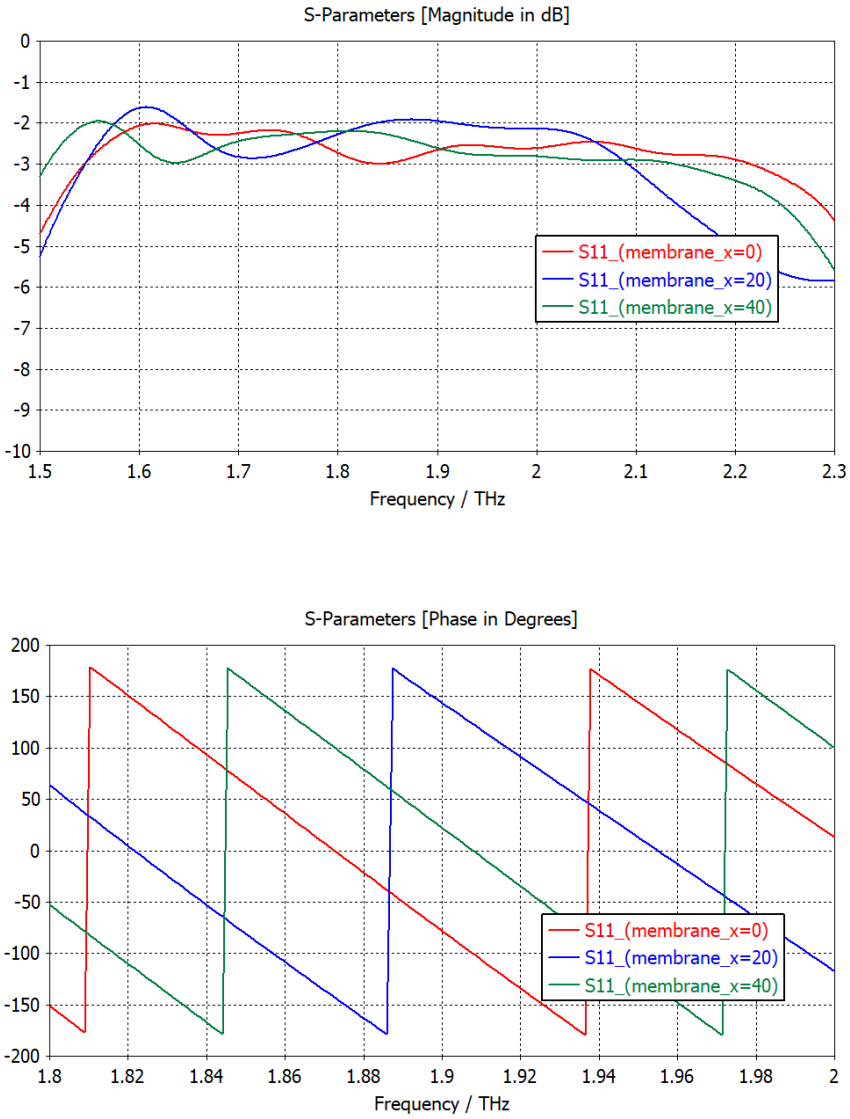

Figure 5.2.7.: Top: S11 of the tuning section with membrane reflector is between -2 dB and -3 dB in the relevant band from 1.8 THz to 2.0 THz. Longitudinal movement of the reflector ($membrane_x$, given in micrometers) modulates the frequency response to some degree.**Bottom:** The phase of the reflected wave illustrates the change in effective cavity length.

The precision of the membrane placement is not limited by the positioning stage itself but rather by the resolution of the microscope used to observe the device through a clear

window in the cryostat while controlling the movements. The process has to be done at an operating temperature of around 50 K after cooldown and thermalization of the parts to avoid thermal expansion-induced misalignments. This requires a microscope with a small numerical aperture to bridge the distance of around 10 cm between QCL and lens, limiting the resolving power to several micrometers. From the conceptual point of the system, this is not a prohibitive condition as successive realignment while observing the tuning performance is possible to find the correct membrane position. More concerning is the possibility of surface flatness imperfections that are unavoidable in the manufacturing process or dust particles that could pollute the surface in a non-cleanroom environment. If the membrane cannot come close enough to the microstrip of the tuning section, this offset in the z-direction could cause the reflectivity to deteriorate below acceptable values. Luckily, this seems not to be the case for offsets smaller than ca. 4 µm (see Fig. 5.2.9).

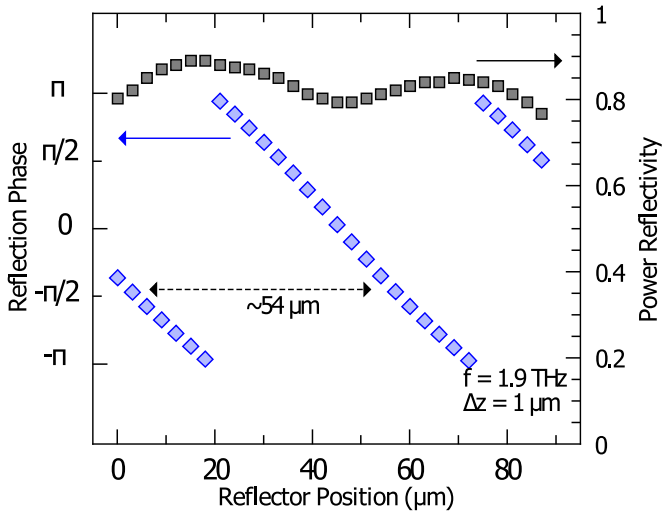

Figure 5.2.8.: Simulated phase of the reflected wave at 1.9 THz as a function of reflector position. A movement of 54 µm scans a full FSR of the resonator. Some modulation of the reflectivity is also seen.

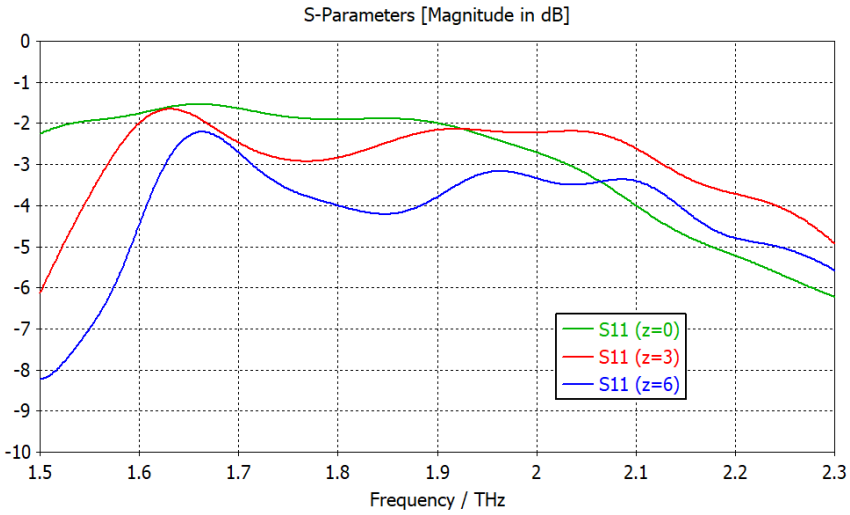

Figure 5.2.9.: An offset of the membrane reflector in the z-direction creates a gap between tuning section and reflector which deteriorates the reflectivity for values larger than ca. 4 µm. If not specified otherwise, a z-direction offset of 1 µm is assumed in the simulations to account for surface roughness.

5.2.4. Front Reflector and Antenna

The devices adopt the 3x3 patch antenna array described in [117]. This antenna type is capable of generating a near-Gaussian beam with high radiative efficiency and has been proven to work as expected at 1.9 THz THz and 4.7 THz so far. It consists of 3 parallel rows of 3 elliptical antenna patches each, fed in series. Similar to the tuning mechanism, the realization of this antenna becomes possible only through the BCB planarization. Radiative efficiencies would be fundamentally lower on a high-ε_r GaAs substrate.

The high efficiency and low inherent reflection from the antenna requires some care in the design of the front reflector to find a balance between resonator q-factor and optical power output. A low q-factor leads to increased threshold current or could prevent oscillation altogether, while a high q-factor gives more weight to intracavity losses, reducing the laser efficiency. A simple facet formed by a GaAs-BCB interface results in a reflectivity of only about 20 percent (power), a relatively low number, and leaves room for improvement to enhance the cavity q-factor. A simple way to achieve this is a BCB-filled gap followed by another block of GaAs. By varying both the gap and the block length the reflectivity can be tuned from 40 to 70 percent. Additionally, the frequency dependency can be chosen in a way such that the response is flat within the considered band. Overall the facet reflectivity must be high enough to prevent the residual antenna reflection from interfering with the resonator.

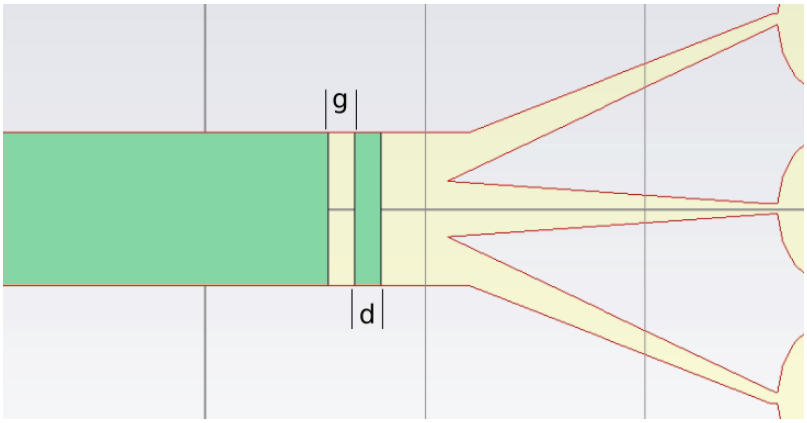

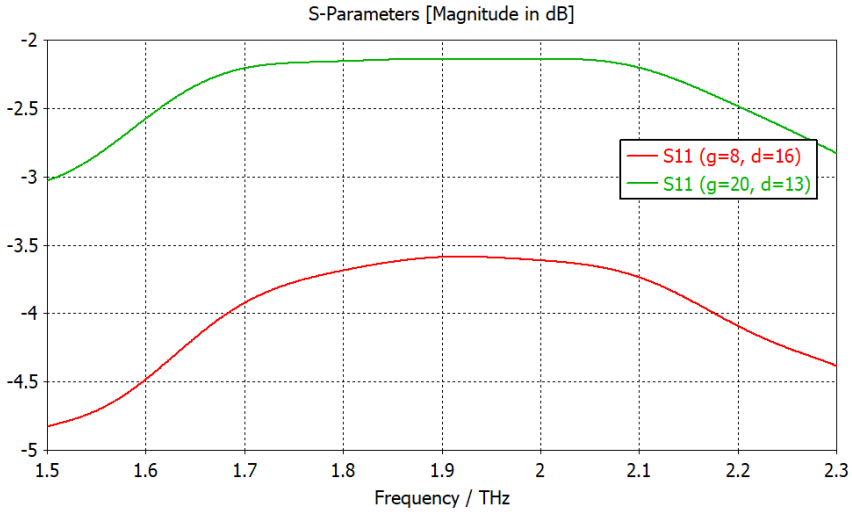

Figure 5.2.10.: The reflectivity of the front reflector can be adjusted from ca. 40 to 60 percent by varying the length of the GaAs block (d) and the size of the gap (g) while simultaneously creating a flat response in the operating frequency range.

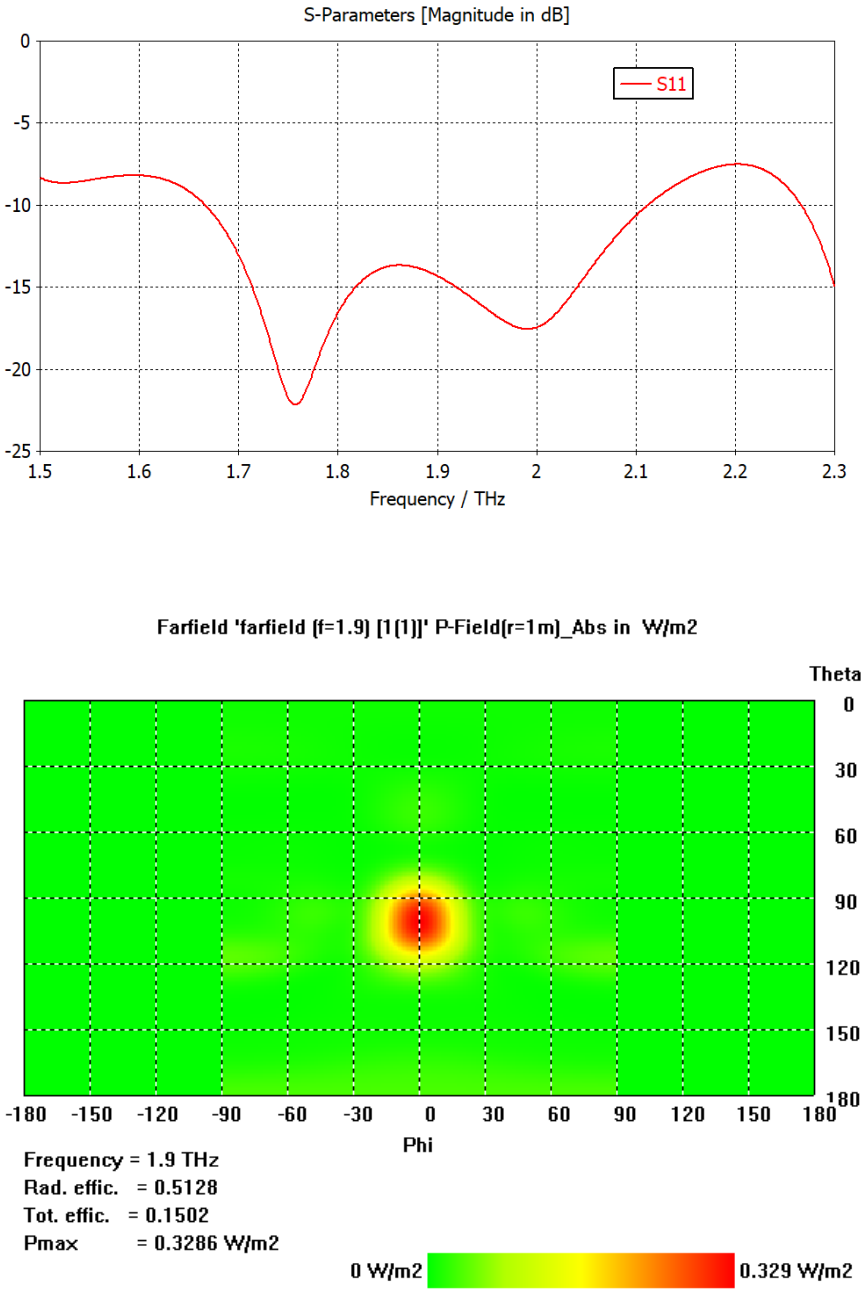

Figure 5.2.11.: Top: Antenna reflection in the relevant frequency band from 1.8 THz to 2.0 THz is lower than -13 dB. **Bottom:** Far field plot of the antenna beam shows an almost Gaussian, low-divergence beam profile (efficiencies are calculated including front reflector).

5.3. Measurement Setup

Evaluation of the device performance and comparison to data from the simulations requires a measurement setup that provides a cryogenic environment and the capability to record data on frequency, output power and beam shape while allowing visual inspection of the tuner position through a transparent window with a microscope.

Cryostat

Most measurements are made using a small closed-cycle cryostat (see Fig. 5.3.1) built in-house that is capable of approximately 45 K minimum temperature under the QCL's heat load, which is low enough to enable QCL operation with good output power. Advantages over a helium pulse tube cryostat include a rapid cooldown of less than one hour and excellent visual and mechanical accessibility to the QCL and the reflector membrane positioning system. The cooling machine is a Sunpower CryoTel™GT Stirling-type refrigerator with a 50 Hz piston cycle. The cooling machine is mounted with a flexible suspension to decouple from the rest of the structure and mitigate vibrations that could have a detrimental impact on the stability of the tuning mechanism. In addition, the vibrational amplitude of the cooling machine is reduced with adaptive electronics that generate a 50 Hz signal 180° out of phase with the vibration and drives an actuator. The circuit constantly measures the amplitude of the vibration and adjusts the coefficients of the generated sine and several of its harmonics until the error signal is minimized. The system is identical to the one deployed in the KOSMA 4.7 THz local oscillator for upGREAT.

The cold plate is connected with thermally isolating fiberglass structures to the vibrationally decoupled part of the cryostat. Flexible copper braids serve as a thermal connection to the cold tip of the cryocooler. The piezo stage is mounted directly to the cold plate to minimize unintended reflector membrane movements relative to the QCL. An elliptical mirror collimates and deflects the high-divergence antenna beam at an angle of 90°. A detailed view of the cold plate is given in Fig. 5.3.2. The QCL copper carrier is pressed down on the cold plate with two fiberglass clamps that each provide an electrical connection to one of the QCLs through their copper-plated underside (see Fig. 5.3.3).

A subset of measurements is carried out at liquid helium temperature to quantify temperature effects on the spectral gain. For this, a cryostat built for a Sumitomo RP-082B pulse tube cooler is used.

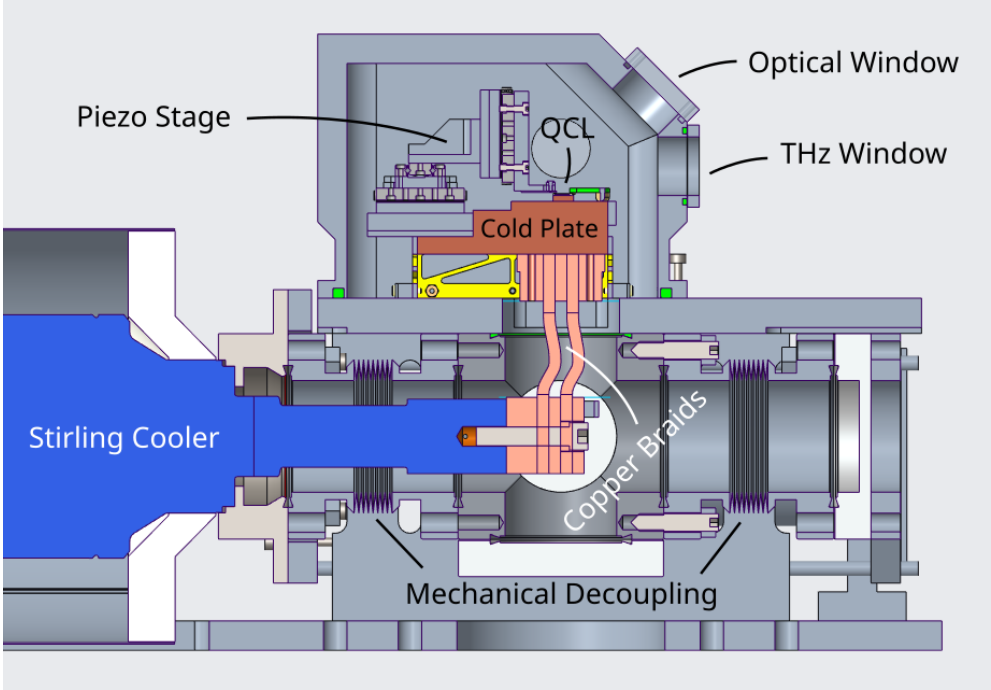

Figure 5.3.1.: Sectional view of the test cryostat. The cold tip of the Stirling cooler (in blue) is decoupled from the rest of the mechanical assembly to isolate the sensitive tuning mechanism from the 50 Hz vibrations caused by the moving helium compressor piston. Thermal connection to the cold plate is achieved with flexible copper braids from the cooling machine cold finger to the cold plate (brown).

THz Detector

The measurements of relative power and beam profile, as well as the recording of interferograms with a Fourier-transform spectrometer are carried out using pyroelectric detectors (Infratech LIE-301, LME-301, LME-353) as they offer sufficient sensitivity for our applications while being robust and compact. The detection mechanism utilizes the natural occurrence of electrical polarization in certain crystals, lithium-tantalate in this case, which changes under temperature variation. The wavelength dependence of this bolometric mechanism is only determined by the absorption efficiency and consequently heating of the LiTaO3 crystal, which is typically highly broadband. The charge across the crystal decays with a device-specific time constant through leakage currents and amplifier input current, which means only changes in illumination are detected and optical chopping of the QCL either mechanically or electrically is necessary. Together with a lock-in amplifier (Stanford Research Systems SR810) this allows the detection of optical powers smaller than 1 µW at 20 Hz chopping frequency and 100 ms integration time. To minimize noise, electric and magnetic shielding of the high-gain stage (typical transimpedance amplifier feedback resistance of 10 GΩ to 100 GΩ) is necessary, as well as protection of the circuitry from air currents.

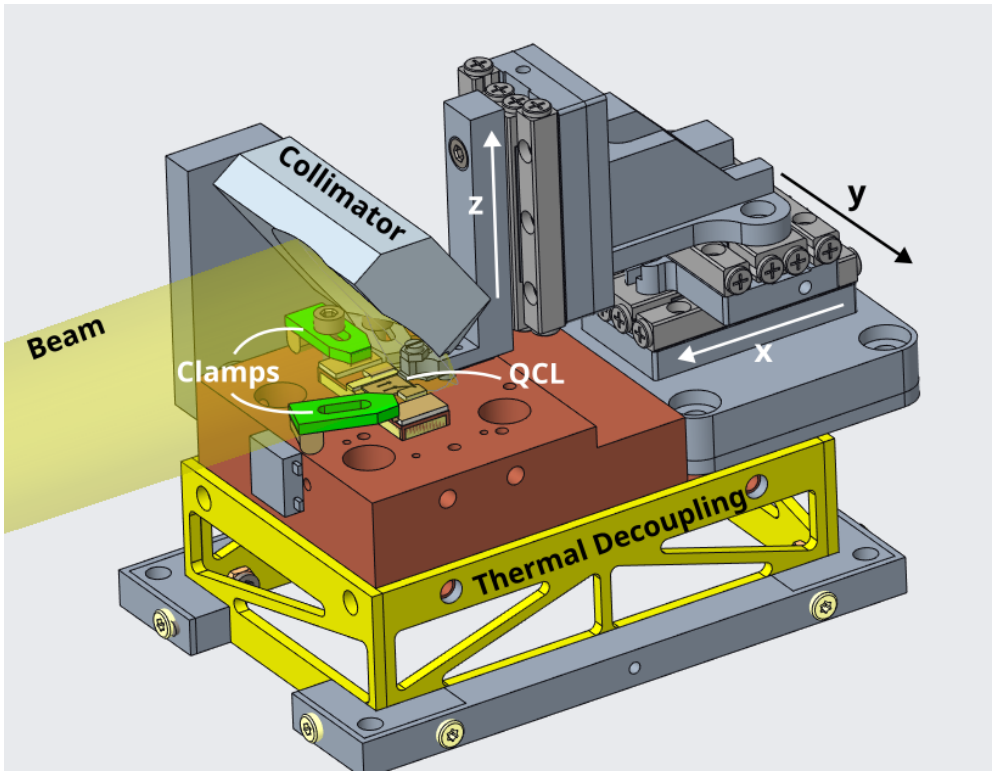

Figure 5.3.2.: View of the cold plate assembly with QCL, collimating mirror and translational stage.

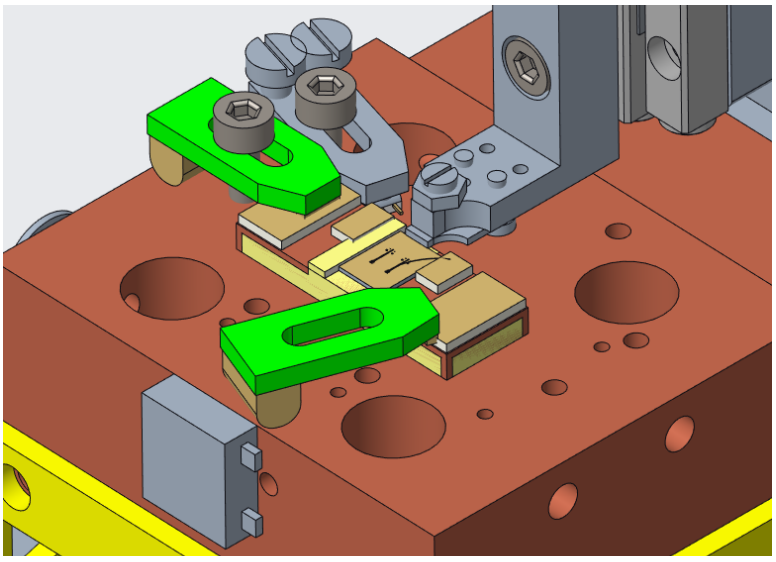

Figure 5.3.3.: Detail of the QCL mounting on the cold plate and the membrane positioning system on the right. Shown in green are the copper-plated fiberglass clamps that serve as a positive electrical contact for the two QCLs and simultaneously provide the physical force to create a good thermal contact with the coldplate

Fourier Transform Spectrometer

Fourier transform spectrometry is a simple and effective way to determine the spectrum of a quantum cascade laser. The collimated, powerful beam is usually easily aligned with the spectrometer's optical axis. The interferogram recorded with a retardation of 30 cm typically yields a resolution of ca. 1 GHz after transforming to frequency space, enough to determine the tuning performance. In addition, the optical power can also be extracted from the interferogram, although two frequency-dependent factors impact the power measurement during tuning: the beam angle from the patch antenna changes with frequency by $0.064\,^\circ\,\mathrm{GHz}^{-1}$[117] and absorption in air varies due to atmospheric water lines. The long THz wavelengths allow a much simpler construction of the spectrometer's moving parts compared to typical FTIRs used in the mid-IR. The moving mirror is mounted on a linear slide driven by a leadscrew with a stepper motor. Most measurements a done with 99.2 µm step size, which leads to an upper-frequency cutoff at 3.02 THz.

Reflector Membrane Positioning

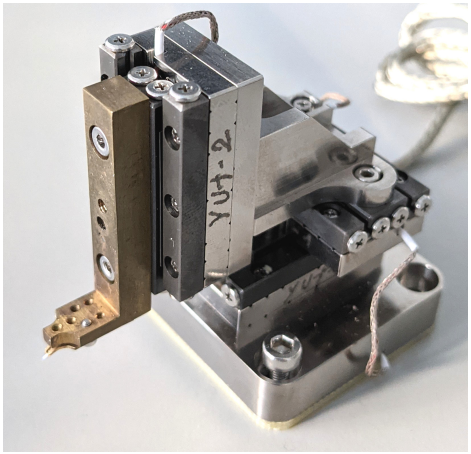

Figure 5.3.4.: 3-Axis piezo positioning stage with reflector membrane attachment.

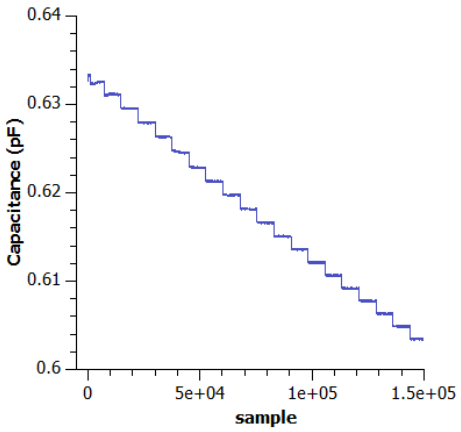

Figure 5.3.5.: Readout of the capacitive position sensor system. Each step corresponds to a movement of 5 µm.

The 3-axis control of the membrane position is implemented with a Smaract piezo system built from Smaract SLC1730 linear translational stages modified for cryogenic operation and a computer-interfaced piezo controller (model SCU3D). As with all piezo slip-stick systems the travel distance is not accurately defined by the number of steps and the input voltage waveform alone since temperature, friction and moved mass determine the exact step size. The steps between successive tuning positions are too small to be

resolved by the microscope, so to determine the membrane movement with sufficient accuracy, we calibrate the conversion of steps to distance before each measurement series by counting the steps necessary for a quantifiable distance, typically 300 µm, in the present environment. Additionally, we implemented a capacitive measurement system based on the Analog Devices AD7747. This 24-bit capacitance-to-digital converter can measure a capacitance of 17 pF with a resolution down to 10 aF and achieves a resolution of ca. 1 µm in our setup.

Chapter 6.

Experimental Results - 1st Generation Devices

6.1. Overview

For a total of ten QCLs from the first fabrication run extensive testing was conducted in this work to determine the performance of the real-world devices compared to the simulated model. All devices are based on the heterostructure "EV2118" grown by MBE at ETH Zürich and then processed into the finished lasers through lithography, etching, BCB planarization and metallization steps.

QCL	Chip	Ridge L	Front Reflector
1[1]	A	1.0 mm	50%
2[1]	A	1.0 mm	67%
3	0	1.0 mm	50%
4	0	1.0 mm	67%
5	1	1.0 mm	50%
6	1	1.0 mm	67%
7	2	1.5 mm	50%
8	2	1.5 mm	67%
9	3	1.5 mm	50%
10	3	1.5 mm	67%

Table 6.1.: List of all 1st generation QCLs discussed.

The ten QCLs are distributed pairwise to five chips, i.e. uninterrupted cuts of GaAs substrate containing two individual QCLs, each with independent anode contacting and common cathode. These chips are mounted on a 6mm x 18mm x 1.5mm copper block that can be clamped down on the cryostat coldplate and electrically contacted, see Fig. 5.3.3.

[1] taper and tuning section are cleaved off on this device for comparison purposes

The QCLs differ in the length of the ridge with 1.0 mm and 1.5 mm devices available (measured from the front reflector to the beginning of the taper section) and in the reflectivity of the front reflector where both 50% and 67% are implemented. This is done mainly to find the best parameters with regard to output power and to find the maximum ridge length that still provides a large enough free spectral range to prevent multimode oscillation. Additionally, we obtained two devices that do not feature a taper or tuning section since it was intentionally cleaved off before mounting the chips. The intention here is to have baseline data on the antenna and IVL characteristics without the uncertainty arising from inaccessible parameters such as membrane reflector coupling efficiency.

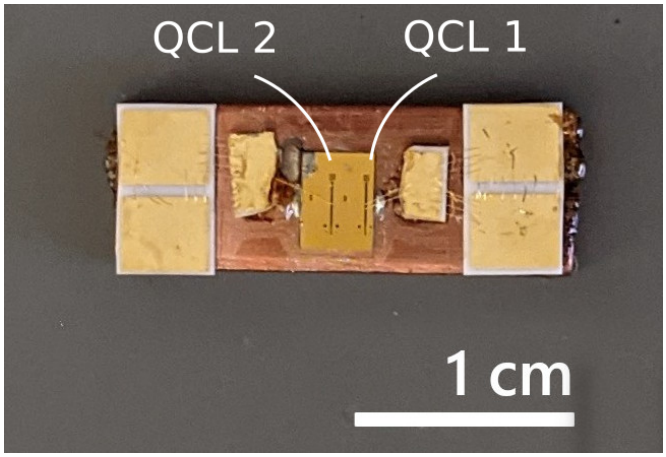

Figure 6.1.1.: One of the five first-generation QCL chips mounted on a copper block with electrical contact pads wire bonded to the devices.

The objective of the measurements performed in this chapter is to verify the general feasibility of the tuning mechanism in the fabricated QCLs.

First, some initial measurements are done where output power and spectrum are investigated without reflector membrane to establish a comparative baseline for the frequency, especially the laser threshold. Comparison to the cleaved devices on Chip A highlights the impact of the taper and tuning section and the influence of the different front reflector reflectivities (50% and 67%) can be observed isolated from these more complicated structures.

The fundamental and most crucial test with regard to the tuning capability is then the measurement of the output spectrum and its tunability by movement of the reflector membrane. It is equally as important to identify issues such as multimode operation or unwanted intra-cavity reflections and to investigate their origin. Next, measuring the

optical output power as a function of tuning configuration and bias current helps to further establish a stable parameter region and improves the overall understanding of the physical processes. Lastly, the measurement of beam profiles, including polarization data, helps to understand antenna characteristics and lets us determine if higher lateral modes are present in the laser ridge.

The spectra discussed in this chapter are recorded with the previously described Fourier spectrometer setup at a cold plate temperature of 46 K to 48 K depending on bias current. The QCL current is chopped at a frequency of 19 Hz by modulating the logic level interlock input of the current supply with the TTL output signal of the lock-in amplifier. Since electrical chopping could, in principle, have an impact on the spectrum, several comparative measurements with a standard mechanical chopping wheel and the QCL running continuously were carried out. No difference between electrical and optical chopping was found in the measured spectra.

6.2. Initial Measurements on the Cleaved Devices

The initial checks performed on the cleaved QCLs 1 and 2 verify that the devices generally work at a temperature of 48 K in the expected frequency range and produce a defined antenna beam in the correct polarization.

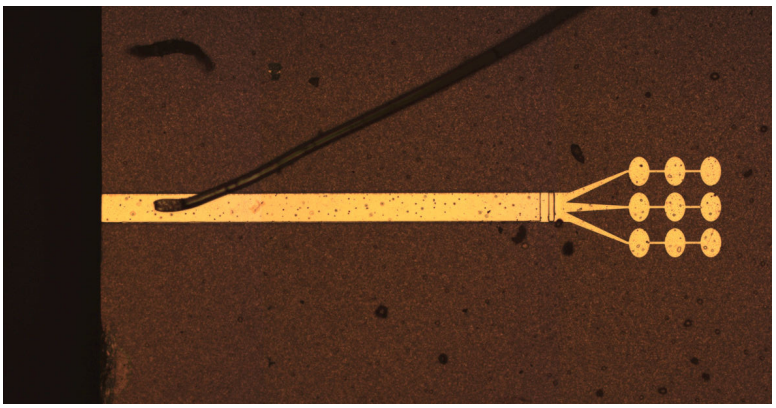

Figure 6.2.1.: QCL 1 and 2 are intended for baseline measurements without any influence from the more complicated tuning structures. The chip is cleaved off such that the transition and tuning section are removed.

Starting with the IVL-curves (Fig. 6.2.2) of the cleaved devices, we observe a laser threshold of 128 mA (183 A cm^{-2}) resp. 132 mA (189 A cm^{-2}) and a current dynamic range of more than 60 mA before laser action ceases accompanied by a large jump in differential resistance caused by electrical field domain formation[148]. Optical output power shows a distinct steplike nature in both QCLs, with a better slope efficiency and higher maximum power in QCL 1.

On examination of the spectra (Fig. 6.2.3 and 6.2.4) it becomes clear that these features are a direct consequence of longitudinal mode jumps resulting from gain profile shift and refractive index changes from bias current variation. Apparently, an optically weaker mode can prevail in conditions that would typically favor another mode with stronger modal gain until a threshold value is reached and oscillation on a different frequency starts. The spectra also reveal fundamental disparities in the two lasers that are not explained by the different front facet reflectivities. QCL 1 always operates on a single mode with a mode spacing of 72.8 GHz made visible through mode selection by current (superposed by a small contribution from current tuning of ca. 2 GHz). This is too high for successively indexed longitudinal modes given that a realistic value for the effective refractive index n_{eff} for GaAs/AlGaAs materials is around 3.6 [149]. Using a field solver to calculate the phase constant β for the laser resonator waveguide, one obtains $\beta = 1.39 \cdot 10^5$ at 1.9 THz. Neglecting the influence of intersubband transitions for now, this leads to a cavity FSR of 42.9 GHz as given by $\nu_{FSR} = c/2nL$, which indicates lasing on every second mode. Increasing the bias current shifts the gain spectrum to higher frequencies and induces a mode jump from 1.81 THz at 150 mA to 1.95 THz at 190 mA. The mode-selective mechanism is most likely attributable to parasitic reflections within the cavity or spatially non-uniform material gain, both resulting from manufacturing uncertainties. QCL 2 on the other hand exhibits multimode lasing at all currents without the suppression of specific frequencies observed for QCL 1. Mode spacing is 36.1 GHz on average, in approximate agreement with the value expected from the simplified waveguide considerations above and almost precisely half the mode spacing of QCL 1. Despite the multimode spectrum, the gain shift to higher frequencies with increasing bias current is again clearly visible.

Verifying the far field patterns against the simulation model confirms that the lasers operate on the expected fundamental waveguide mode. Deviations from a gaussian beam indicate possible discrepancies between the model and real-world devices. The far field radiation patterns are recorded with a single-pixel pyroelectric detector moved with an XY translation stage at a distance of 24 mm above the QCL with all collimating optics removed. Map resolution is determined by a 1 mm pinhole aperture in front of the detector. An alternative cryostat cover with a large HDPE window replaces the regular cover designed for tuning. Polarization data is obtained with lithographically etched polarizer grids in transmission. Tests at 1.9 THz indicate a polarizing efficiency of better than 95% for these filters. The fraction of the total power integrated over the beam in each polarization is indicative of the symmetry of the laser and its oscillating modes. The patch antenna is designed to radiate a near-Gaussian beam with a polarization vector parallel to the laser ridge. Still, the experimental data reveals a non-negligible

fraction of the total integrated power in the orthogonal polarization, contributing more than one third of the total power in some devices.

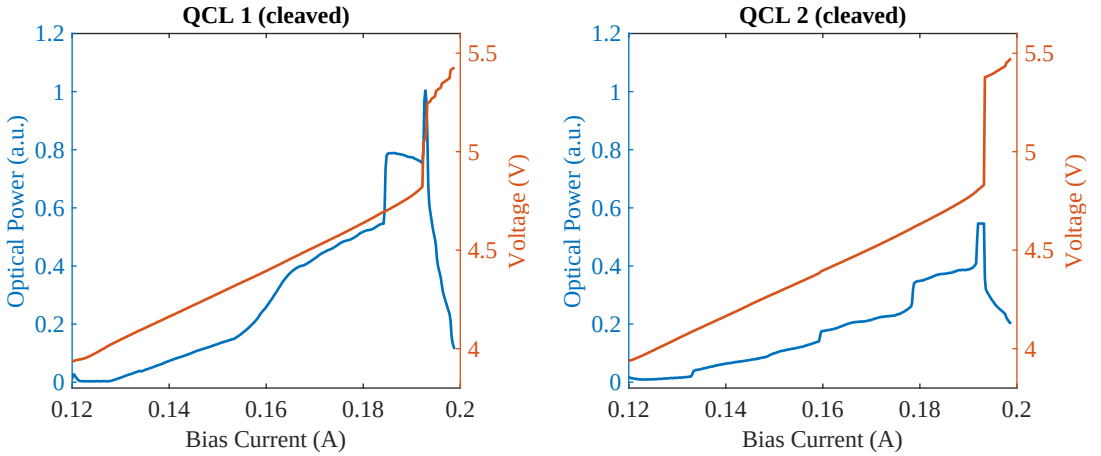

Figure 6.2.2.: Left: IVL characteristics of QCL 1 measured with a pyroelectric detector in an optically chopped setup. **Right:** IVL characteristics of QCL 2, measured in an identical setup. The nonidentical spectral features (see below) lead to differences in the optical power curves, whereas the IV characteristics depend on the heterostructure and are nearly identical.

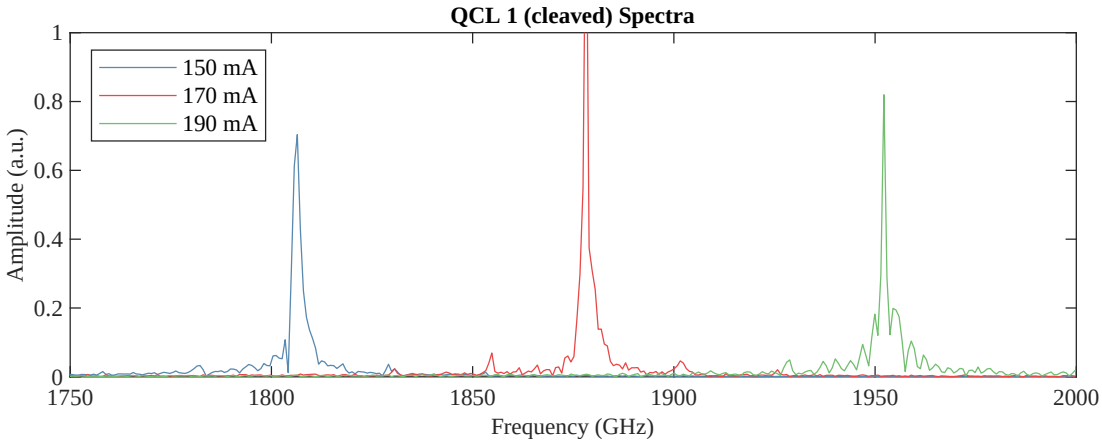

Figure 6.2.3.: QCL 1 spectra at different bias currents. Single-mode operation is always maintained. The mode spacing of 73 GHz is approximately twice the calculated cavity FSR due to skipped modes.

6.3. Baseline Characteristics without Reflector Membrane

At the time of this assessment, only Chip A and Chip 0 (see table 6.1) are readily mounted and bonded; therefore, the first tested tunable devices are QCL 3 and 4. With the general parameters and laser characteristics established from the measurements on the cleaved devices it is now possible to evaluate the effect that the additional transition

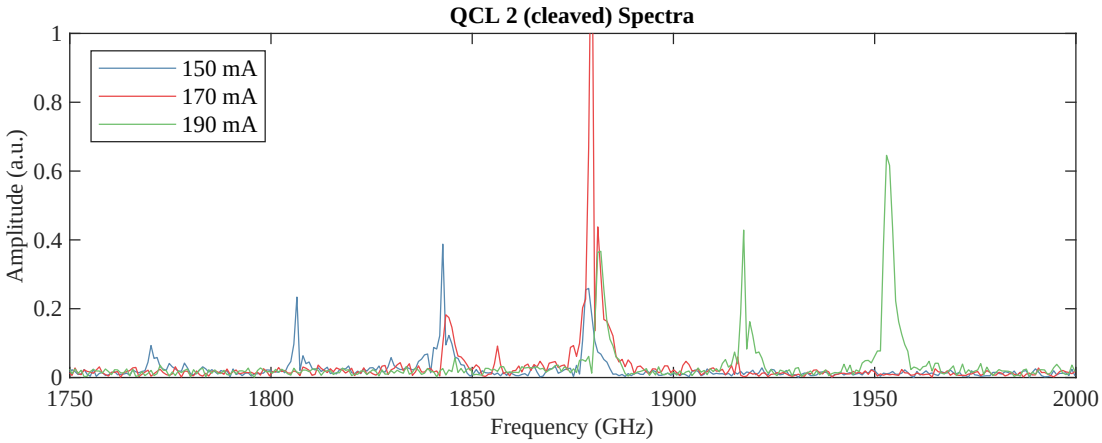

Figure 6.2.4.: QCL 2 spectra reveal multimode operation at all bias currents. Here no modes are skipped, and a mode spacing of 36.1 GHz on average appears.

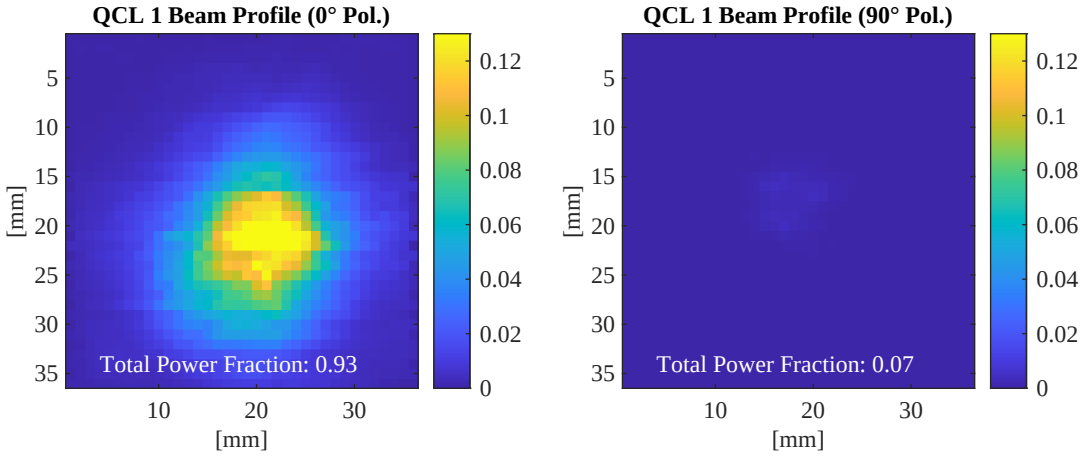

Figure 6.2.5.: Beam profile of QCL 1 in co- and cross-polarization. 93% of the power is found in the designed polarization of the antenna.

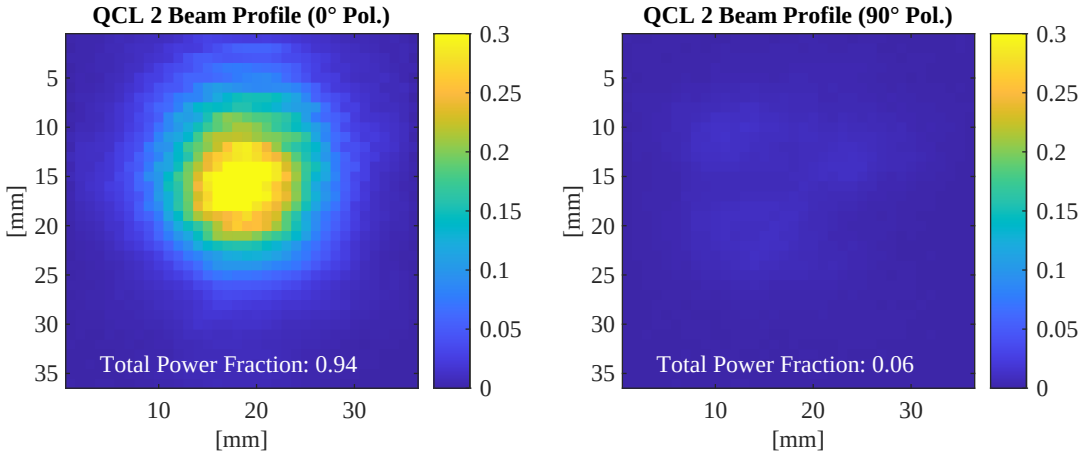

Figure 6.2.6.: Beam profile of QCL 2.

and tuning section has on the QCLs. Experiments on the bare chip without applied reflector membrane are carried out initially and compared to the results of the previous section. The setup is unchanged, and only the copper carrier with the chip is exchanged on the cold plate.

As a starting point, the IVL curves are again measured for both QCLs. Featuring a larger GaAs area due to the added material in the transition section, the operating current is expected to be 10% higher for these devices compared to the cleaved ones to provide the same current density. Since the cavity Q-factors are not well known, no detailed information can be taken from the comparison of threshold current and slope efficiency. However, qualitatively worse performance can be predicted for lasers running without reflector due to high losses at the open tuning section. Far field simulations predict radiative losses of ca. 50% of all power transferred to the tuning section microstrip, whereas dielectric losses in the BCB are negligible according to available material data.

The measured IVL curves generally confirm this, even though they appear dramatically different for the two lasers. While the substantial losses lead to a narrow current dynamic range from 208 mA to 215 mA on QCL 3 together with low optical power, this is much less pronounced for QCL 4, which, while performing still significantly worse than the cleaved devices here, suffers much less from additional losses. Inspection of the spectra allows more insight into the cause of this discrepancy.

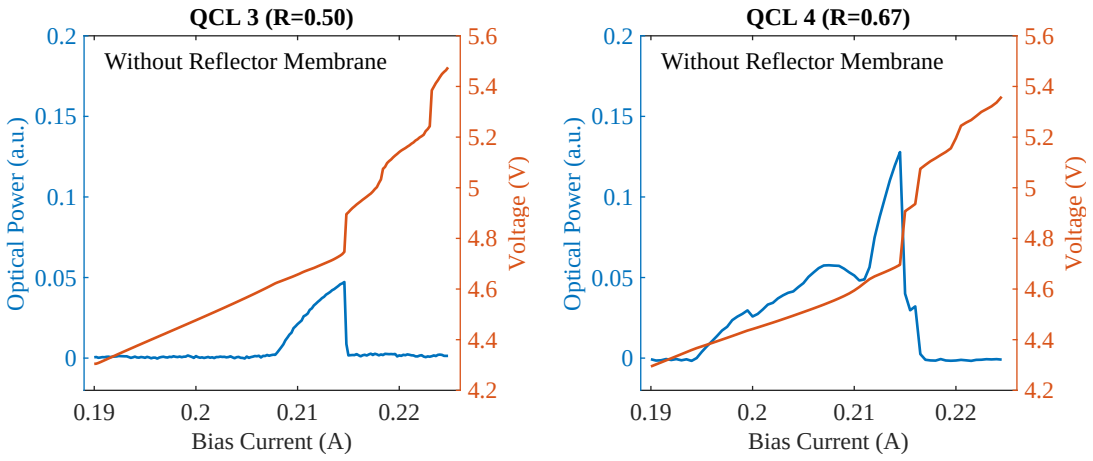

Figure 6.3.1.: Left: IVL curve of QCL 3 measured without the reflector membrane. The current dynamic range is restricted to a narrow range between 208 mA and 215 mA caused by high losses. **Right:** IVL curve of QCL 4 without reflector, here the larger current dynamic range and output power indicate lower losses compared to QCL 3.

The spectra shown in Fig. 6.3.2 and 6.3.3 further demonstrate that significant variation in key parameters is present. QCL 3 favors a single mode at around 1.99 THz.

A mode spacing of 49.5 GHz can only be determined at the lowest current setting, as the emission is otherwise single mode. No further mode jump can be induced through gain profile shifting due to the small current dynamic range from 208 mA to 215 mA. One mode is certainly skipped here, similar to QCL 1. In contrast, QCL 4 is much more prone to multimode oscillation throughout all currents. Such a difference in preferred mode regime was already observed in the cleaved devices and can again be explained by unintentional frequency selective elements arising from manufacturing uncertainties. A mode spacing of 30.1 GHz can be determined from the multimode spectra in Fig. 6.3.3 for QCL 4 without reflector membrane. Comparing this to the model is not as straightforward as for QCL 1 and 2 before since the phase constant β is not uniform throughout the waveguide. A way must be found to determine cavity FSR from the CST simulations. Since the Eigenmode solver included in the software package places too restrictive conditions on the model, the most straightforward way is to excite the structure through the front facet and find the frequencies with maximum intracavity field density and, resulting from that, maximized losses seen as a dip in the S11 parameter. For such an approach, we find that the FSR is 30.3 GHz assuming a phase refractive index $n_{p,eff} = 3.6$ at 1.9 THz[149] for GaAs-AlGaAs heterostructures, which is surprisingly close to the measured value for QCL 4, but significantly more than seen in QCL 3.

The problem that arises at this point is the previously neglected frequency dispersion of the refractive index of the gain material, from which a group refractive index $n_{g,eff} = n(\nu) + \partial n(\nu)/\partial\nu$ is derived, which is always higher than the phase refractive index. This distinction is essential for calculating the cavity FSR, which depends on $n_{g,eff}$ if dispersion is taken into account. The dispersion of a QCL is composed of a static part from the semiconductor material and waveguide and a dynamic part that originates from intersubband gain since the frequency dependence of the (phase) refractive index is linked to the gain profile through Kramers-Kronig relations[132] and typically measured with time-resolved transmission spectroscopy of the laser resonator above threshold[150]. This dependence creates a maximum of $n_{g,eff}$ that can be substantially higher than $n_{p,eff}$ in the vicinity of the peak of the gain profile. Going back to the measurements made for QCLs 1 and 2, it was already observed that the mode spacing was ca. 15% lower than calculated from the waveguide model alone, and the $n_{g,eff}$ experimentally determined by $\nu_{FSR} = c/2nL$ is 4.13 for these devices. There is no reason to believe that this gain-induced effect should be much different for the tunable lasers, therefore the missing correction for QCL 4 is inconsistent. The most likely explanation is a shorter than expected resonator length, as would be the case for a strong reflection from the transition section that dominates the lasing process. Of course, that would entail a

disruption of the tuning principle for this laser.

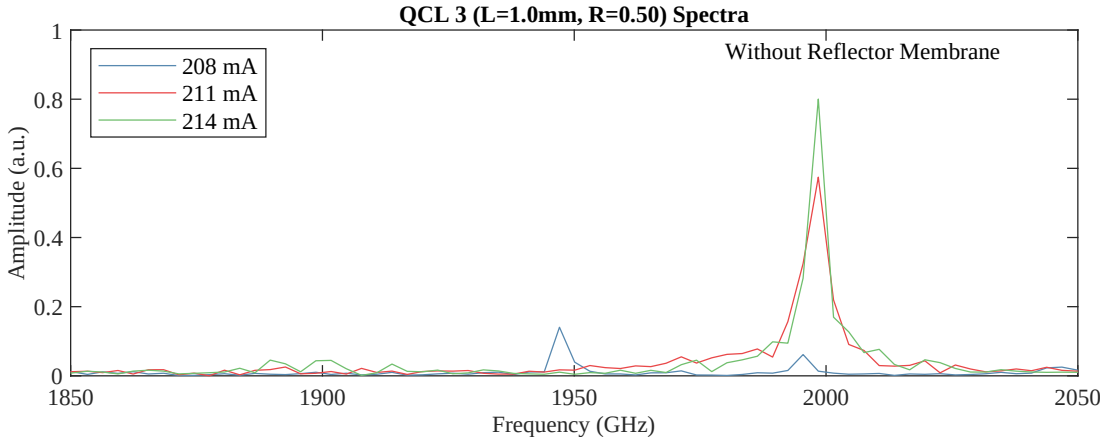

Figure 6.3.2.: Spectra of QCL 3 without reflector at different currents within the lasing current range for this configuration. The device emits at a single mode around 1.99 GHz except for the lowest current setting, revealing a second mode 49.5 GHz lower in frequency.

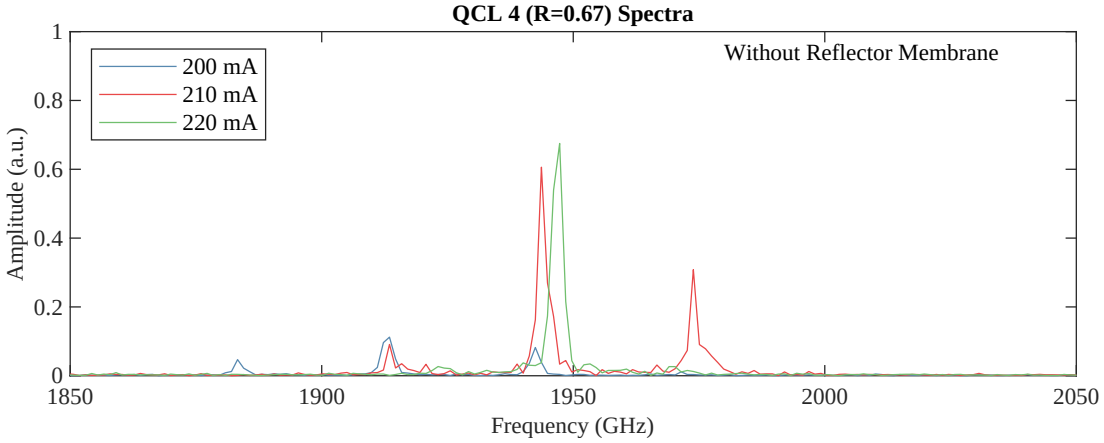

Figure 6.3.3.: Multimode emission is observed in the QCL 4 spectra without reflector.

6.4. Baseline Characteristics with Reflector Membrane

The next step is to investigate the effect the reflector membrane has on the laser parameters. The model predicts a lower threshold current, a higher slope efficiency and increased maximum optical power are expected as a result of the much lower radiative losses from the microstrip. For these measurements, the reflector is fixed with the piezo stage at a position centered at the zero position, with the first reflector strip directly at the end of the transition from laser ridge to microstrip (see Fig. 6.4.1).

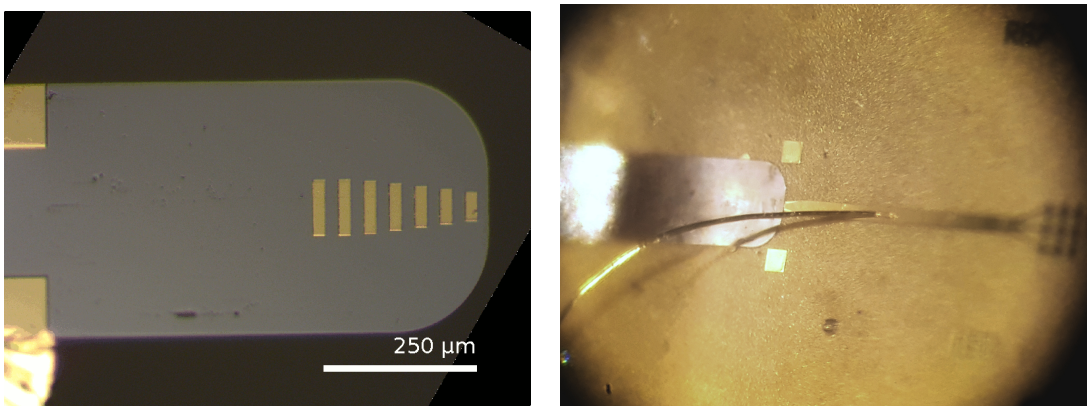

Figure 6.4.1.: Left: Bottom side of a reflector membrane. **Right:** Microscope image of QCL 3 with the reflector membrane applied viewed through the cryostat optical window.

As expected, the IVL curve of QCL 3 changes significantly with the reflector and shows a sixfold increase in peak optical power. At the same time, the current dynamic range now spans the range from 199 mA to 223 mA with a lower threshold and higher maximum current before field domain formation, resulting from the improved Q-factor and consequently the more robust photon-driven transport.

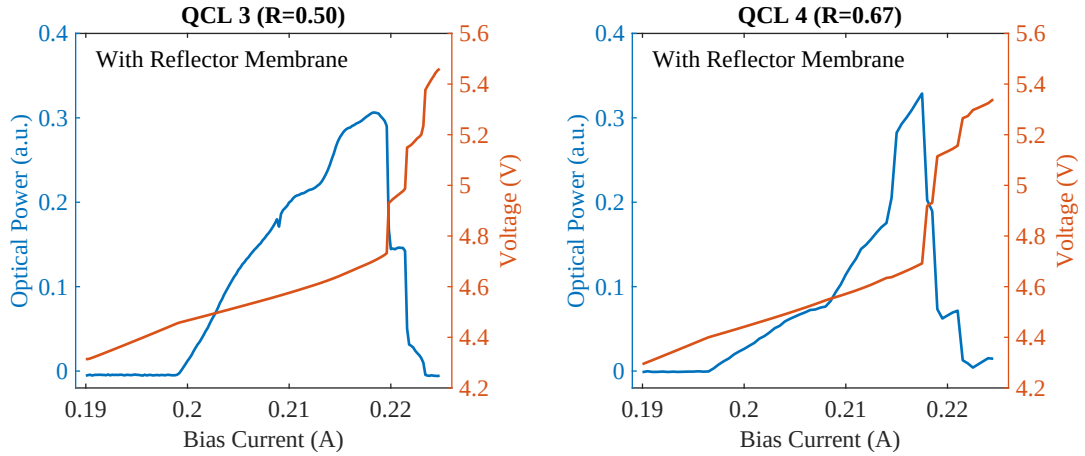

Figure 6.4.2.: Both QCL 3 and QCL 4 have their optical power increased significantly through the application of the reflector membrane.

At the same time, the recorded spectrum indicates that the resonant cavity length has changed as well, with the laser now operating between 1.956 THz and 1.963 THz with a more pronounced current tuning compared to the reflector-less operation. Without the reflector, this frequency range lies outside any observed mode. Since multimode regime is inaccessible with any current, no statement can be made regarding the FSR.

QCL 4 does not show an equally strong response to the reflector, although this device

also shows an improvement with a doubling of the optical power and the maximum current increased to 222 mA. The spectrum also reveals the impact of the reflector, the formerly multimode spectrum has changed to single-mode at all bias currents. The frequency of this mode, contrary to QCL 3, is unchanged within the usual variation from the highest lasing mode seen before at 1.977 THz without reflector. This indicates a bad coupling of the reflector to the tuning section so that the laser mode is not confined between front facet and membrane reflector. The loosely coupled reflector then produces the observed mode-selective properties. It is not easy to identify the cause of this with certainty, and at this point analysis is possible only tentatively.

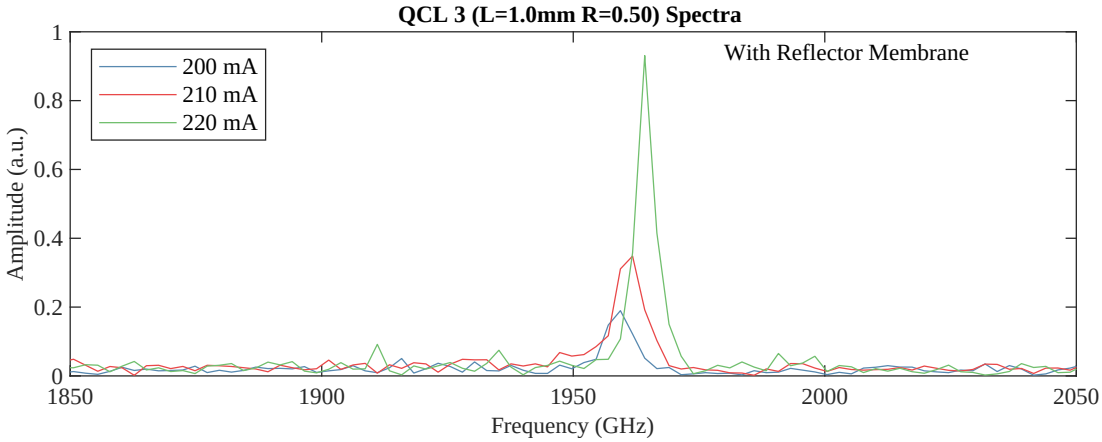

Figure 6.4.3.: Application of the reflector membrane has a profound effect on the spectrum of QCL 3. The frequency of the single mode has shifted from1.97 THz to ca 1.96 THz. A significantly larger current range is now accessible.

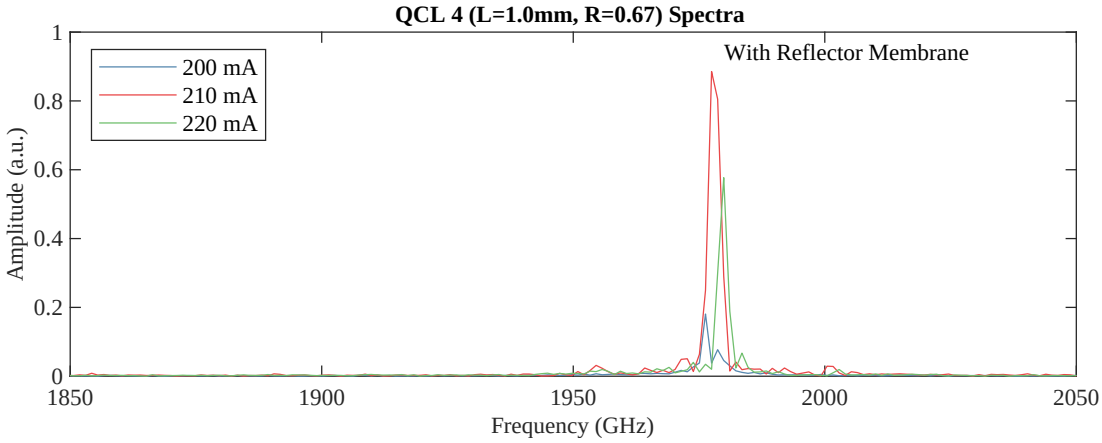

Figure 6.4.4.: The spectra of QCL 4 change from multimode to single mode operation with the reflector.

6.5. Continuous Tuning with Membrane Reflector

The results presented in this section are obtained similarly to the last one, except that now the reflector is now moved along the tuning microstrip section and the response of the laser to this tuning input is observed. The direction of movement is towards the far end of the strip to protect the laser, especially the bond wire, from accidental contact with the moving parts.

At the time of the experiments, the reflector position was calculated from a calibration movement performed before and after the measurement series since no absolute position sensor was available. The travel distance of the reflector per actuator step depends primarily on the piezo ceramic temperature; it is therefore incessant to wait for thermal equilibrium after cryostat cooldown to avoid drifts in the calculation of the position. The calibration is done by positioning the silicon membrane at the start of the tuning strip. This is observed visually through a microscope with an upper limit of the error not larger than 10 µm. The membrane is then moved to the far end of the microstrip, 300 µm away, and the total number of steps is counted. The number of piezo steps, amplitude and frequency used for each advancement is identical to the measurement series to account for inertia effects. Typically the individual positions are spaced by 5 to 20 piezo steps.

The most basic experiment to verify the general feasibility of the tuning mechanism is to set a reasonable bias current in accordance with the previously taken IVL curve and then successively record laser spectra and move the reflector. This approach yields great results for QCL 3, as shown in Fig. 6.5.1, where tuning over a span of ca. 22 GHz is observed in this configuration at 212 mA current. An almost linear relationship between membrane position and frequency is found here.

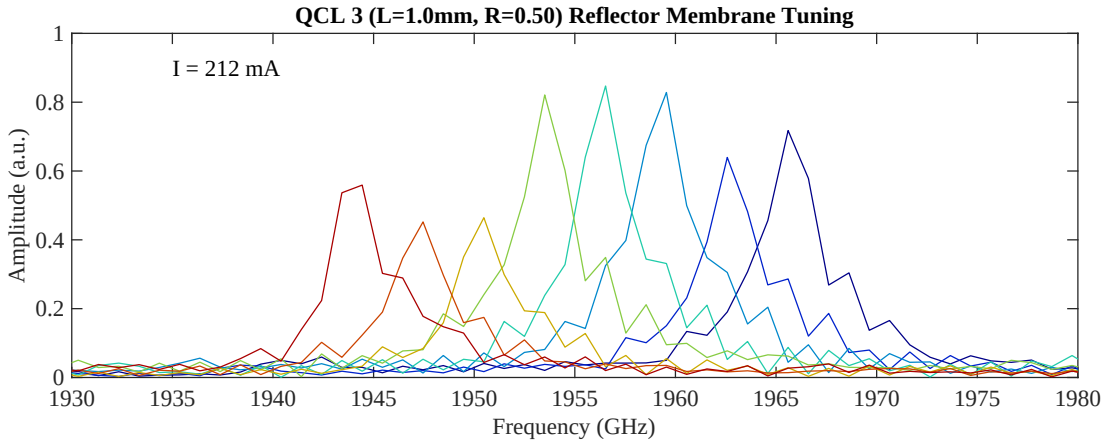

Figure 6.5.1.: Spectra of QCL 3 for different reflector membrane positions with a total travel range of 49 µm. A tuning range of 22 GHz is demonstrated in this measurement

The subsequent measurement includes a more extensive reflector movement range and is visualized in Fig. 6.5.2 as a frequency plot. The emission frequency is automatically determined from the spectra using Matlab. Here the reflector position dependency of the frequency, as well as the mode jump, is more clearly visible than in the spectral picture. This mode jump is a consequence of the shape of the total cavity gain, which must have a maximum within the tuning range and causes the frequency to jump whenever the next resonant cavity mode achieves a higher modal gain than the currently oscillating one that is being "pulled away" from the maximum gain region as the reflector membrane moves. From the plot we can determine a frequency jump of 24 GHz.

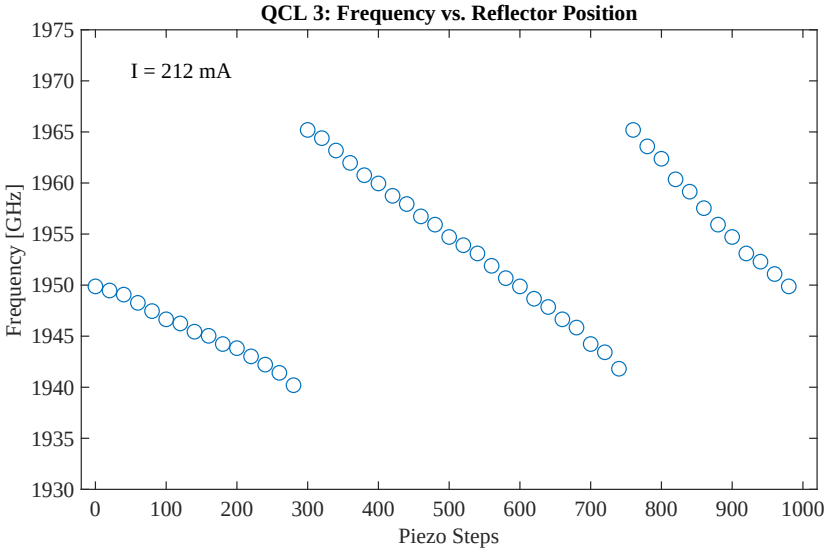

Figure 6.5.2.: Peak emission frequency of QCL 3 for a measurement series at 212 mA. The reflector membrane is moved backward 20 steps of the slip-stick piezo actuator between each FTS run. A range of 24 GHz is accessible to continuous tuning. Two mode rollovers are observed at 300 and 800 steps when the frequency is pulled away far enough from the maximum total gain frequency to favor the next follow-up mode.

A complete characterization of the accessible frequency tuning range has to include also the full span of the current dynamic range. For this purpose, the next dataset is obtained starting again at the same initial reflector position as before, but now spectra for a total of seven currents from 200 mA to 220 mA are processed before the next reflector position is set. A program written in C++ using the Qt 5 framework is responsible for operating the current source, piezo stage and FTS in synchronization and saves the recorded interferograms to a computer together with the associated parameters. The peak frequency of the resulting 516 individual spectra is plotted in Fig. 6.5.3 for all currents and reflector positions, as long as an emission peak is identified.

The central conclusion here is that the underlying tuning behavior can be found in the data for all bias currents, i.e. frequency monotonically decreasing as the reflector is

moved backward until a mode rollover occurs and the frequency rebounds. The observed shift in the reflector position at which the mode rollover takes place is in agreement with the previously seen Stark shift of the gain maximum towards higher frequencies at higher currents: As the approximately equally spaced cavity modes are moving towards lower frequencies with increasing cavity length the frequency rebound will occur first for currents which blue shift the gain.

A novelty noticed in this measurement is the mode jump to ca. 1.99 THz at currents of 216 mA and above for some reflector positions. While the blue shift of the gain is normal and the resulting frequency jump is expected, some data points reveal a reversal of the tuning direction in this region, indicating that less explicable effects can become dominant under certain conditions. In addition, it should be noted, that the frequency selective feature causing a mode skip in the spectra without membrane (see Fig. 6.3.2) prevents lasing in the range from 1.97 THz to 1.99 THz also with the added reflector.

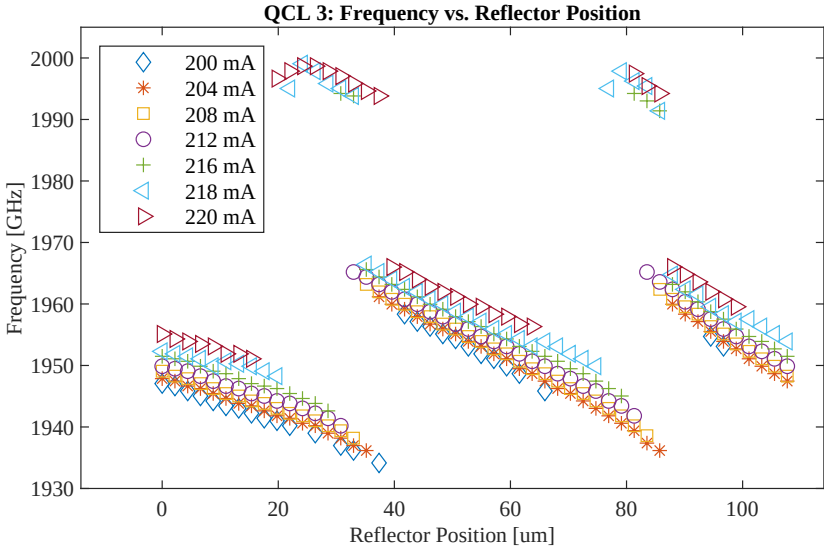

Figure 6.5.3.: Measurement series identical to Fig. 6.5.2 but for a set of bias currents within the current dynamic range. At 218 mA and 220 mA another mode higher in frequency is tunable with some reflector positions. At some points in the parameter space, especially on the low and high ends of the current range, the optical power is either too low to appear in this chart or lasing ceases completely.

The same periodicity of the frequency is found again in the optical power output (Fig. 6.5.4). For currents smaller than 216 mA, the power is maximal at frequencies well within the tuning range. It decreases at the edges close to the mode rollover, consistent with previous assumptions of a frequency-selective total cavity gain. Above 216 mA this periodicity is not observed. Instead, rather unsystematic fluctuations are found under these conditions where some of the power changes coincide with the previously shown mode jumps while others do not.

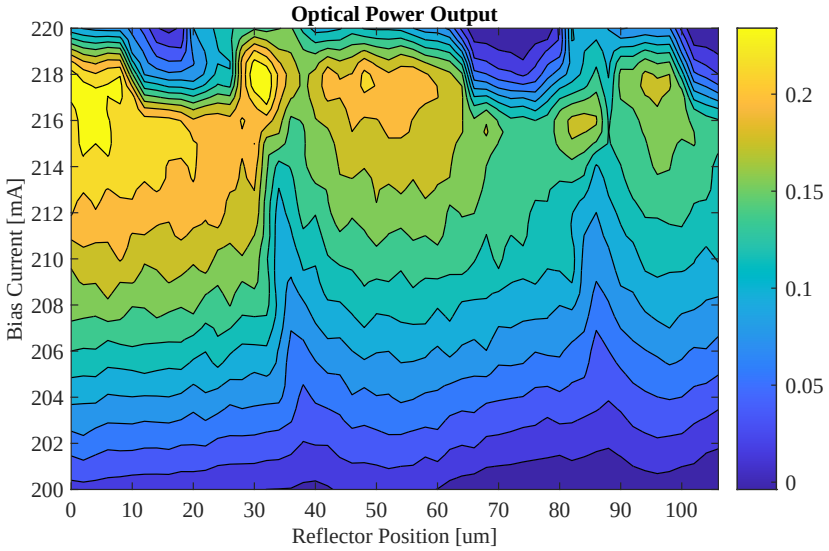

Figure 6.5.4.: Optical output power of QCL 3 as measured with a pyroelectric detector for the same bias currents and reflector positions as in Fig.6.5.3. The periodicity in frequency emerges similarly in the output power.

The tuning characteristics of QCL 4 deviate significantly from QCL 3. The previous investigation of the effect of the reflector membrane on the IVL curves suggested reduced effectiveness in QCL 4 and the suspiciously high FSR without reflector added to this suspicion. The findings for the tunability support the earlier hypothesis of strong transition section reflections, in fact, a continuous tuning range of only 4 GHz before a mode jump occurs is discovered (see Fig. 6.5.5). Additionally, the required reflector movement distance to go through this range is much larger than expected and does not correspond to an equivalent change in cavity length. The mode jumps induced by the reflector movement show a mode spacing of either 29 GHz or 60 GHz where a skipped mode can be assumed. Possibly both the reflector coupling is insufficient and the parasitic reflections create a coupled-cavity system. The approximately same frequencies are found in the multimode emission of the earlier measurement on this laser without any membrane at 200 mA and 210 mA, see Fig. 6.3.3 which further promotes the assumption of a dominant resonance between the front facet and transition section.

It is not completely clear what exactly happens on a microscopic level to cause all of the observed phenomena in QCL 4. A bad reflector coupling alone can explain the weak tuning and the emission frequencies close to those observed without reflector. Nevertheless, it has to be kept in mind that QCL 3 and QCL 4 perform already differently without any reflector at all in terms of IVL characteristics and mode spacing, therefore possibly two concurrent effects are in place, causing bad reflector coupling and increased gain without reflector (or higher losses in QCL 3). Alternatively, since the measured

mode spacing and comparison to the simulation support this, it is compelling to consider a strong reflection at the transition. Both the high optical power without reflector as well as the weak tuning can be explained monocausally this way.

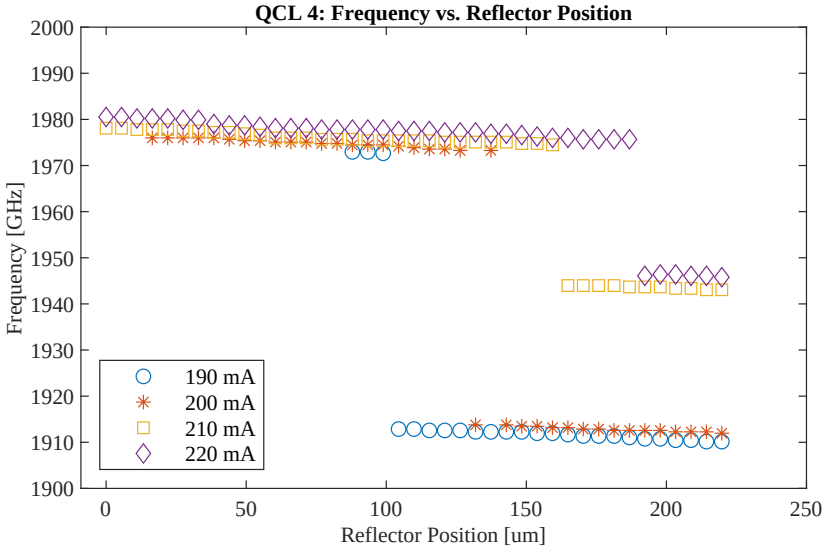

Figure 6.5.5.: Measurement similar to the one shown in Fig. 6.5.3. A much smaller continuous tuning range is presented here and the typical periodicity of the frequency is not observed compared to QCL 3. Note the doubled movement range of the reflector, for a reflector displacement of 200 µm only 3 out of 7 Bragg reflector stripes remain on the tuning section.

The far field pattern is measured in both polarizations as before with the cleaved lasers. The setup is identical with all collimating optics removed and a distance of 24 mm between laser and detector motion plane. Due to constraints in the experimental setup, only measurements without reflector membrane are carried out. The recorded data reveals that the beams are not quite as good as with QCL 1 and 2, both regarding the distortion of the beam shape and power found in the cross-polarization. Finding some radiation from the tuning section in the far field is not surprising. With the cleaved devices, the rear facet is directly coupled to free space, and the emitted power can radiate on-axis with the laser ridge, perpendicular to the antenna beam. For the tunable lasers on the other hand, any power coupled out at the transition or at the end of the tuning microstrip is to some degree directed in the z-direction, adding to the antenna beam.

6.6. Tuning of Remaining 1st Generation Devices

The remaining devices from the 1st generation, QCL 5 to 10, are similarly investigated for tunability to increase the sample size and hopefully find another well-performing QCL. They became available at a later time after the measurements of QCL 3 and 4 so

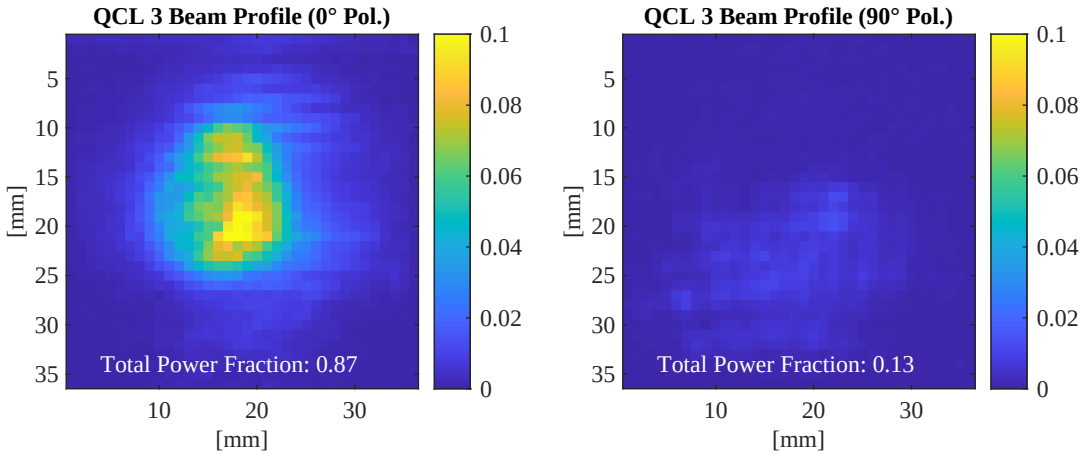

Figure 6.5.6.: Beam profile of QCL 3. The gaussicity is not quite as good as for the cleaved lasers, but the beam is fairly narrow and the polarization is still largely as expected.

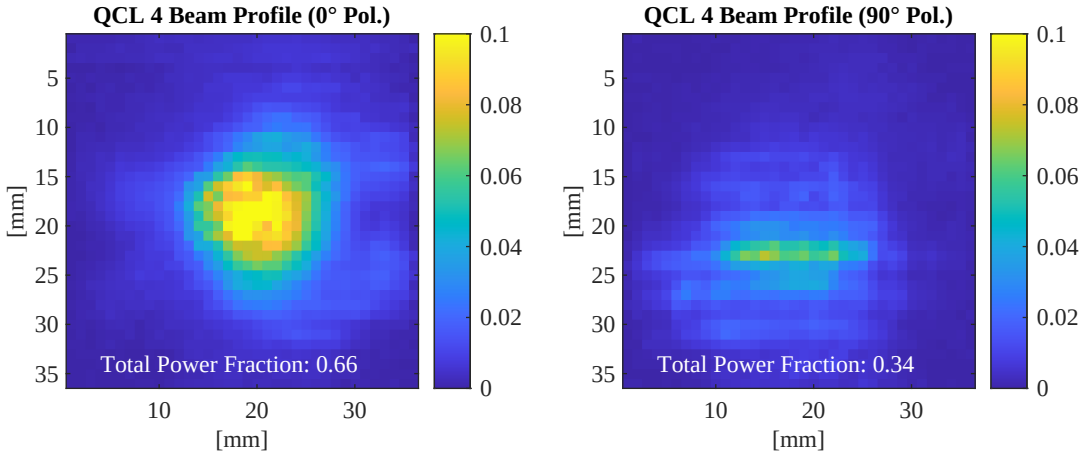

Figure 6.5.7.: Beam profile of QCL 4. A larger fraction of power is found in the cross-polarization.

far returned mixed, but promising results. The chips were cut from the same wafer and mounted to identical copper carriers as before, the only difference being their original position on the wafer and the associated variances in the layer buildup. In addition to the 1.0 mm long devices, there are several lasers with 1.5 mm length available from this batch.

The findings from the 1.0 mm devices QCL 5 and QCL 6 are directly comparable to QCL 3 and 4 from the last section, as their dimensional parameters are identical. Especially QCL 5, which is identical to the previously well-tunable QCL 3, including the front reflector parameters, is of interest here to determine if the Q-factor or any other facet-related property is causally connected to the tunability.

Again, the IVL curves without reflector serve as a starting point for evaluation and comparison. It is already clear that all lasers in this section perform differently from the previous two. This is especially evident from the lower laser threshold current without reflector, which is 145 mA for QCL 5 (188 A cm^{-2}) and 135 mA for QCL 6 (175 A cm^{-2}), significantly below the values observed in both QCL 3 (270 A cm^{-2}) and QCL 4 (251 A cm^{-2}). The corresponding IVL curves are given in Fig. 6.6.1 and Fig 6.6.2.

The 1.5 mm devices QCL 7 to 10 all have a laser threshold of 200 mA to 210 mA (179 A cm^{-2} to 187 A cm^{-2}). While the optical power varies between the lasers, the general shape of the IL curves is uniform, and the IV curves are practically identical up to the breakdown current. An example is given in Fig. 6.6.2. Curiously enough, a boost in output power is sometimes observed in the unstable current region, here seen above 312 mA accompanied by the typical voltage discontinuity.

On the following pages, a set of data is given for QCL 5, 6 and 8 since they are representative of the observations made. Each set contains spectra recorded without reflector, tuning response and beam profiles for both polarizations.

The frequency vs. reflector position plots are created from FTS measurements, where each position point and each bias current setting represent an individual measurement. Unlike QCL 3 and 4, the laser emission now contains several frequency components due to multiple active longitudinal modes. In the diagrams, the three strongest identifiable emission peaks are plotted, if present.

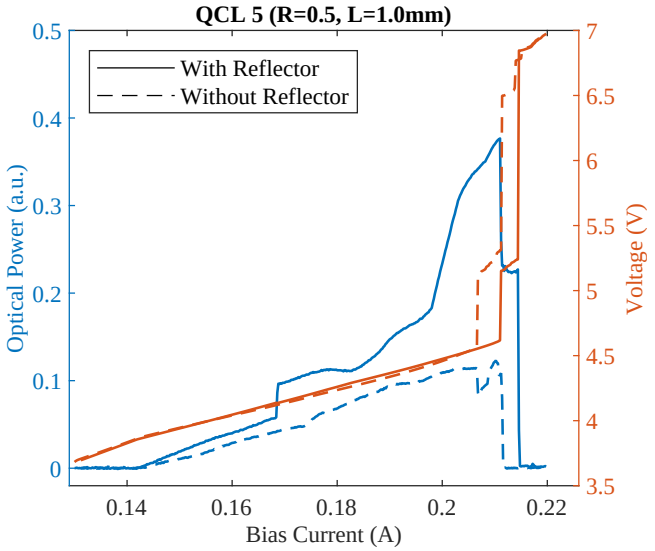

Figure 6.6.1.: IVL characteristic of QCL 5 with and without reflector membrane. Threshold current density is 186 A cm^{-2} similar to QCL 6 on the same chip and therefore significantly lower than the two previous 1.0 mm devices (270 A cm^{-2} for QCL 3 and 252 A cm^{-2} for QCL 4). The threshold current is unaffected by the presence of the reflector, while slope efficiency improves. Electric domain formation is delayed due to a stronger intracavity field resulting in enhanced photon-driven transport.

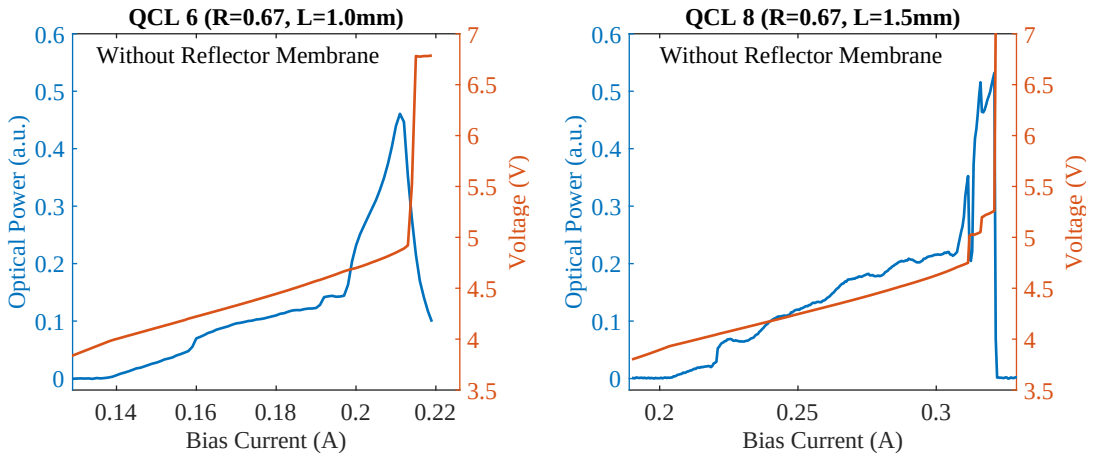

Figure 6.6.2.: Left: IVL characteristics of QCL 6 without reflector membrane. **Right:** IVL characteristics of QCL 8, threshold current density is 183 A cm^{-2}. The increased optical power in the unstable bias region, here seen above 312 mA, unexpectedly occurs in some devices.

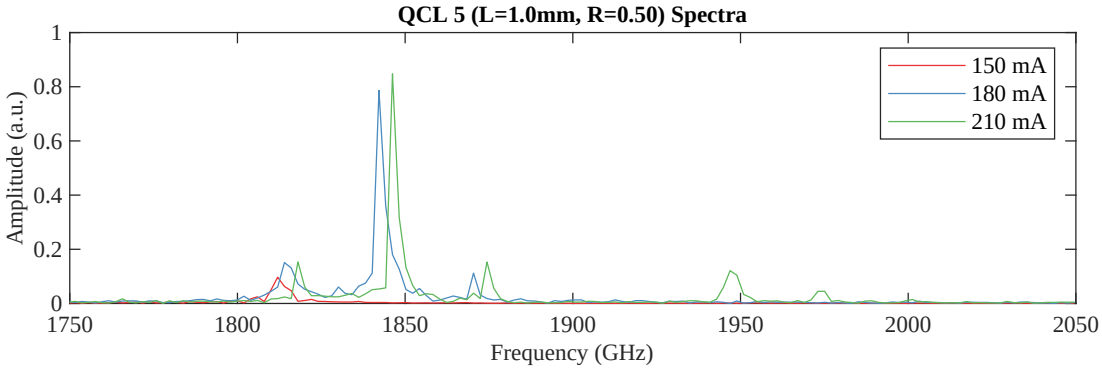

Figure 6.6.3.: Spectra of QCL 5 at various bias current settings. The mode spacing is 27.4 GHz.

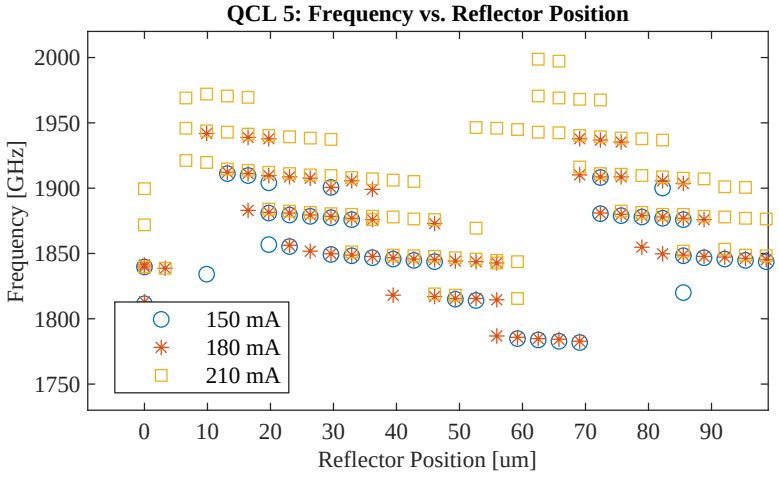

Figure 6.6.4.: QCL 5 tuning results. 11 GHz tuning is accessible. Typical "bands" occur where lasing ceases.

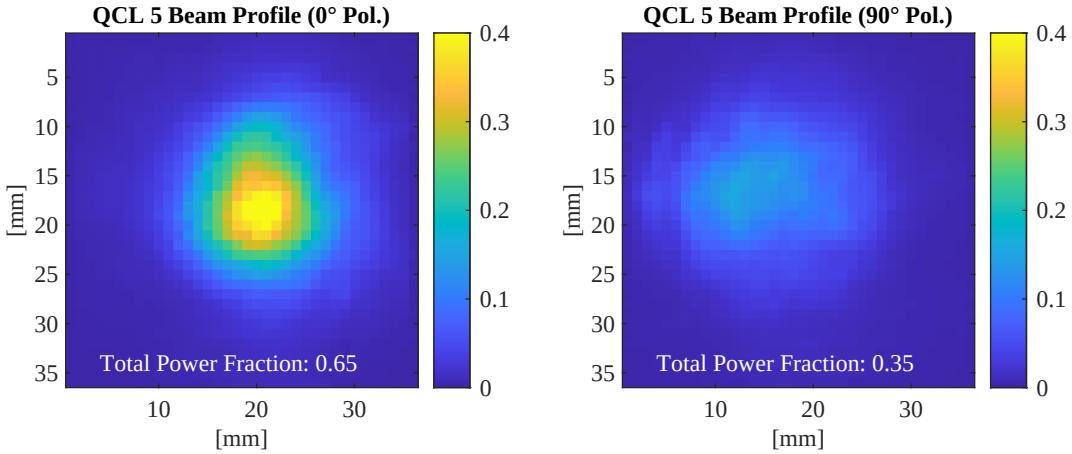

Figure 6.6.5.: Left: Beam profile for the E-field vector parallel to the laser ridge. The antenna beam is designed for this polarization. Divergence and shape are consistent with simulations. **Right:** Beam profile in orthogonal polarization. All power measured originates from undesired effects.

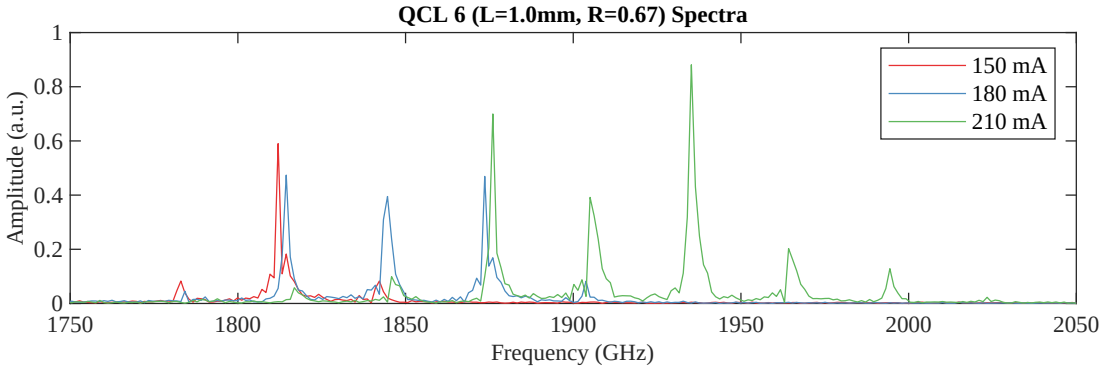

Figure 6.6.6.: The spectra of QCL 6 reveal enhanced gain at higher frequencies compared to QCL 5. Mode spacing is 28.3 GHz.

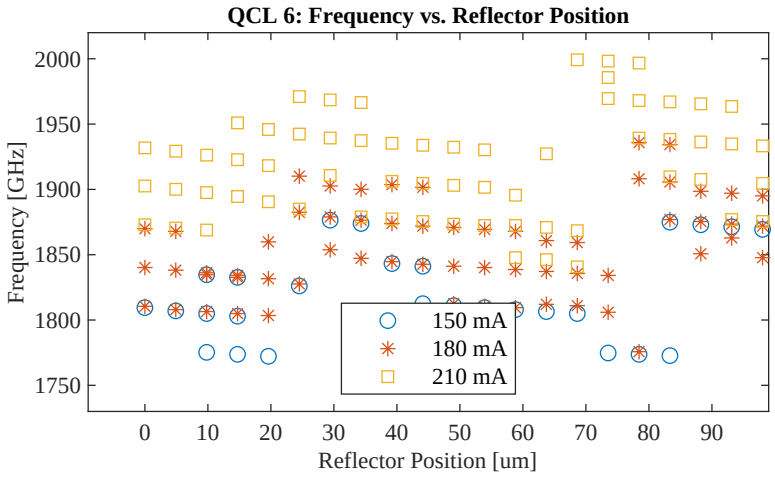

Figure 6.6.7.: This laser is well-tunable, with some lasing modes traversing more than a full FSR at select currents. Non-uniform tuning is especially well observable in this device.

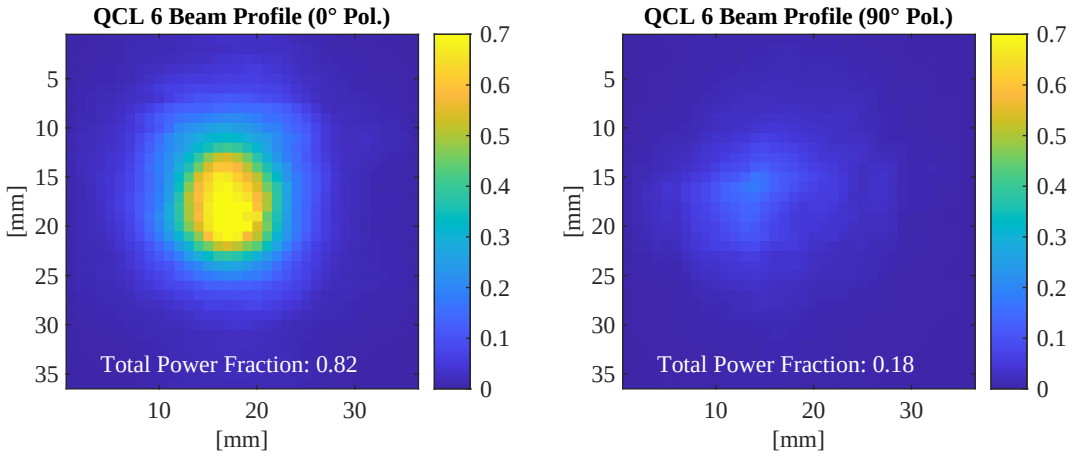

Figure 6.6.8.: QCL 6 far field measurement.

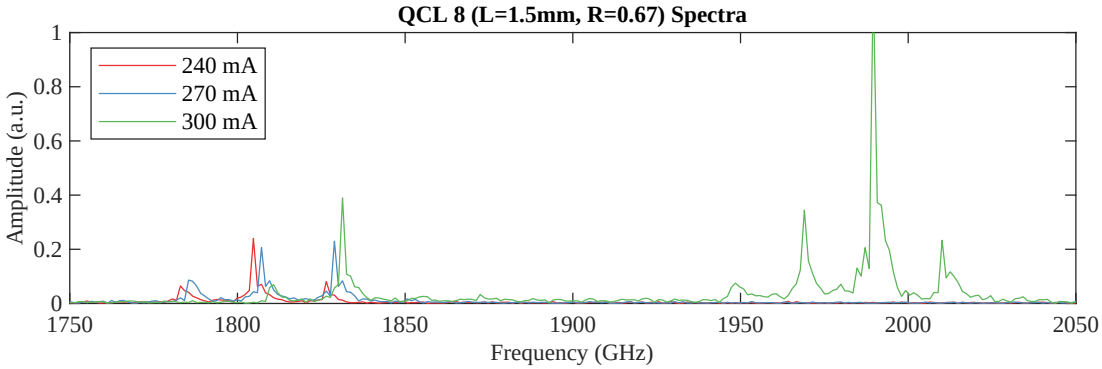

Figure 6.6.9.: Similar to QCL 7 there is a gap from 1.83 THz to 1.94 THz found in the spectrum. Since both lasers are located next to each other on the same chip, this could have a systematic cause related to the position on the wafer. Mode spacing is 20.8 GHz

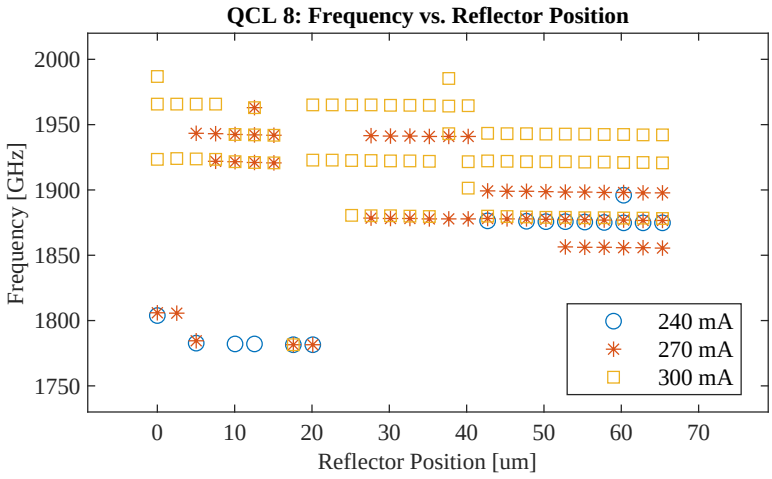

Figure 6.6.10.: Only around 1 GHz continuous tuning is possible. An effect of the reflector position on the modal gain is present. This is the only laser where the cavity resonance frequency seems almost unaffected by the reflector position.

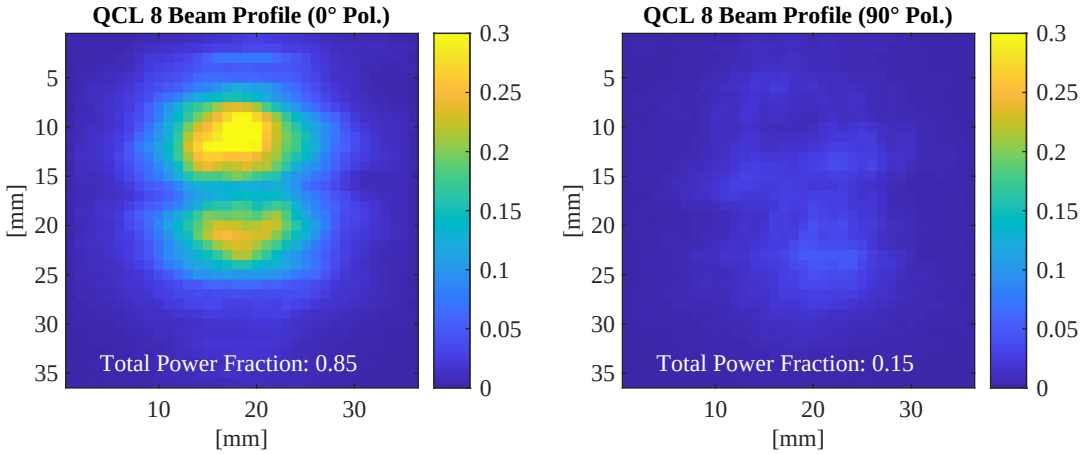

Figure 6.6.11.: QCL 8 far field measurement. This is the only device that shows a clear double peak in the beam profile.

Chapter 7.

Discussion - 1st Generation Devices

7.1. Manufacturing Deviations from the Model

The findings presented in the last chapter suggest that a profound analysis of the possible causes for the inconclusive tuning behavior is necessary to avoid these issues in a planned second generation of lasers.

Optical microscopy imaging is the means of choice to verify structural integrity and find deviations of the lasers from the model. Electron beam microscopy is unfortunately unavailable, but the metallic topology can be resolved with white-light interferometry.

In terms of surface roughness and contamination with particles, the principal question is if a sufficient coupling between the membrane reflector and tuning section can be assured. The extent of any irregularity in the z-direction should be as low as possible, with 3 µm to 4 µm being the maximum tolerable gap between membrane and structure to retain a good reflection (see Fig. 5.2.9).

Upon inspection, it becomes clear that the chip surface is not as clean and uniform as assumed during the design. Instead, different forms of contamination of varying severity can be identified. First, a "sputter" of tiny circular droplets, approximately from 2 µm to 10 µm in diameter, is spread over the wafer. Their origin is unclear, and the height could not be measured in white-light interferometry due to limited resolution. Possibly their impact is limited to optical appearance. They seem to be different in nature than some other observed droplets that are larger in size and clearly show a convex shape, as evident from refraction of underlying patterns.

In addition, dust particles of larger sizes are found in some places, possibly typical dust particles emerging from non-cleanroom handling of the lasers in the laboratory. Such a particle was found close to the tuning section only on one occasion, which could

be removed with careful movement of the membrane.

Last, elevations or distortions in the BCB surface are visible at some points. They are highly detrimental to tuning efforts when found within the contact area of the membrane since they tend to stick out of the planar surface by a large degree, preventing any reflector coupling. This is the case e.g. for QCL 4.

Microscopy images of QCL 3 and QCL 4 are shown in Fig. 7.1.1 with a clear indication of surface irregularity at the tuning section of QCL 4, consistent with the tuning experiment results. Also shown in Fig. 7.1.2 is an excellent example of larger particles. For additional images, refer to appendix A.

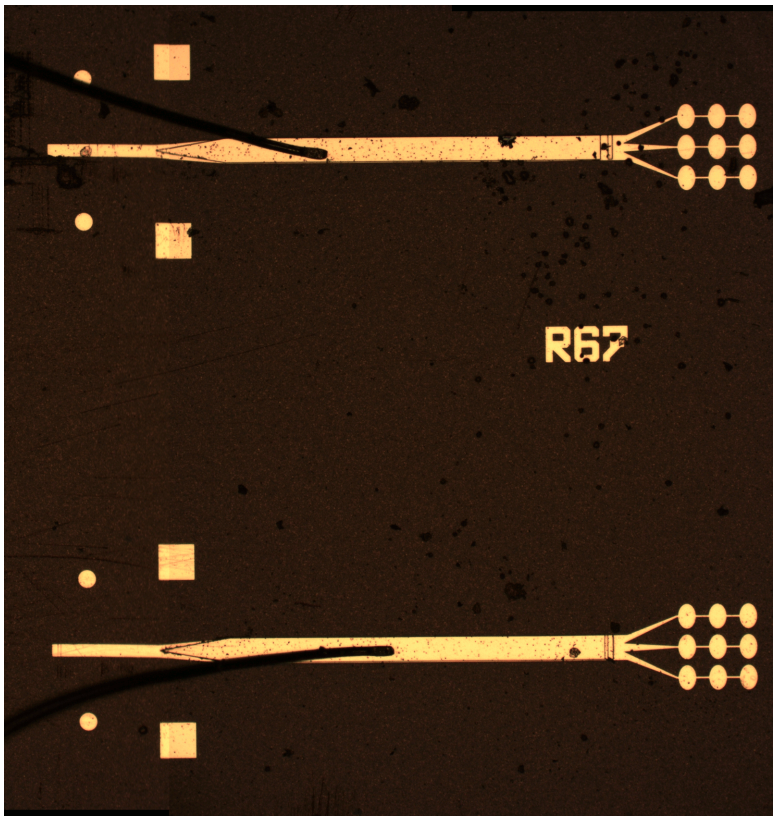

Figure 7.1.1.: Full view of QCL 3 (lower) and 4 (upper). Also visible aside from the lasers are the bonding wires and markers for membrane positioning. Some surface contamination can be identified, especially on QCL 4, where imperfections close to the tuning section are a possible cause of the ineffective tuning.

Regarding the metal structuring quality, the most critical issues are dimensional accuracy and gold layer defects. Luckily this appears to not be a concern here, with a slight offset between GaAs and gold metallization of ca. 3 µm in the lateral direction being the only observed in-plane deviation from the model resulting from the lithography process. The gold film integrity is good throughout all devices; the dark spots seen on some lasers can be identified as surface contaminants at higher magnifications that do

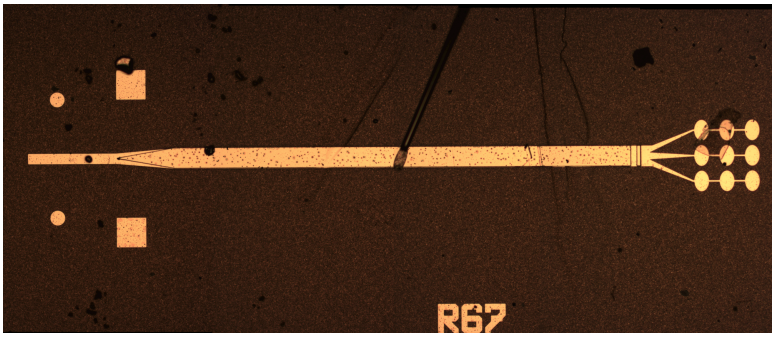

Figure 7.1.2.: QCL 8 is an example of the worst possible case, a large particle ca. 20 µm in diameter is ingrained in the tuning section. This device is almost not tunable. Furthermore, the large translucent particle on the antenna is possibly responsible for the double beam seen in later measurements.

not affect the metal and are not expected to cause issues as long as they are not close to the tuning section or on top of the radiative antenna structures.

Contrary to that, the BCB planarization is not as reliable. From white-light interferometry imaging it can be concluded that the BCB layer is ca. 2 µm thinner than the GaAs laser ridge, which leads to discontinuities whenever the gold layer covers a GaAs-BCB interface. This is the case at the tuning section transition and at the front reflector towards the antenna. The same step can be made visible under an optical microscope with a high numerical aperture lens and, consequently, a small field depth. Focussing the two planes successively (see Fig. 7.1.3) while observing the travel distance of the microscope stage as measured by a digital micrometer caliper yields 2.3 µm for the step. This is confirmed with white-light interferometry, see Fig. 7.1.5. A possible consequence of this discontinuity is deteriorated performance of the transition from laser ridge to tuning section.

7.2. Impact of the Identified Issues

In this section, the impact of the issues identified so far is analyzed to quantify the effects on the tuning efficiency of the lasers and find possible solutions. Concluding from the previous findings, two suspected problems could interfere with the intended tuning principle: Degraded reflector coupling arising from surface irregularities and degraded performance of the transition taper due to a planarization discontinuity, mainly in the form of increased reflection back to the ridge.

In the first case the silicon membrane is prevented from aligning flat on the chip surface, and the reflector stripes do not couple sufficiently to the stray field of the tuning section, which is concentrated close to the microstrip edge. A significant part of the power in the tuning section then propagates past the reflector until it is reflected and

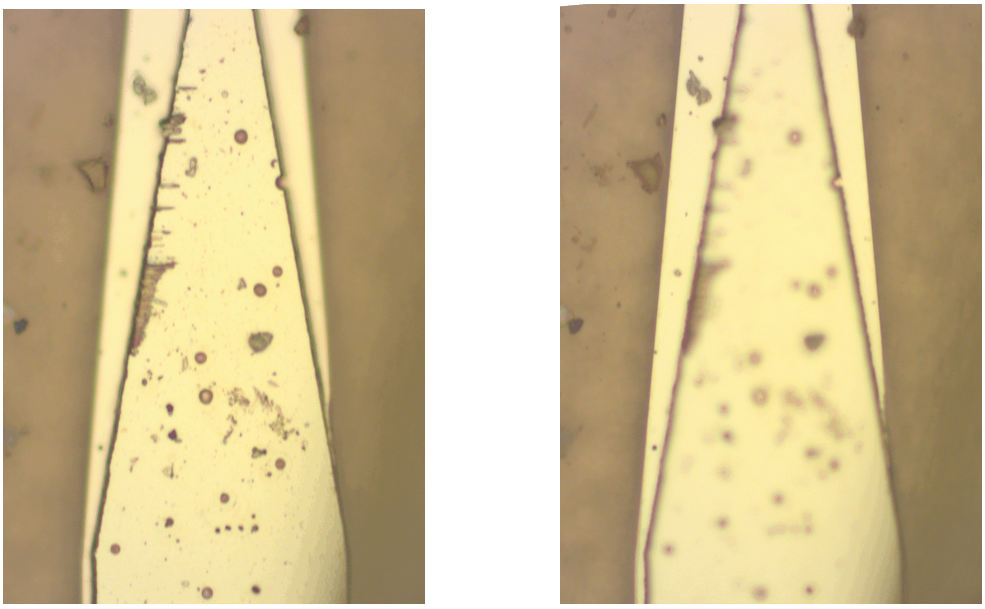

Figure 7.1.3.: Taper section of QCL 4. The underlying GaAs triangle is visible through the top metallization. **Left:** Upper focus on the GaAs plane **Right:** Lower focus on the BCB plane. The travel distance of the microscope stage is 2.3 µm between the two images.

partially radiated at the end of the tuning section microstrip. The resulting phase and amplitude of the total reflected wave is a superposition of contributions from the reflector and this residual wave. A threshold value for the gap was determined from the initial simulations during the design phase to be around 3 µm to 4 µm before reflector efficiency starts to decrease, a value that is easily met or surpassed by some of the identified surface irregularities. An additional source of error is the alignment of the membrane. As a result of mechanical constraints of the experimental setup, the distance of the microscope lens to the cold plate is approximately 10 cm, requiring a low numerical aperture with limited resolving power. An offset in the lateral direction of up to 5 µm could go unnoticed and further reduce performance. Fortunately, the effect of this is not prohibitively strong, manifesting in 0.2 dB to 0.3 dB overall reduced reflection and some distortions of the frequency dependency as is shown by respective simulations. A realistic scenario considering the limitations of the system and taking into account observations made by optical inspection through the microscope during alignment is a reflector offset of 3 µm in the z-direction and 3 µm lateral offset.

To determine if the lower reflectivity resulting from these alignment uncertainties alone can explain the measured tuning behavior of the lasers, the simulation model is revisited to identify conditions that can explain the experimental findings. Especially for the devices that remained at a more or less stable frequency and showed little tuning

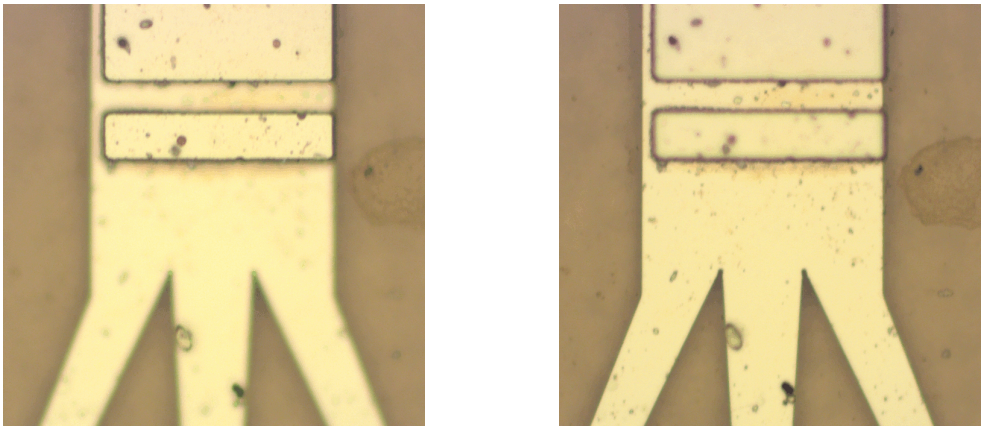

Figure 7.1.4.: Image of the front reflector and the antenna split created similar to Fig. 7.1.3. The slight lateral offset of the metallization is well visible here.

response to reflector movement, the reflector coupling must be extremely low.

In an attempt to answer this question, first simulations are carried out with large misalignment values. As it turns out, the microstrip leakage field still couples to the reflector stripes for rather large gaps; see Fig. 7.2.1 for a scalar plot of the electric field with $\Delta z = 10\,\mu\text{m}$. The effect on the reflected wave in terms of amplitude and phase are shown in Fig. 7.2.2 and Fig. 7.2.3. While the results confirm a generally lower reflectivity with significant modulation from the superposition of contributions from the reflector and the open-ended tuning microstrip, a variable phase shift is still present. Suppression of the tuning mechanism through membrane misalignment alone seems to require unrealistically large gaps, with 10 µm already being quite large and impossible to miss during visual inspection through the microscope. The only occasion with a clearly visible airgap is QCL 8, which suffers from a large particle directly on the tuning section. Several other QCLs with bad tuning performance, e.g. QCL 4, 9 and 10, did not show visible signs of a large gap. In conclusion, alignment parameters alone can not reconcile the simulation results with experimental findings.

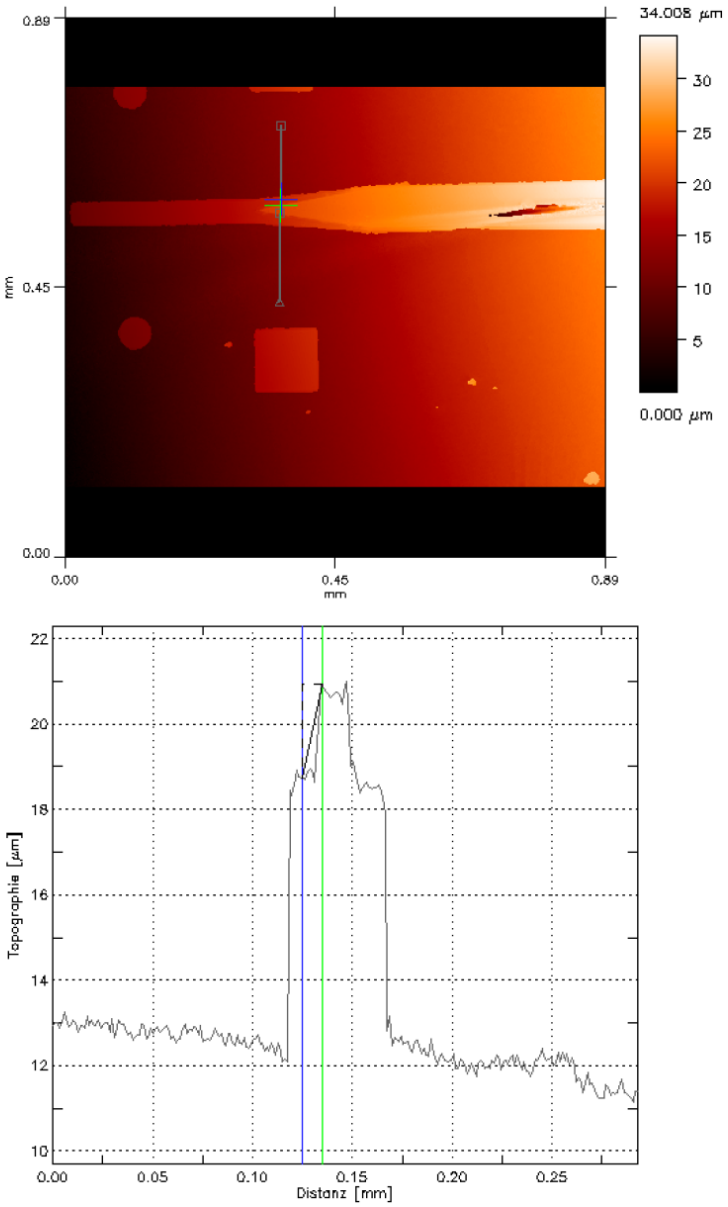

Figure 7.1.5.: White light interferometry imaging of the taper and tuning section of QCL 3. The elevation profile along the blue marked line reveals a step in the top metallization from GaAs to the BCB layer. The data shows that the BCB surface is approximately 2 µm lower than the laser ridge. The distance to the ground plane is measured through BCB and hence appears shorter due to refraction.

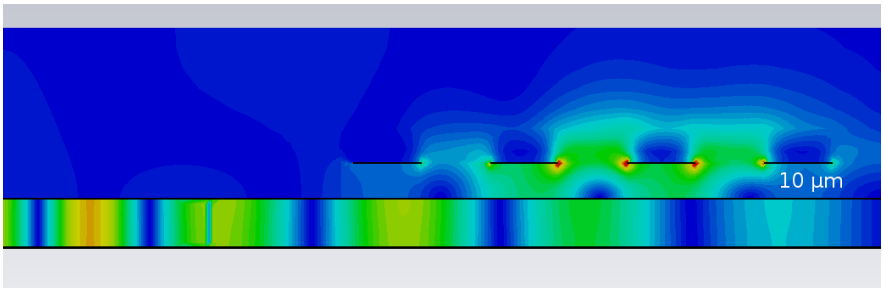

Figure 7.2.1.: Lateral view on a cross-section along the symmetry axis of the laser. Shown is the E-field absolute value for a wave incident from the left coupling to the first four gold reflector stripes with a 10 µm gap.

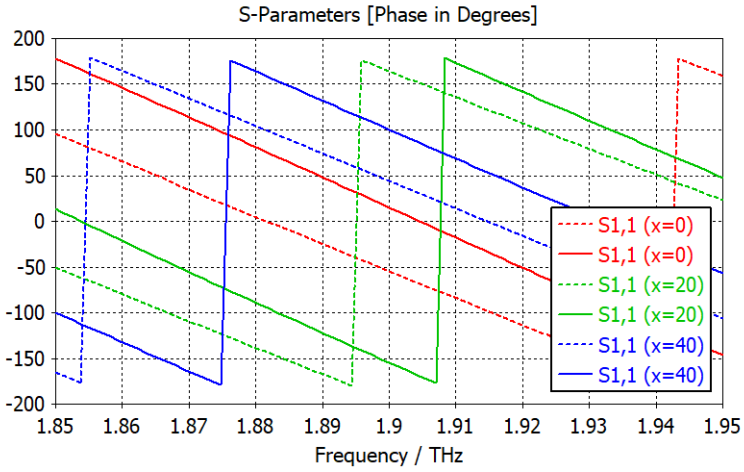

Figure 7.2.2.: Phase of the reflected wave for $\Delta z = 3\mu m$ (dashed) and $\Delta z = 10\mu m$ (solid) for reflector positions x = 0 µm, 20 µm and 40 µm. The phase shift induced by reflector movement is still observed for large gaps.

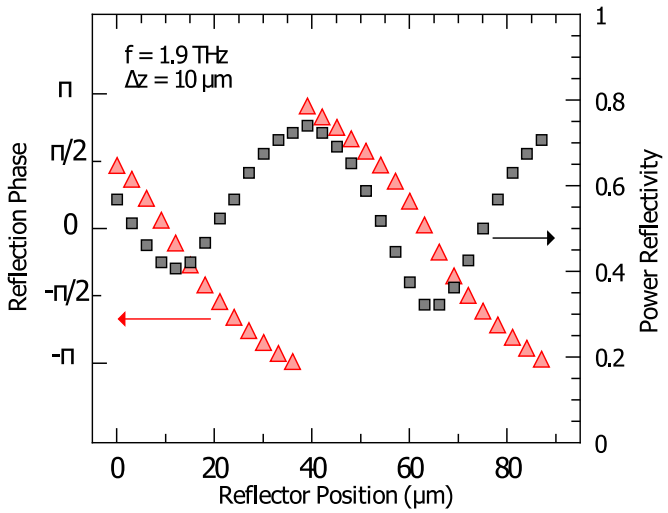

Figure 7.2.3.: Simulated phase of the reflected wave at 1.9 THz as a function of reflector position, now with a large vertical gap of 10 µm between reflector and tuning section. Even for this excessive value, the desired phase shift is still present. Nevertheless, the reflected amplitude is generally lower and heavily modulated, a consequence of reflections from the far end of the tuning section.

In addition to the reflector membrane misalignment investigated in the analysis above, the second important issue identified in the last chapter - the BCB planarization offset - has to be considered. Initially, this is done without any reflector misalignments to isolate the BCB step effects from membrane coupling effects. A combination of both can eventually be compared to the experimental findings.

The part most sensitive to a BCB planarization offset with respect to a diminished effectiveness of the movable reflector is the transition taper. The top gold layer will have a discontinuity where it transitions from GaAs to BCB. Such a step seems initially unfavorable for a part designed with minimal reflections in mind. A critical question in this context is if the GaAs sidewall of the transition section is metallized (see Fig. 7.2.4). Since the gold layer is sputtered vertically during manufacturing, it is unclear if continuous metallization is achieved on these surfaces. The distinction has a dramatically different outcome: If metallization is continuous, the performance of the transition is actually improved since the impedance mismatch between ridge and tuning microstrip decreases. If conductivity is broken on the other hand, reflections occur and resonance effects introduce a strong frequency dependency. The simulations are carried out first for the transition only, which is simulated as a 2-port device to isolate the impact of the surface step and metallization from other reflections, see Fig. 7.2.5. From the power amplitude S11 parameter alone it becomes clear that an unmetallized side wall would lead to prohibitively strong reflections, up to -5 dB (see Fig. 7.2.6) for some frequencies. S11 of the complete transition and tuning section with reflector is shown in Fig. 7.2.7 and emphasizes the effect of interferences from those parasitic reflections. In general, the behavior of the complete laser becomes less predictable since the phase shift achieved by reflector movement now is a function of frequency as well, which was much less pronounced previously (see Fig. 7.2.2).

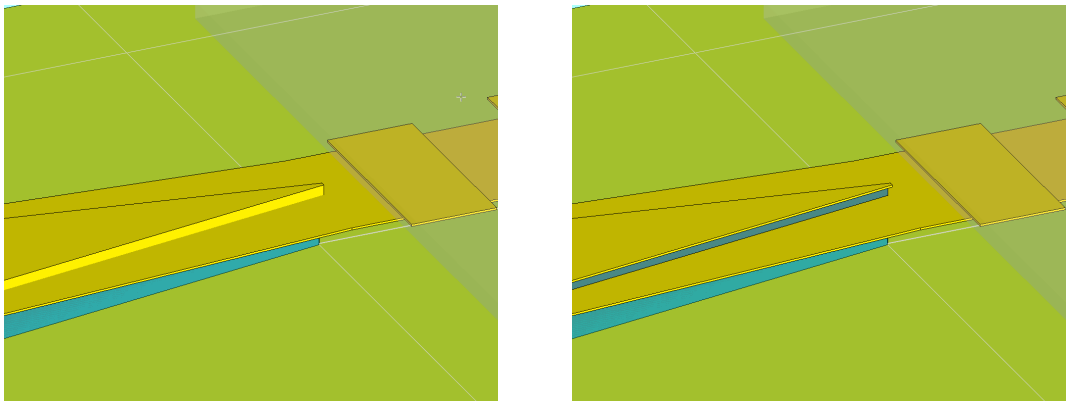

Figure 7.2.4.: Visualization of the uncertain side wall metallization on the transition resulting from BCB planarization tolerances.

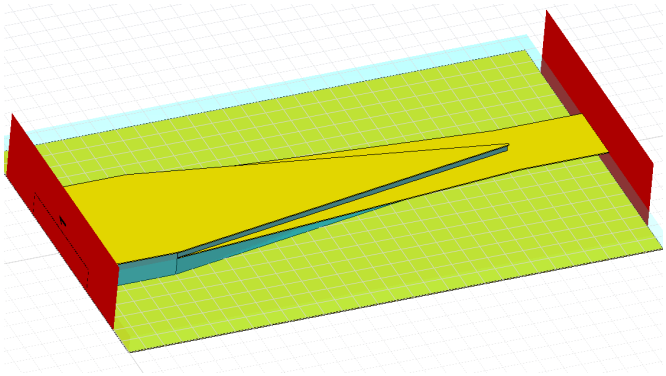

Figure 7.2.5.: Simulation model for the S-parameters of the transition taper alone. The second port absorbs transmitted power to isolate the effect of the taper side wall metallization from reflections at the end of the tuning microstrip. Results are shown in Fig. 7.2.6.

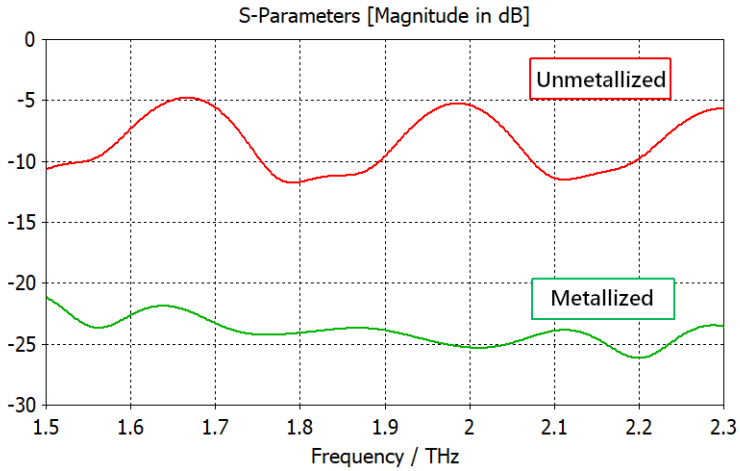

Figure 7.2.6.: S11 of the tapered transition section alone. Reflections around −5 dB occur at 1.99 THz well within the laser bandwidth. BCB planarization offset is 2.3 µm

.

While these findings shine some light on the suspected issues and their consequences for tuning performance, it must be considered that the validity of simulation models can depend on many factors, some of them unknown or not easily incorporated. In particular, the simulations with unmetallized side wall depend sensitively on the exact BCB offset, metal thickness and length of the "slit" as well as meshing parameters of the field solver. It is reasonable to take a step back from this microscopic analysis and also consider a broader approach, as is done in the next chapter.

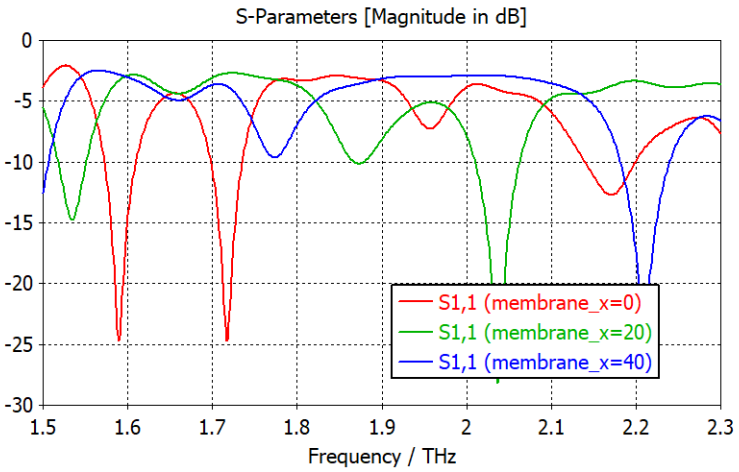

Figure 7.2.7.: S11 of the complete tuning section, including the transition with unmetallized side walls and reflector membrane. BCB height is 11.3 µm, leaving an exposed side wall 2.3 µm high. A strong frequency dependency of the amplitude of the reflected wave appears.

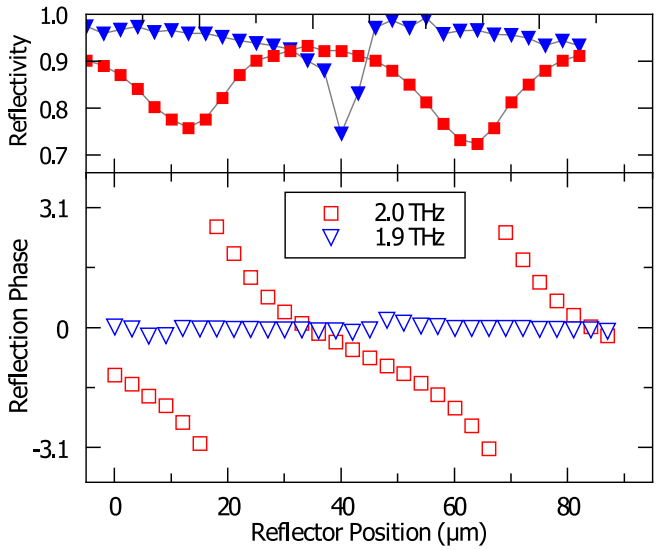

Figure 7.2.8.: Simulated phase of the reflected wave at 1.9 THz and 2.0 THz as a function of reflector position with gold metalization missing at the transition section GaAs side walls (2.3 µm BCB planarization offset). In contrast to a continuous metal layer (see Fig. 7.2.2), the phase modulation strongly depends on frequency. For several frequency bands (e.g. from ca. 1.85 THz to 1.95 THz) the tuning mechanism is strongly suppressed due to resonant reflections. These resonance frequencies are sensitive to the exact metallization defect geometry; a comparison to measurements is therefore qualitative only.

7.3. Analytical Coupled-Cavity Model

In the last chapter, it could be established that the lasers' identified and hypothesized structural features do not fully explain the measurements concerning tunability and spectrum. Since a coupled-cavity effect induced by an unexpectedly strong reflection within the cavity, most likely from the tapered section, could presumably explain the observed power modulation, additional steps are taken to investigate this further in a more generalized way. The model used here extends the well-known Fabry-Perot resonator by adding a third mirror to create two coupled cavities. The first cavity corresponds to the GaAs-filled laser ridge, whereas the second cavity extends from the impedance matching to the movable reflector, although the model itself is not restricted in its parameters. A straightforward way to calculate the resonance frequency and threshold gain as a function of the movable reflector position is to treat the total construct as a two-mirror cavity of length L, where the second mirror has a complex amplitude reflectivity coefficient $r_2(\nu, d)$ that includes all phase and magnitude effects of the second cavity (see illustration of the concept in Fig. 7.3.1).

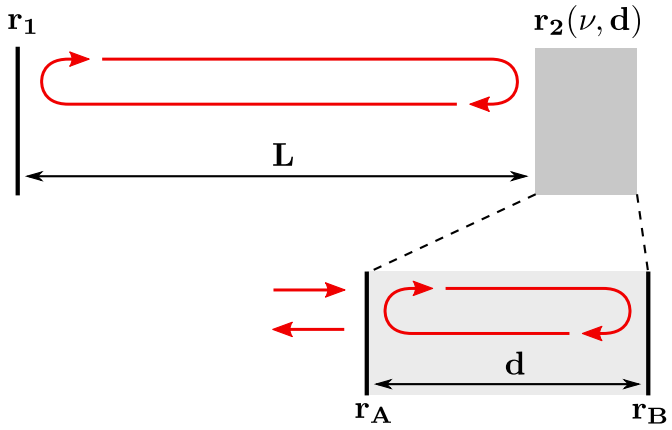

Figure 7.3.1.: Model of a three-mirror cavity. The frequency response of the first cavity of length L can be calculated if the (complex) reflection coefficient $r_2(\nu, d)$ of the second cavity is known.

The standard way to obtain the reflection $r_2(\nu, d)$ is to calculate the sum of all transmitted and reflected amplitudes:

$$r_2(\nu, d) = r_A + t_A^2\, r_B\, e^{2i\delta} + t_A^2\, r_A\, r_B^2\, e^{4i\delta} + t_A^2\, r_A^2\, r_B^3\, e^{6i\delta} + \ldots \tag{7.1}$$

with phase length $\delta = 2\pi d\nu/c$. Some care has to be taken with regard to the phase shift on reflection. In the literature this calculation is usually done for a solid etalon made from a dielectric material, which implies a phase shift $\Delta\phi = \pi$ on internal reflection and

$\Delta\phi = 0$ on reflection from the outer surfaces as well as no phase shift on transmission. For a partial mirror with symmetrical refractive index of the medium on both sides the relation is only determined to

$$\Delta\phi_{refl} = \Delta\phi_{tran} + \pi \tag{7.2}$$

as a result of energy conservation without further knowledge of the mirror's detailed construction [151]. For such "free-standing" mirrors, the cavity reflection coefficient then becomes

$$r_2(\nu, d) = r_1 + \frac{(1 - r_A^2)\, r_B e^{2i\delta}}{1 + r_A\, r_B\, e^{2i\delta}} \tag{7.3}$$

On a side note, the differences in phase shift between the resonator types change the resonance condition by $\Delta\delta = \pi/2$ but have no further impact on the spectral shape. From here, the power reflectivity and phase of the reflected wave are obtained through

$$R_2(\nu, d) = r_2(\nu, d)\, r_2^*(\nu, d) \tag{7.4}$$

$$\phi_2(\nu, d) = arg(r_2(\nu, d)) \tag{7.5}$$

where some attention has to be paid regarding the phase wrapping that usually limits the $arg()$ function to $[-\pi, \pi]$, which is undesired in this case.

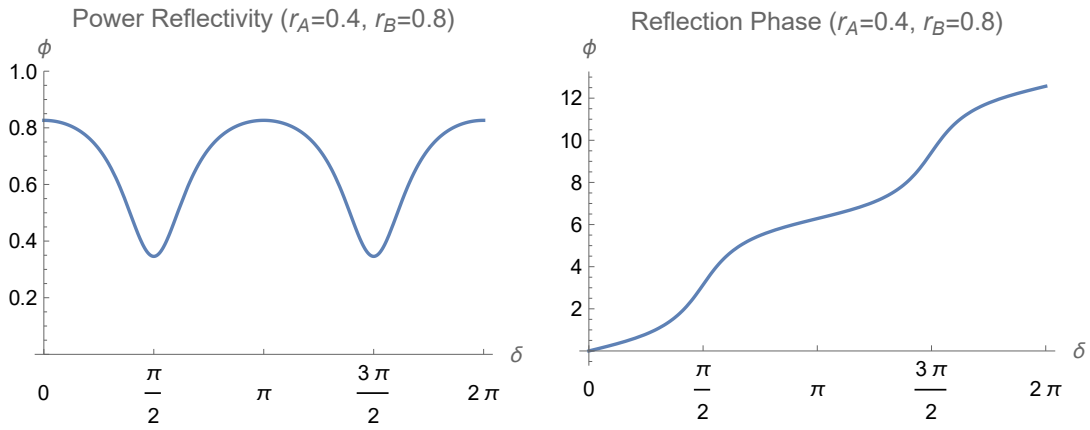

Figure 7.3.2.: Left: Power reflectivity R_2 of a 2-mirror resonator. The horizontal axis is given in units of phase length $\delta = 2\pi L\nu/c$. **Right:** Phase of the reflected wave.

With $\phi(\nu, d)$ it is now possible to solve the resonance condition for the entire cavity.

After one roundtrip the phase difference must equal multiples of 2π:

$$\frac{4\pi\nu L}{c} + \phi_2(\nu, d) = 2\pi n \tag{7.6}$$

which is solved numerically to find the resonant frequencies depending on the "tuning" cavity length d. As it turns out, the frequency tuning $\partial\nu/\partial d$ is not uniform and instead varies periodically.

The model is completed with a consideration of the threshold gain in such a Fabry-Perot resonator

$$G^{FP}_{m,th} = \alpha_w + \frac{1}{2L} ln \frac{1}{R_1 R_2} \tag{7.7}$$

with waveguide loss α_w. $G^{FP}_{m,th}$ is a function of both d and ν and is maximal at points in the parameter space where tuning is the most effective, see Fig. 7.3.3 for an illustration of total cavity resonance frequencies and threshold gain.

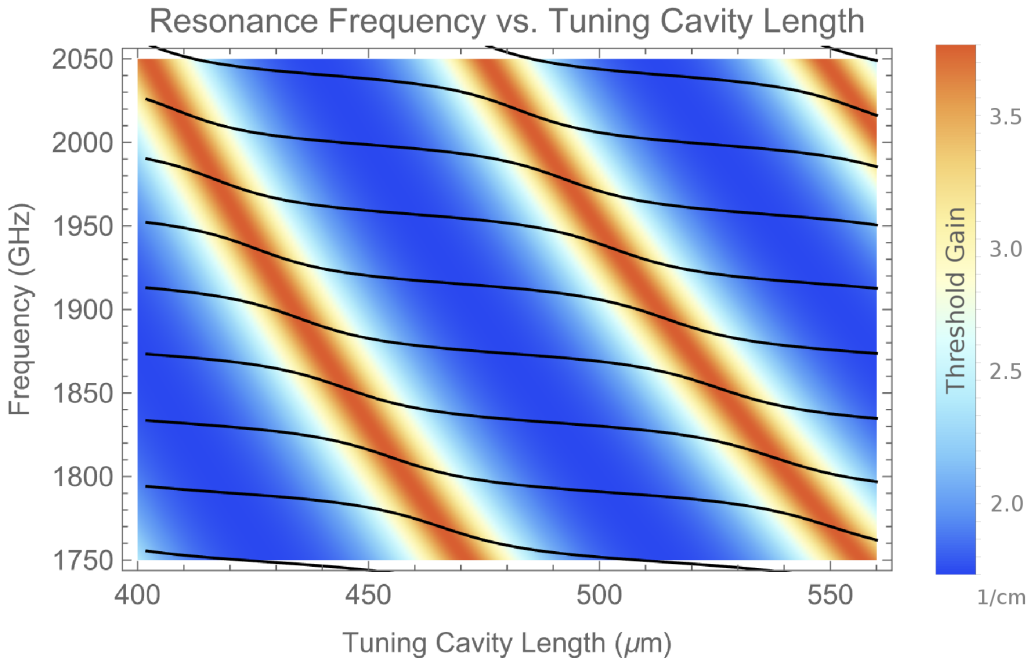

Figure 7.3.3.: Solid lines: Cavity resonance frequencies as a function of tuning length d, found as numerical solutions of Eq. 7.6. **Color map:** Cavity threshold gain with α_w set to zero. Parameters are $r_1 = r_B = 0.8$, $r_A = 0.4$, $L = 3.6\,\text{mm}$ optical length including refractive index chosen to imitate the physical devices. Tuning cavity optical path length d =400 µm to 560 µm yields results similar to the features seen in the measurements. This is a reasonable value for the distance of the reflection phase center for the complex movable reflector structure.

A comparison of the predictions made by this model to measurement data indicates an agreement of the key features in many cases. The "gaps" coinciding with the areas of increased threshold gain are found in most devices either in the form of complete suppression of lasing or reduced optical power, see Fig. 7.3.4. The non-uniform tuning in high and low-threshold regimes is also apparent in several measurements, with the stronger tuning often hidden by ceased lasing, although on some occasions, e.g. in QCL 6, also observed directly. While the model can explain essential features of the tuning data on most devices, it is clear that additional effects remain beyond the capacity of this model. Most notable are seemingly irregular frequency jumps and less clearly distinguishable threshold gain regions for several devices. This also makes it hard to extract tangible numbers from comparing the model to the experiment. The foremost question at this point is how strong the undesirable reflectivity r_A must be to reproduce the observed frequency tuning. While this can not be answered for all devices with high confidence, an amplitude reflectivity of $r_A >= 0.25$ is certainly a lower bound. In terms of power reflectivity this is $-12\,\mathrm{dB}$, much higher than the ca. $-20\,\mathrm{dB}$ calculated in the initial CST simulations. Calculations with unmetallized taper side walls, see chapter 7.2, gave S11 results between $-10\,\mathrm{dB}$ and $-5\,\mathrm{dB}$, a rough value that could match the model and experiment. It must be noted that the impact of the frequency dependency of the simulated S11, both in amplitude and phase, can not be evaluated within the analytical model presented here. Other explanations, e.g. gold diffusion into a gap between GaAs and BCB during the sputtering step induced by stress within the materials, remain speculative. Clarity could be brought with electron microscopy of a cross section of this part of a laser.

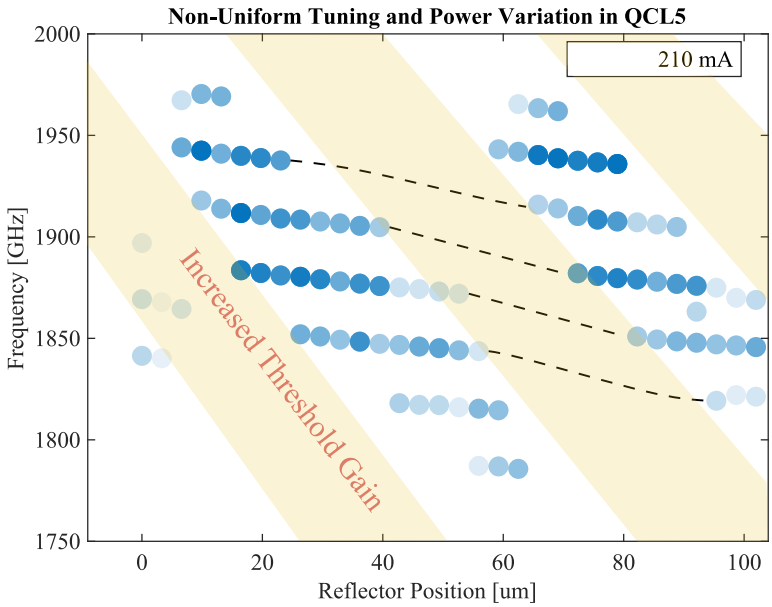

Figure 7.3.4.: Experimental tuning data shows the same features predicted by the model. The data shown here originates from QCL 5. Lasing is suppressed in areas of increased threshold gain, and the resonance frequency shift deviates from the slope observed outside these areas, indicated with dashed lines. Although this is not always observed clearly in other devices, at least in QCLs 5, 6, 8 and 9, similar effects are present. Marker intensity is scaled by output power.

Chapter 8.

2nd Generation Tunable QCLs

8.1. Goals and Motivation

The analysis in the preceding chapters revealed two principal points: first, the tuning mechanism generally works and is worth pursuing further, and second, the results from the first generation of tunable QCLs clearly indicate what should be focused on. A review of critical points and possible changes suggests several desired improvements: better surface quality regarding BCB planarization and roughness, shorter ridges to obtain lasers operating on a single mode and an uninterrupted top metal surface at the tuning strip transition. Since the time of manufacturing of the QCLs discussed so far, the processes involved have matured and after discussion with the QCL work group at ETH Zürich, it was decided that a renewed manufacturing run using still available material from the same QC multilayer structure as used before is reasonable to achieve these stated goals.

For the new design, the ridge length is reduced to ca. 600 µm to find a balance between satisfactory output power and increased chances of single-mode operation. Decreasing the resonator length is a commonly used approach with the intent to both increase the FSR of the cavity and reduce the total cavity gain at a given pump level. Both effects favor the resonator mode closest to the material gain peak. The exact length of each laser ridge on the wafer is varied from 580 µm to 620 µm for otherwise identical designs to find an optimum between material gain profile and cavity spectrum and introduce some degree of variance into the standing waves originating from taper or antenna reflections such that a favorable configuration can be found.

The front facet is chosen with only one set of parameters to reduce the total number of different designs, since in the previous generation no advantage of either 67% or 50% power reflectivity could be determined. The reflectivity for this design is 60%.

The last design change is a tuning strip slightly longer by 50 µm to allow a more extensive reflector movement range without reflector stripes "falling off" the far end of

Figure 8.1.1.: CAD drawing of a second generation device from which the lithography masks are produced. The ridge is shortened to 600 µm, with improved alignment markers visible on the left. GaAs in green, top metalization in red.

the tuning strip, as was the case before.

Aside from the laser itself, two sets of visual markers on the wafer close to the tuning section have been added to allow easier lateral alignment of the reflector membrane and providing references for the longitudinal position.

At the time of manufacturing the first generation tunable QCLs, the BCB planarization process was in its early stages and has improved since then with the experience gained. The better surface matching of BCB and GaAs is expected to remedy the issues that occurred before due to the underperforming transition region. In addition to that, the gold sputtering is now carried out at an angle of 30° instead of perpendicular to ensure the metalization of any protruding GaAs triangle side walls, see ch.7.1.

8.2. Device Overview

A total of 14 individual lasers from this batch of QCLs were available, and all were tested for tunability. As before, one laser chip containing QCLs 11 and 12 was cleaved off right at the beginning of the taper section to separate any effects induced at that point and carry out baseline measurements for IVL curves and beam profiles. Chip 5 and 6 contain unmodified devices matching the design shown in Fig. 8.1.1. The remaining lasers are modified at a later point using Focussed Ion Beam etching to narrow the ridge metalization from 70 µm down to 50 µm.

QCL	Chip	Ridge L	Comments
11	4	615 µm	Cleaved
12	4	618 µm	Cleaved
13	5	603 µm	
14	5	606 µm	
15	6	609 µm	
16	6	612 µm	
17	7	579 µm	FIB
18	7	582 µm	FIB
19	8	585 µm	FIB
20	8	588 µm	FIB
21	9	591 µm	FIB
22	9	594 µm	FIB
23	10	597 µm	FIB
24	10	600 µm	FIB

Visual inspection confirms an improved surface quality with much fewer irregularities compared to the previous generation. In addition, there is no discernible in-plane offset between GaAs etching and the top metal layer this time. Finally, the transition section that is convincingly suspected of causing at least some of the issues found in the first-generation lasers through out-of-spec reflectivity appears substantially smoother in optical microscope images. A BCB-GaAs height step could either not be resolved by depth-of-field probing this time or only weakly. This is supported by white-light interferometry, where a step could still be detected. Still, the maximal measured elevation difference is 0.7 µm on some devices, approximately one third of the previous value. Overall, the new devices deviate much less from the simulated models and would be expected to perform better.

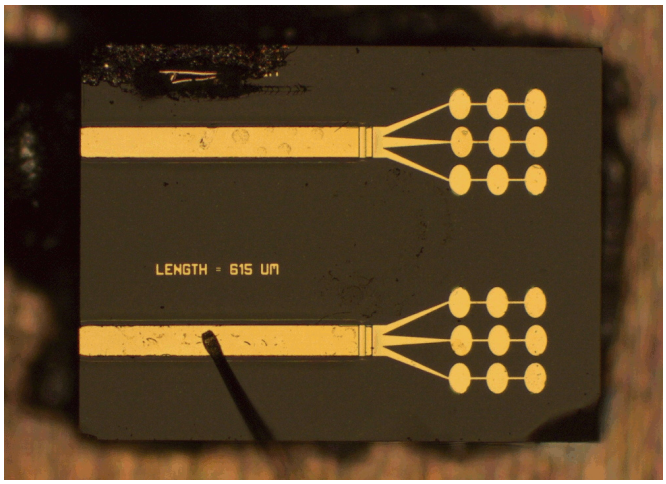

Figure 8.2.1.: QCLs 11 and 12. The chip is cleaved at the taper.

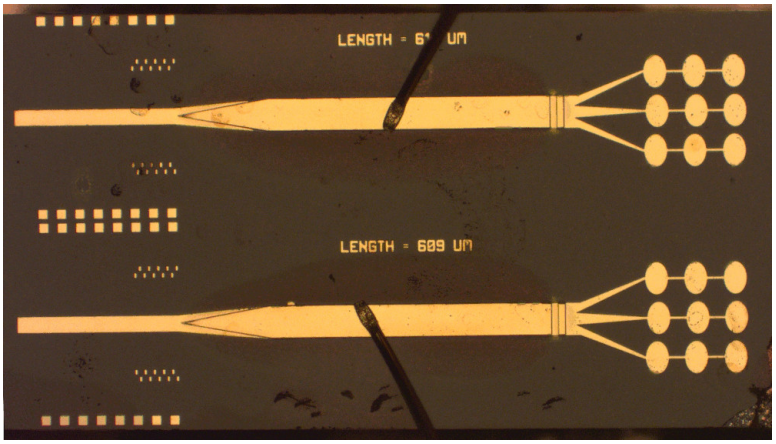

Figure 8.2.2.: QCLs 15 and 16.

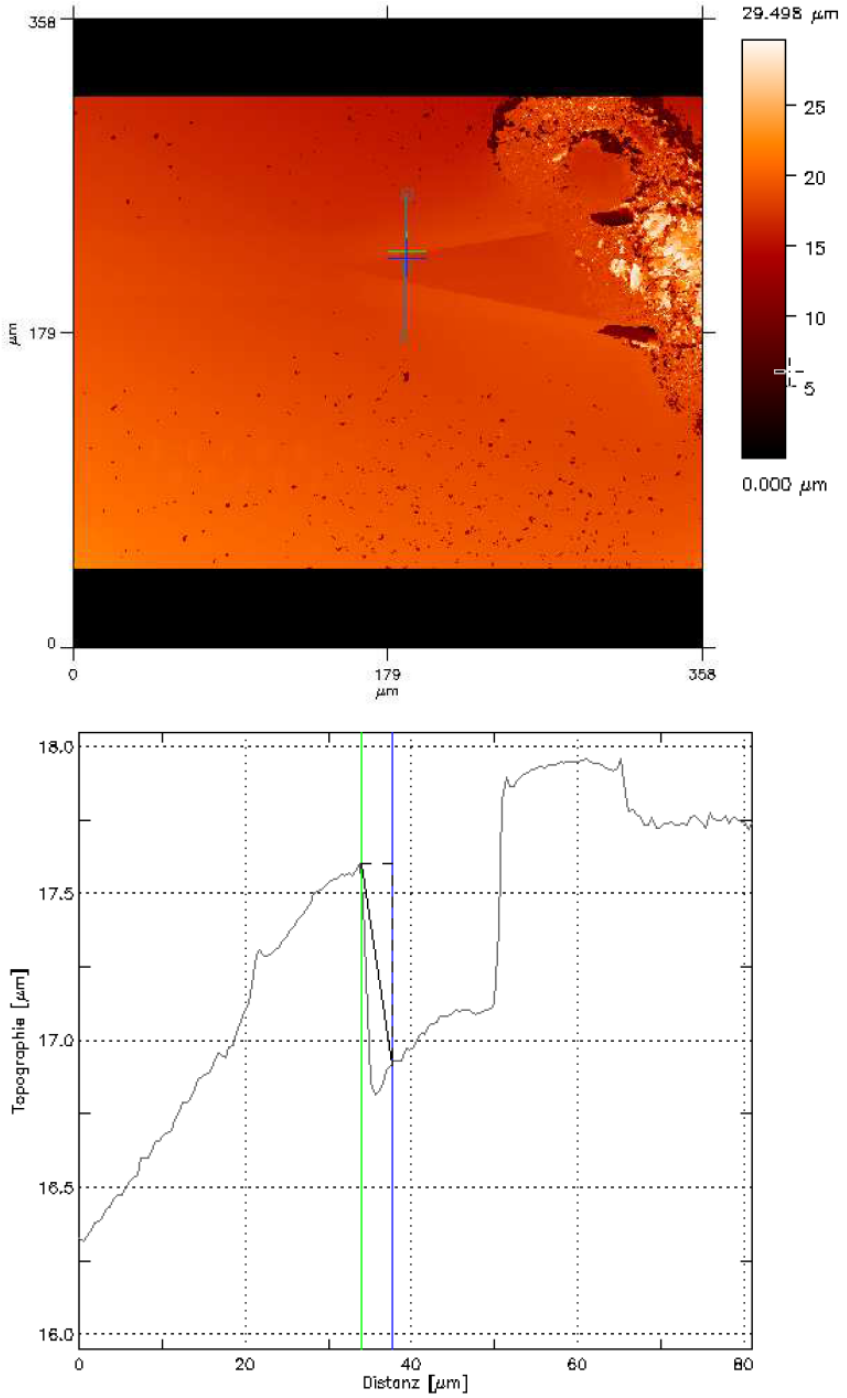

Figure 8.2.3.: White light interferometry imaging of the taper and tuning section of QCL 13. Similar to Fig. 7.1.5 the elevation profile is plotted along the blue line. The step in the top metallization from GaAs to BCB layer has improved and is only ca. 0.5 µm now (and inverted). Artifacts on the right are caused by the bond wire.

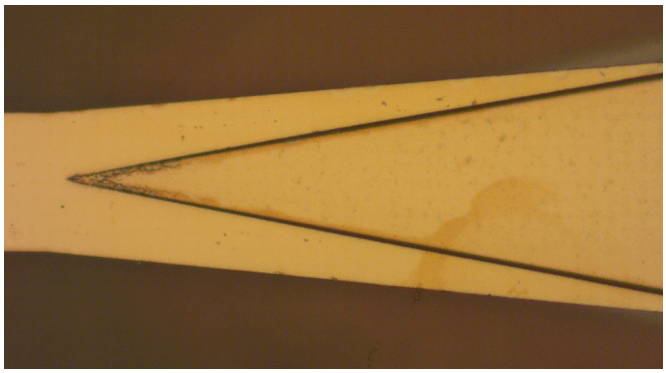

Figure 8.2.4.: Detail of the transition (QCL 13). The underlying GaAs triangle is gain visible through the gold layer, but the step is much less severe than in the first-generation devices. The surface appears substantially smoother.

8.3. Results - Original 2nd Generation Devices

QCLs 11 and 12 (Cleaved)

The cleaved devices QCL 11 and 12 became available at a point later in time than QCLs 13, 14, 15 and 16. Nevertheless, they are presented here first to keep consistency with previous chapters. Characterization is again based on IVL curves, spectra and far field measurements.

Initial output power and voltage measurements for QCL 11 and 12 are consistent with expectations for devices fabricated from the known active material. Threshold current at 48 K is 155 A cm^{-2} and 167 A cm^{-2}, around 10% lower than the comparison value of the cleaved first generation devices. This can be attributed to lower losses due to improved metal surface quality and a better mode overlap resulting from better lithography mask alignment. Both lasers enter a changed modal regime at around 265 A cm^{-2} accompanied by a boost in optical power as the gain profile shifts towards higher frequencies. Both lasers reach luminosity maximum shortly before the critical current is reached. Interestingly the power does not drop step-like as seen before but appears to decay exponentially, the reason for which remains unclear.

Examination of the spectral data shows unexpected properties that raise concerns about the correct operation of both lasers as intended in the design. The first apparent problem is the irregular mode spacing that exists for both lasers but is most evident for QCL 12, see Fig. 8.3.4. This is hard to explain with normal longitudinal multi-moding for such a laser geometry and hints at a more complex modal distribution. When polarization is discriminated in the spectra by adding a standing wire grid in the beam path, this suspicion is corroborated further, as the spectral features are not observed uniformly in co- and cross-polarization.

The far field scans give the final confirmation of non-fundamental optical modes. Contrary to the calculated antenna lobe, no similarity to a Gaussian profile is found. Instead, the patterns are highly irregular and ca. one third of the optical power is in the wrong polarization. For comparison, the first-generation cleaved QCLs had more than 90% of power distributed to the expected polarization and the beam was highly Gaussian. Furthermore, it could be established that the origin of the radiation is not the antenna. For this, a 200 µm by 200 µm absorber (Tessellating TeraHertz RAM, Thomas Keating Ltd.) with a thickness of 100 µm was placed at several points directly on the laser. While the effect on measured optical power was minuscule for placement on the antenna, it was an order of magnitude higher when the absorber covered parts of the laser ridge. The absorptance of this thin platelet is not perfect; approximately 65% was measured with a pinhole aperture and a pyrodetector. Nevertheless, this

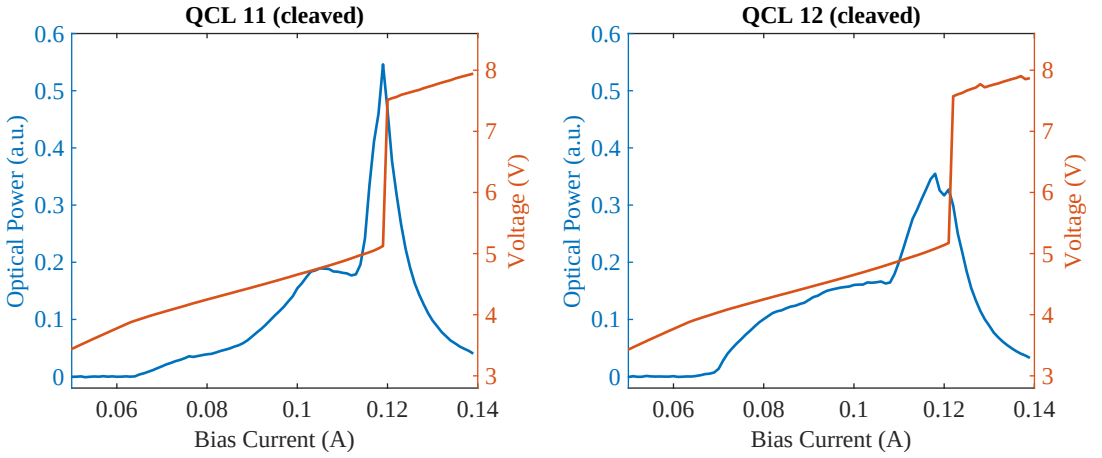

Figure 8.3.1.: IVL curves for QCL 11 and 12. Threshold current density is 155 A cm^{-2} and 167 A cm^{-2}.

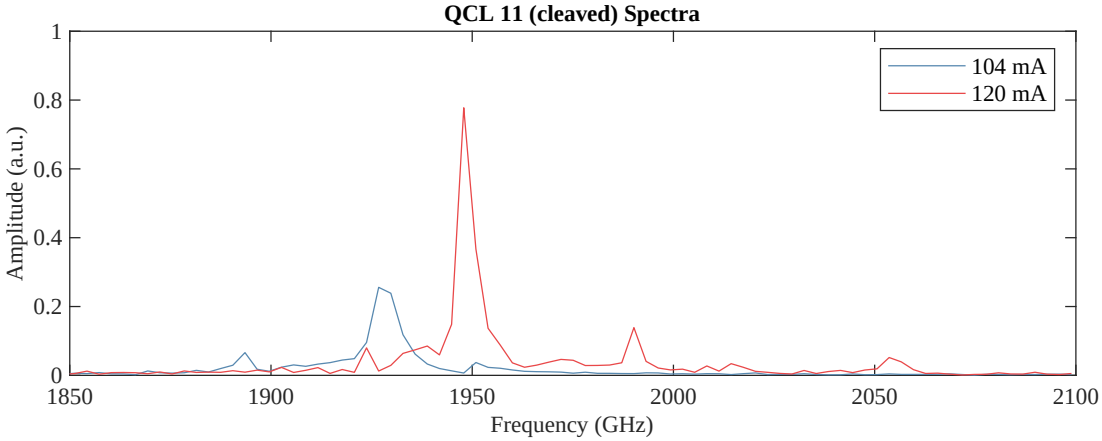

Figure 8.3.2.: QCL 11 spectra at 104 mA and 120 mA.

experiment confirms that very little - if any - fraction of the intra-cavity field couples to the fundamental q-TEM10 mode that would be radiated efficiently by the antenna.

It should be noted that the relative strength of the different modes seen in the spectra is unreliable as a result of the divergent and ill-shaped beams randomly radiated from the laser structures since it can be certainly assumed that not every oscillating mode creates the same pattern when radiated randomly from sub-wavelength structures. Some will necessarily couple better to the Gaussian optics of the Fourier transform spectrometer than others, depending on the exact distribution.

The occurrence of these problems already with the cleaved devices is a severe setback and gives little hope for a better outcome with the tunable devices.

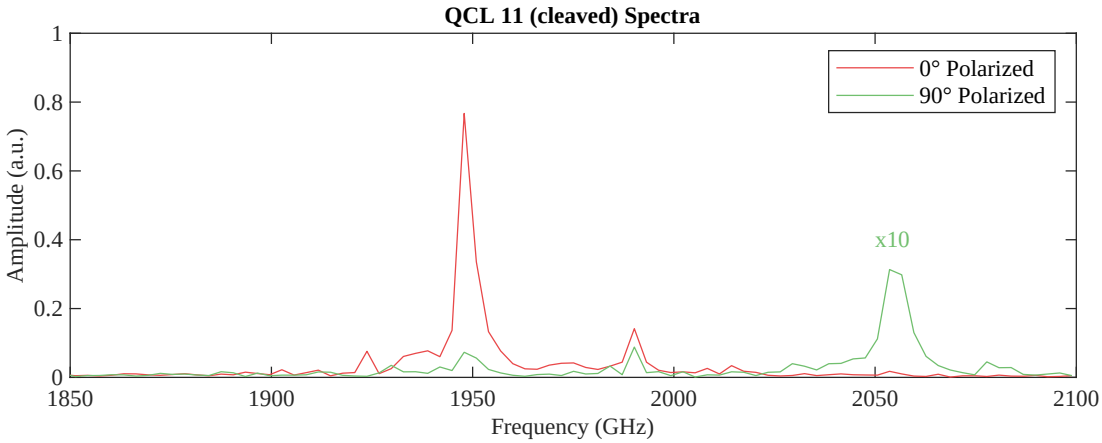

Figure 8.3.3.: QCL 11 spectra at 120 mA separated into beam polarizations of 0° and 90°. The unequal spectral power distribution suggests that more than one lateral mode is oscillating at the same time.

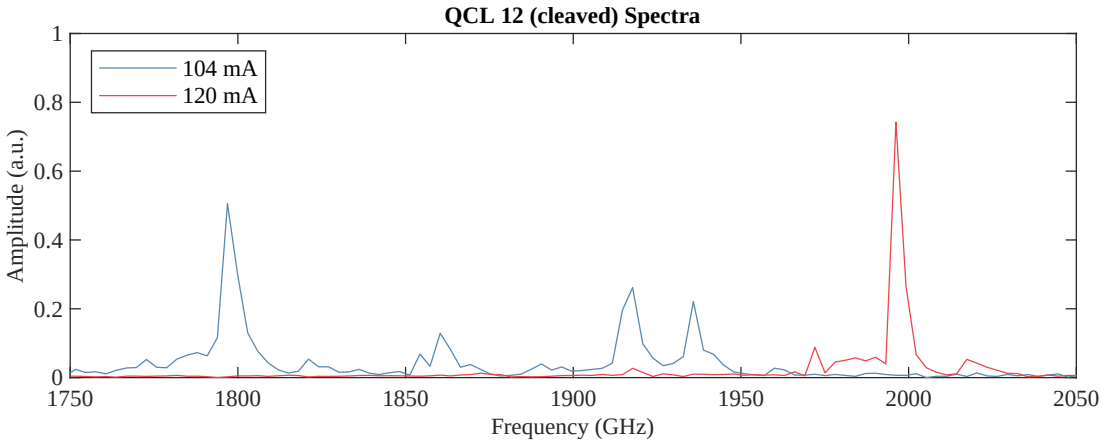

Figure 8.3.4.: QCL 12 spectra at 104 mA and 120 mA.

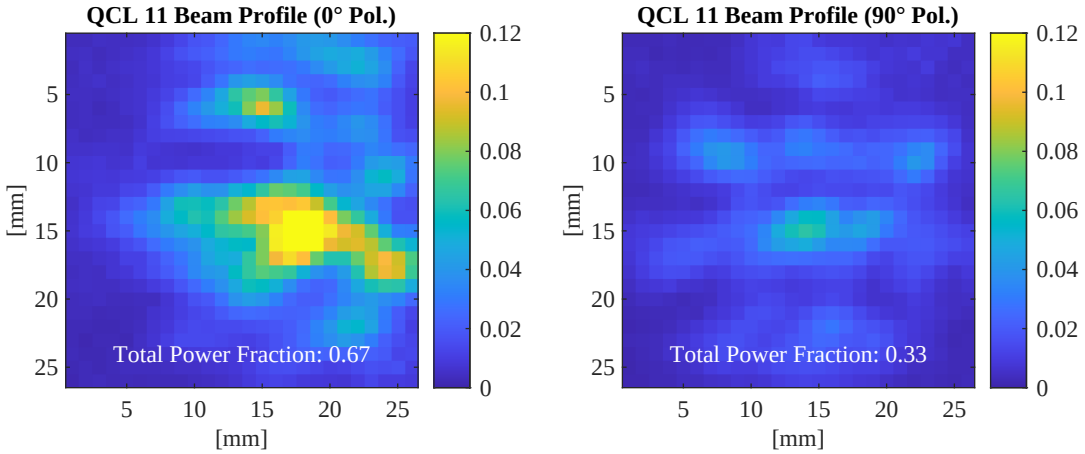

Figure 8.3.5.: QCL 11 far field measurement adds to the inconsistencies in the spectral data. A strong discrepancy from the expected gaussian beam is found, which can only be explained by major problems with the cavity mode.

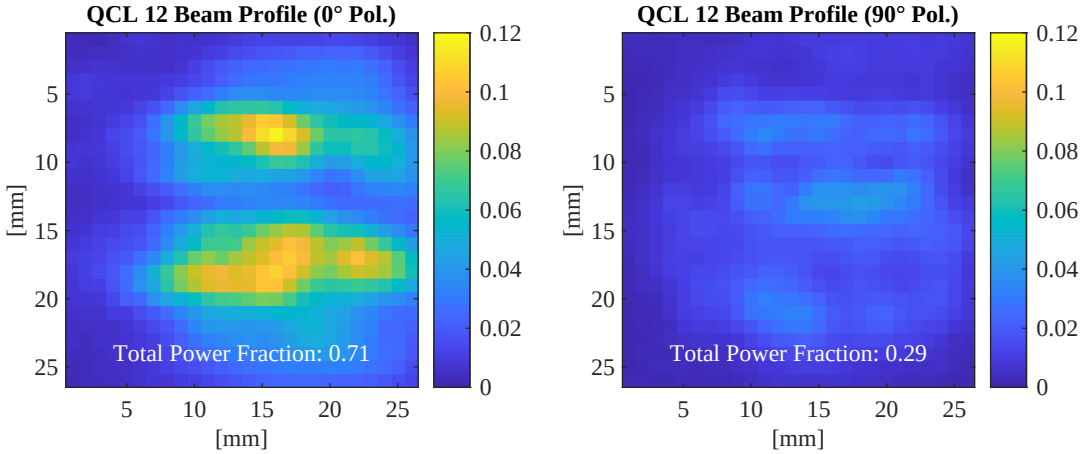

Figure 8.3.6.: QCL 12 far field. Similar irregularity already found in QCL 11 far field is also present here.

QCLs 13 to 16

The tunable QCLs 13 to 16 yield results similar to the cleaved lasers. The apparent mode problem is present equally for all devices, as evident from spectral measurements and beam patterns. Nevertheless, some tuning experiments were performed, which confirmed that the intended tuning mechanism generally does not work in the sense that no continuous tuning is possible. A modulation of relative mode intensity and, occasionally, a mode jump could be induced by the reflector movement. An interesting observation can be made in the spectra: A striking lack of any spectrally resolved current tuning. This is surprising and stands in contrast to the approximate value of $250\,\mathrm{MHz\,mA^{-1}}$ measured for the 1st generation devices in an otherwise similar setup. One possible interpretation of this result is a reduced overlap of the cavity mode with the active material of the laser.

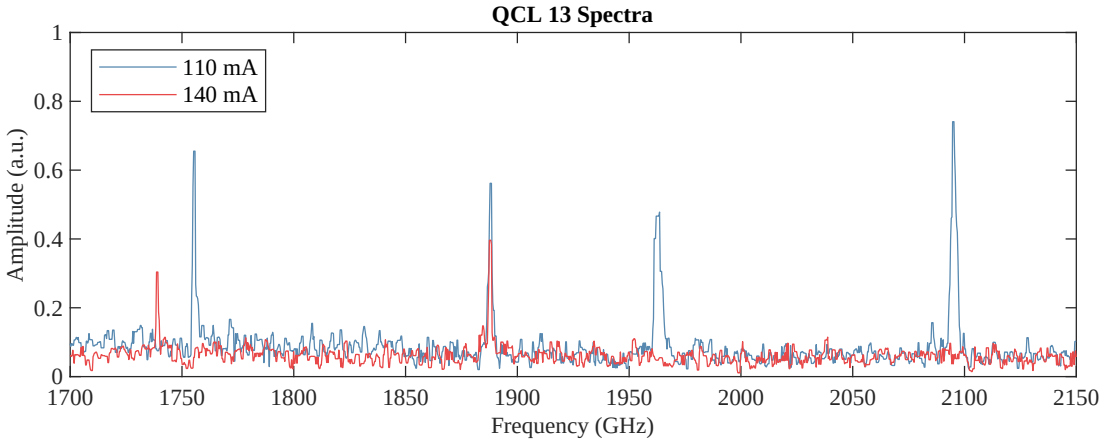

Figure 8.3.7.: QCL 13 Spectra measured without reflector membrane at 110 mA and 140 mA. Two findings are noticeable here: The frequency jump from 1740 GHz to 1755 GHz that is impossible with a longitudinal mode jump, and the unresolved current tuning seen at 1840 GHz.

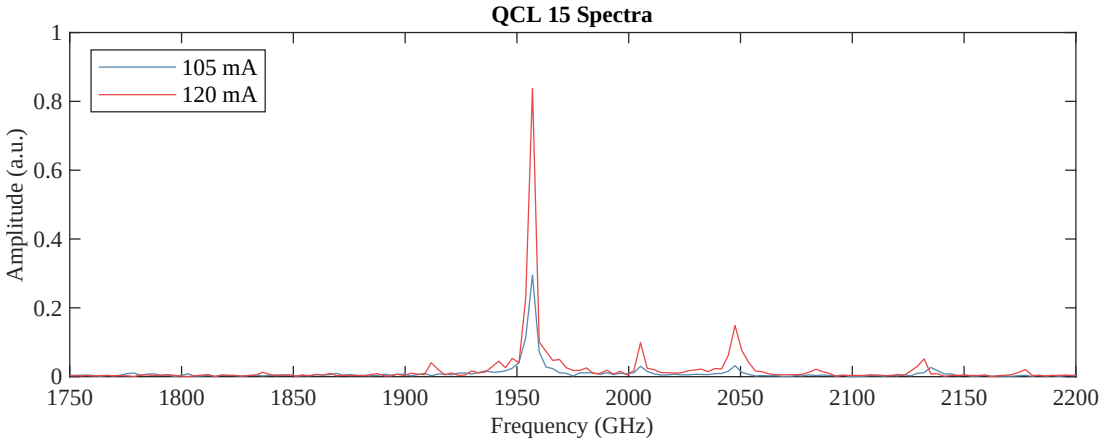

Figure 8.3.8.: QCL 15 spectra again show no signs of current tuning.

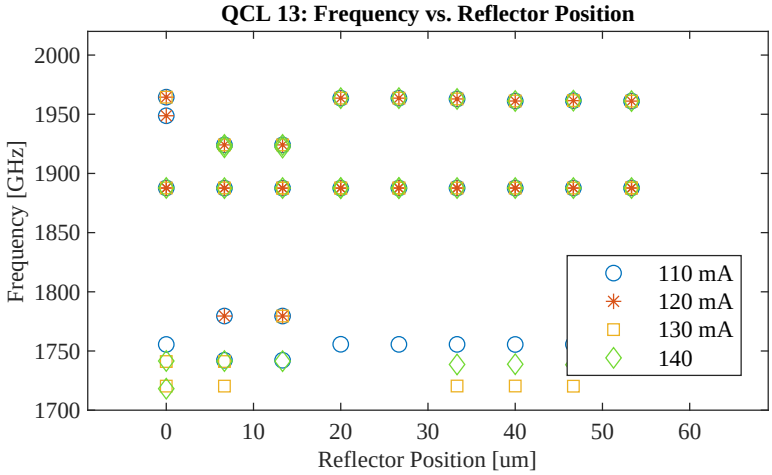

Figure 8.3.9.: QCL 13 tuning experiment revealing minimal effect on the spectrum with no continuous tuning detectable.

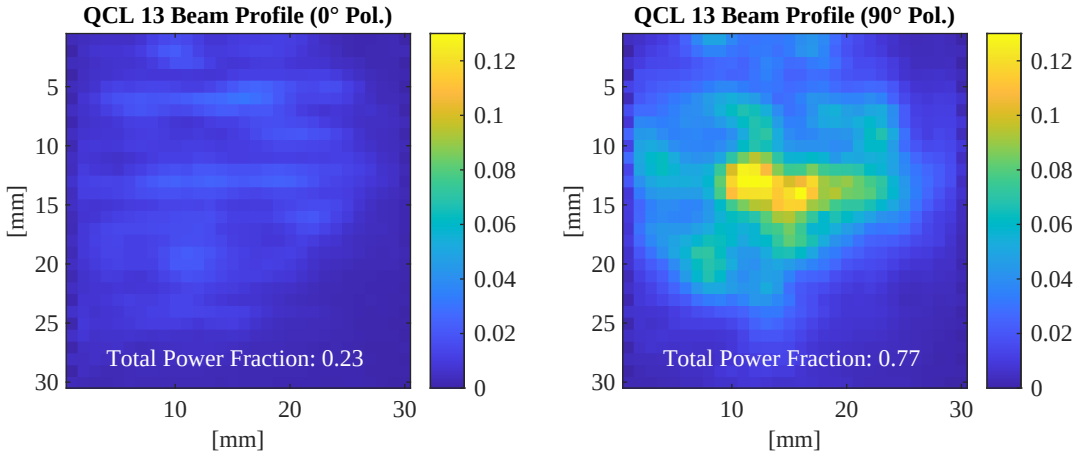

Figure 8.3.10.: QCL 13 far field.

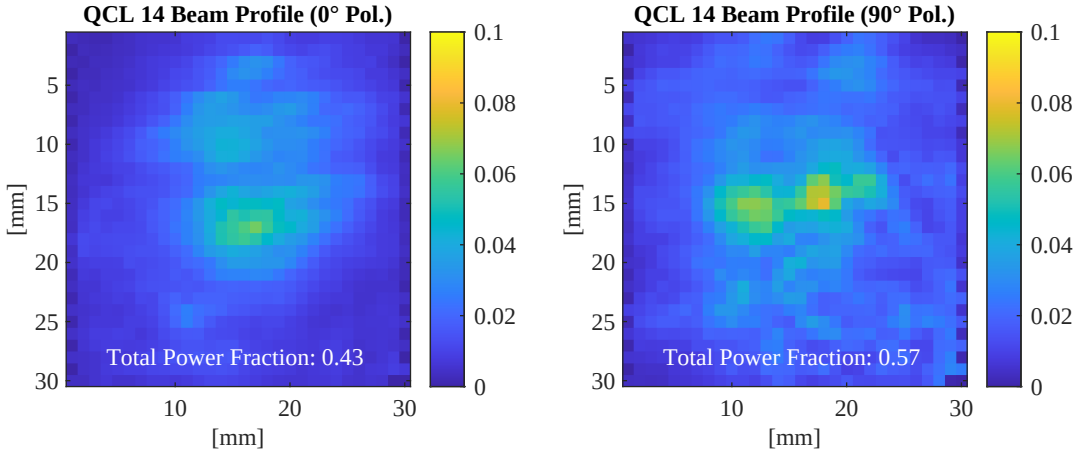

Figure 8.3.11.: QCL 14 far field.

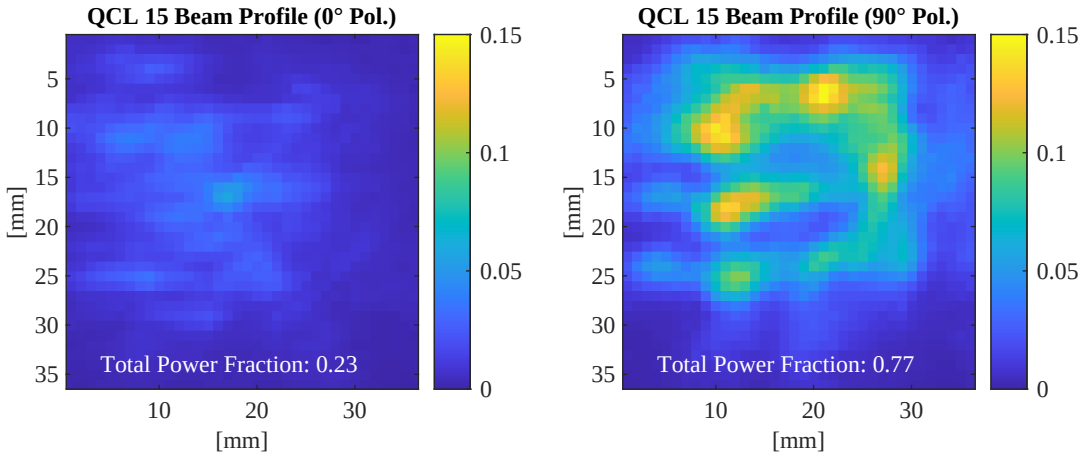

Figure 8.3.12.: QCL 15 far field.

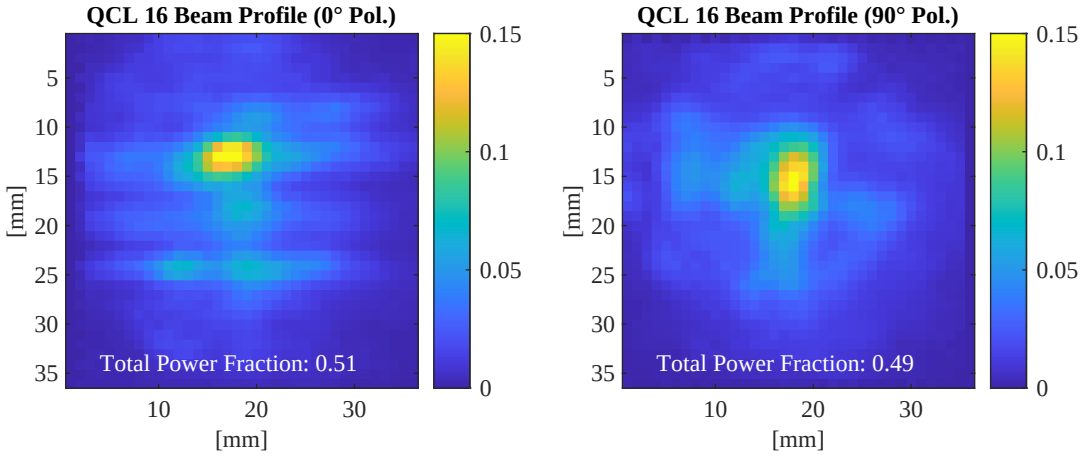

Figure 8.3.13.: QCL 16 far field.

Naturally, the question arises how this can be explained in terms of the possible laser cavity modes. With the current ridge width and thickness, four different quasi-TEM microstrip modes are propagated (see Fig. 8.3.14). QCLs 13 to 16 were the first devices that became available from the new manufacturing run for testing, and lacking the data from the cleaved lasers that confirms a similar behavior with these it was intuitive to turn the attention to the transition and tuning section first. It turns out that indeed the asymmetric mode labeled q-TEM40 in Fig. 8.3.14 is strongly reflected from the transition. This makes sense, because it is the highest order mode still propagated at 1.9 THz in the laser ridge, but since the tuning strip is narrower by a factor of two (and the BCB's dielectric constant lower) this mode falls below its cut-off frequency in this part. At some point on the transition section the wave must therefore be reflected back into the ridge. Since q-TEM40 is asymmetric, the high power fraction in the "wrong" polarization would be explicable. The fact that the same issue is found in the cleaved lasers casts doubt on the validity of this explanation - at least the higher order mode reflectivity of the transition can not be the sole explanation. Unfortunately, the root cause remains cryptic. It seems unlikely that oscillation could occur on any mode other than those of the ridge waveguide, but the unpredictable and disparate emission profiles call that assumption into question. In fact, on close examination of the emission spectra one more detail hardly fits to intra-waveguide TEM-modes: the lack of any resolved current tuning. This is a sign that a major part of the modal volume does not overlap with the active material and is not subject to the tuning mechanisms induced by current changes. Surface waves in the BCB could form resonances, but it is questionable if they could have q-factors high enough to compete with the waveguide modes.

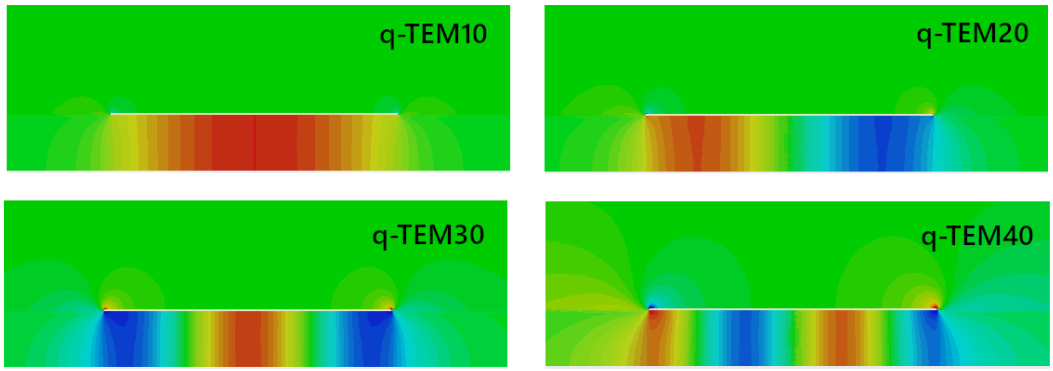

Figure 8.3.14.: Lateral modes supported by the laser ridge. Lasing of higher-order modes is one possible cause for the irregular spectra and ill-shaped beam patterns observed.

8.4. Results - FIB Etched 2nd Generation Devices

Assuming that the issues found so far indeed originate from higher-order lateral modes within the waveguide, there is a way to reduce the QCL's apparent tendency to oscillate on those modes. A reduction in the width of the ridge from 70 µm to 50 µm ensures that the suspected q-TEM40 mode can not be propagated within the waveguide anymore. For this, it is enough to reduce the top metal width without touching the GaAs ridge since the electric field is primarily confined by the metal structures and is only weakly guided by the dielectrics. This is possible with a Focused Ion Beam etching process and was carried out at ETH Zürich for a total of 8 lasers. The result of the process is shown in Fig. 8.4.1 and 8.4.2.

The following measurements reveal that, unfortunately, the FIB treatment did not yield the desired outcome. The spectra and far fields are still unpredictable, and tuning experiments are unsuccessful. It is worth noting that tuning does not work on any of the modes seen in the spectra. That means that the fundamental waveguide mode is either not excited at all or too weak to be detected with the noisy room temperature spectrometer system.

In conclusion, it has to be acknowledged that the second generation of tunable QCLs does not meet the expectations. Within the scope of this work, it could not be determined what the cause of the observed phenomena is. Although the lasers undisputedly do not oscillate on the intended waveguide mode, the measurements do not allow a definitive statement about the nature of the lasing mode, and EM field simulations could not be made consistent with them.

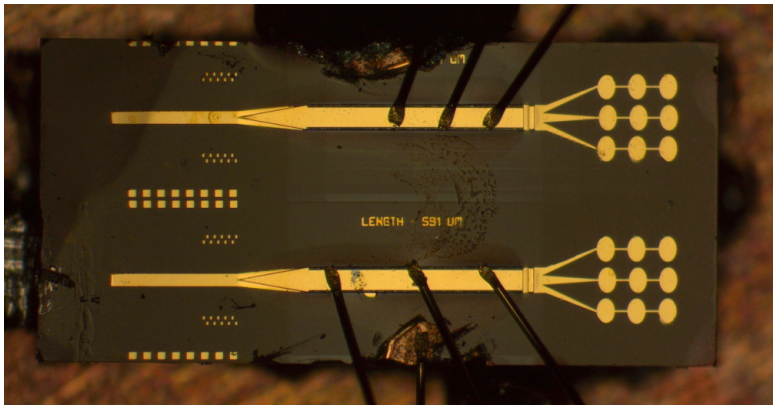

Figure 8.4.1.: QCL 21 and 22. These devices have been modified by Focussed Ion Beam etching to narrow the top metalization of the laser ridge in an attempt to inhibit higher lateral modes.

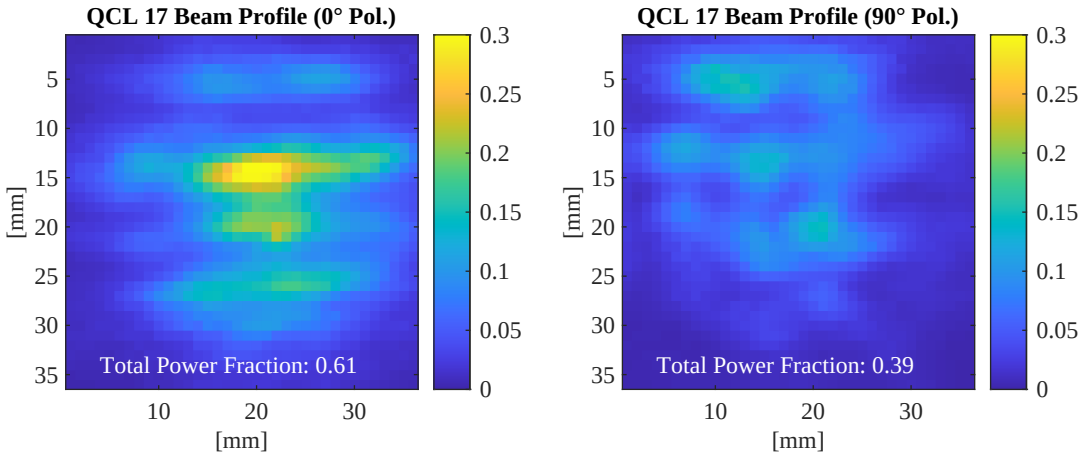

Figure 8.4.4.: QCL 17 far field. The FIB modification of the laser ridge did not suppress irregular modes; the far field pattern is still similar to the original 2nd generation lasers.

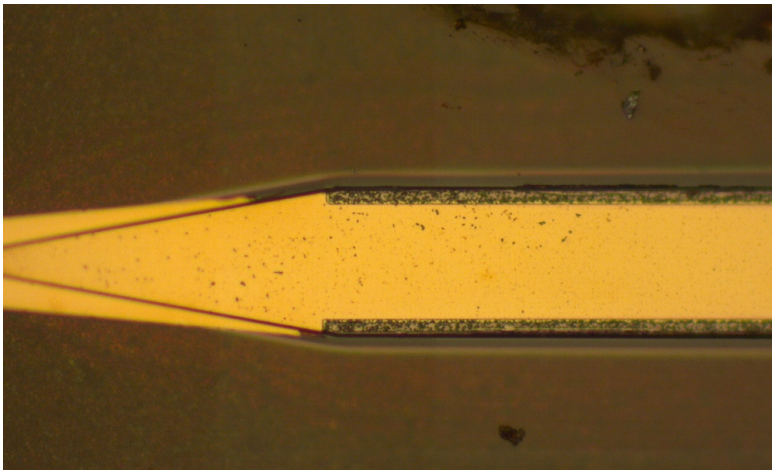

Figure 8.4.2.: Detail of the FIB etching on QCL 22.

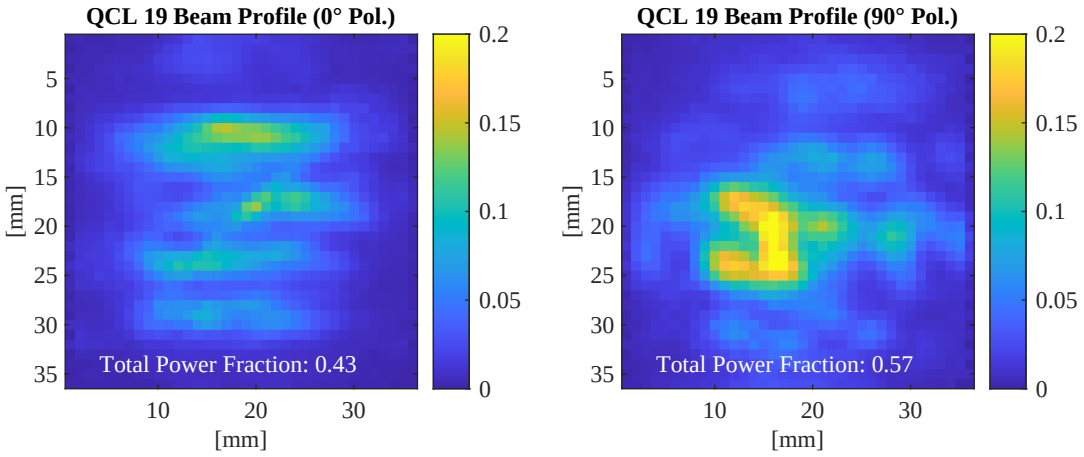

Figure 8.4.5.: QCL 19 far field.

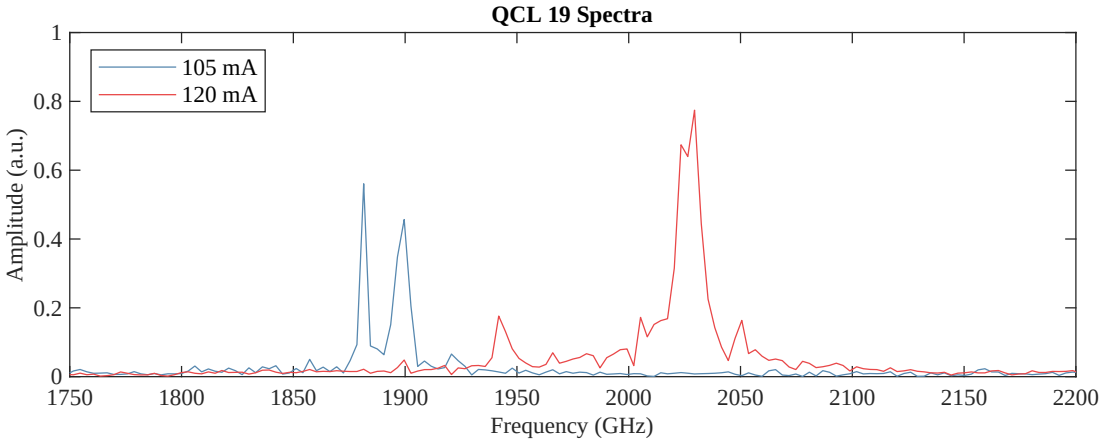

Figure 8.4.3.: Spectra of QCL 19 at 105 mA and 120 mA. The observed FSRs do not correspond to the expected fundamental longitudinal modes.

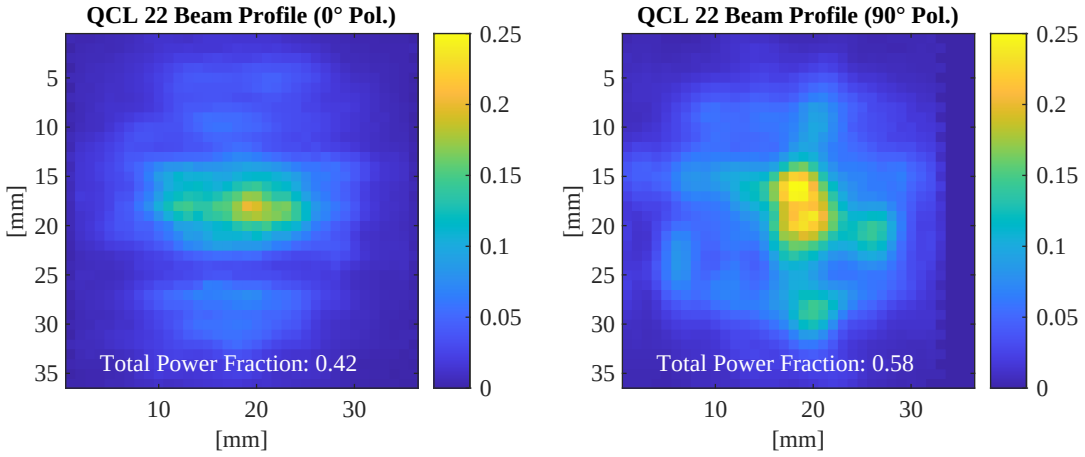

Figure 8.4.6.: QCL 22 far field.

Chapter 9.

Conclusion and Outlook

In the course of this thesis, a novel approach to frequency tuning of terahertz quantum cascade lasers was investigated using direct electric field manipulation with mechanical methods on a chip scale. For that purpose, devices were designed with the intent to produce an extended stray field outside the waveguide. It is hypothesized that the coupling of this stray field to a movable reflector is strong enough to dominate the laser feedback and define the frequency of the laser mode.

By using the commercially available field solver CST Microwave Studio it was shown that the principle idea performs well within the limitations of computer simulation and solutions were found that enable a robust tuning scheme using standard lithography for manufacturing lasers with the desired properties. Extended iterative simulation steps were carried out to verify the design ideas and optimize all structures with respect to electromagnetic performance, manufacturability and robustness against process tolerances.

The manufacturing was done in cooperation with the quantum optics workgroup of J. Faist at ETH Zürich. The BCB planarization step developed in this workgroup is a crucial component of the tunable QCL design and has been used successfully as a basis for earlier antenna-coupled THz QCLs. It could be established with this work that the material is resilient enough to be applied in mechanically demanding environments such as a moving silicon membrane in physical contact. It was shown that with precise control of process parameters, it is possible to control the planarization process to a degree that allows the construction of continuous metal films stretching over GaAs-BCB boundaries, allowing low reflection impedance-matching between GaAs-based and BCB-based waveguides.

From an experimental point of view, the tunable setup, especially the reflector alignment, was possible with a relatively simple positioning and monitoring system with sufficient precision. The results from the first-generation lasers demonstrate a

working tuning mechanism, with the observed frequency shift on reflector movement often agreeing with values expected from simulations. However, overall performance and tuning efficiency vary between individual lasers. The possibility of stray field manipulation to create a cavity boundary is verified in this way also experimentally. The best result was coincidentally achieved with QCL 3, the first tuning experiment done during this work. Frustratingly, the good tuning performance from this laser could not be matched or surpassed in subsequent efforts. Deviations from the simulations include non-uniform tuning that can be understood if a higher reflectance than expected between laser ridge and tuning section is assumed. In this case, an analytical model independent of the microscopic cause of this intracavity reflection gives results that replicate the observed behavior. This particularly stresses the importance of manufacturing precision in this part since already comparatively small intracavity reflections carry significant repercussions.

Two main areas for improvement had emerged at this point: The impedance matching between sections had to be improved to minimize the above reflections, and most first-generation lasers emit in a multimode spectrum that is unsuitable for application as a local oscillator. Both points were addressed with a second manufacturing run that entailed shorter resonators to promote single-mode operation and improved lithography and surface quality. In an unwelcome turn of events, these changes lead to the formation of higher-order modes. The apparently random manifestation in spectra and beam shapes prevents a clear attribution to a specific cause. No common pattern could be found despite the characterization of 14 different devices from this batch, leaving the question of where precisely the laser resonance is formed and which modes are active. In hindsight, it would have been advisable also to produce a small number of 1.0 mm or 1.5 mm lasers as well to decouple the effects of changed length and improved process in the comparison to the older devices.

This thesis had to cope with many difficulties and unexpected outcomes. This is especially true for the second generation of tunable QCLs, which became possible only after completion of planned work on the MBE facilities at ETH Zürich and was then delayed due to the ramifications of the Covid-19 pandemic. To make matters worse, they contributed far less to the further development of this tuning approach than was anticipated. But, for all that, important insights into the challenges raised by mechanically tunable THz QCLs were gained. For at least some of the presented devices, it could be shown that the idea of using two-dimensional Bragg reflectors on silicon membranes can be used successfully to implement an on-chip tuning mechanism by coupling to the stray field of a BCB substrate microstrip. A publication on the first-generation lasers is in preparation, where at least one laser performed close to

expectations and a conclusive analysis was possible.

Future work that did not make its way into this thesis will focus on three things. First and foremost, the origin of the irregular mode present in the second generation of QCLs has to be investigated further. Reverting to original dimensions of more than 1 mm at least for a number of test devices is a first step, as well as decreasing ridge width to about 50 µm. Secondly, the disruptive reflections at the GaAs-BCB transition section must be reduced. There is a good chance that the improved manufacturing process used for the second-generation lasers already solves this issue. This will be known once lasing on the fundamental qTEM mode is re-established. If the reflections are still too high, it might be possible to construct the tuning section without the transition to BCB. Simulations indicate a strong enough stray field can be produced by tapering the ridge top metallization to a thin stripe, approximately 5 µm in width. Here a similar membrane reflector with an optimized design can terminate the cavity similar to the design investigated in this work. A disadvantage is increased sensitivity to misalignment. Finally, single-mode operation needs to be worked on. Since shortening the laser ridges led to the discussed mode problems, it could be suitable to try instead to control the stark shift of the gain profile and the losses independently, as could be done by electrically splitting the top contact and individually biasing both sections. In fact, devices with this feature were manufactured as part of the second generation but could not be evaluated for the same reason as the rest. Alternatively, a DFB structure to limit the laser spectrum to a single mode without the ability to select a mode through Stark shift could be an initial step in this regard.

Chapter 10.

References

Bibliography

[1] Marc Mertens. "Characterization of 4.7 THz Quantum Cascade Lasers for the upGREAT Local Oscillator". MA thesis. University of Cologne, 2017.

[2] Keita Ohtani, Dana Turčinková, Christopher Bonzon, Ileana-Cristina Benea-Chelmus, Mattias Beck, Jérôme Faist, Matthias Justen, Urs U Graf, Marc Mertens, and Jürgen Stutzki. "High performance 4.7 THz GaAs quantum cascade lasers based on four quantum wells". In: *New Journal of Physics* 18.12 (Dec. 2016), p. 123004. DOI: 10.1088/1367-2630/18/12/123004.

[3] C. Risacher, R. Güsten, J. Stutzki, H.-W. Hübers, R. Aladro, A. Bell, C. Buchbender, D. Büchel, T. Csengeri, C. Duran, U. U. Graf, R. D. Higgins, C. E. Honingh, K. Jacobs, M. Justen, B. Klein, M. Mertens, Y. Okada, A. Parikka, P. Pütz, N. Reyes, H. Richter, O. Ricken, D. Riquelme, N. Rothbart, N. Schneider, R. Simon, M. Wienold, H. Wiesemeyer, M. Ziebart, P. Fusco, S. Rosner, and B. Wohler. "The upGREAT Dual Frequency Heterodyne Arrays for SOFIA". In: *Journal of Astronomical Instrumentation* 07.04 (Dec. 2018), p. 1840014. DOI: 10.1142/s2251171718400147.

[4] Yoko Okada, Ronan Higgins, Volker Ossenkopf-Okada, Cristian Guevara, Juergen Stutzki, and Marc Mertens. "First detection of [13C II] in the Large Magellanic Cloud". In: *Astronomy & Astrophysics* 631 (Nov. 2019), p. L12. DOI: 10.1051/0004-6361/201936685.

[5] N. Schneider, R. Simon, C. Guevara, C. Buchbender, R. D. Higgins, Y. Okada, J. Stutzki, R. Güsten, L. D. Anderson, J. Bally, H. Beuther, L. Bonne, S. Bontemps, E. Chambers, T. Csengeri, U. U. Graf, A. Gusdorf, K. Jacobs, M. Justen, S. Kabanovic, R. Karim, M. Luisi, K. Menten, M. Mertens, B. Mookerjea, V. Ossenkopf-Okada, C. Pabst, M. W. Pound, H. Richter, N. Reyes, O. Ricken, M. Röllig, D. Russeil, Á. Sánchez-Monge, G. Sandell, M. Tiwari, H. Wiesemeyer, M. Wolfire, F. Wyrowski, A. Zavagno, and A. G. G. M. Tielens. "FEEDBACK: a SOFIA Legacy Program to Study Stellar Feedback in Regions of Massive Star Formation". In: *Publications of the Astronomical Society of the Pacific* 132.1016 (Sept. 2020), p. 104301. DOI: 10.1088/1538-3873/aba840.

[6] B. Mookerjea, G. Sandell, V. S. Veena, R. Guesten, D. Riquelme, H. Wiesemeyer, F. Wyrowski, and M. Mertens. "Distribution of ionized, atomic, and PDR gas around S 1 in ρ Ophiuchus". In: *Astronomy & Astrophysics* 648 (Apr. 2021), A40. DOI: 10.1051/0004-6361/202040217.

[7] R. Higgins, S. Kabanovic, C. Pabst, D. Teyssier, J. R. Goicoechea, O. Berne, E. Chambers, M. Wolfire, S. T. Suri, C. Buchbender, Y. Okada, M. Mertens, A. Parikka, R. Aladro, H. Richter, R. Guesten, J. Stutzki, and A. G. G. M. Tielens. "Observation and calibration strategies for large-scale multi-beam velocity-resolved mapping of the [CII] emission in the Orion molecular cloud". In: *Astronomy & Astrophysics* 652 (Aug. 2021), A77. DOI: 10.1051/0004-6361/202039621.

[8] M. Tiwari, M. Wolfire, M. W. Pound, E. Tarantino, R. Karim, L. Bonne, C. Buchbender, R. Güsten, C. Guevara, S. Kabanovic, Ü. Kavak, M. Mertens, N. Schneider, R. Simon, J. Stutzki, and A. G. G. M. Tielens. "SOFIA FEEDBACK Survey: PDR Diagnostics of Stellar Feedback in Different Regions of RCW 49". In: *The Astronomical Journal* 164.4 (Sept. 2022), p. 150. DOI: 10.3847/1538-3881/ac8a44.

[9] S. Kabanovic, N. Schneider, V. Ossenkopf-Okada, F. Falasca, R. Güsten, J. Stutzki, R. Simon, C. Buchbender, L. Anderson, L. Bonne, C. Guevara, R. Higgins, B. Koribalski, M. Luisi, M. Mertens, Y. Okada, M. Roellig, D. Seifried, M. Tiwari, F. Wyrowski, A. Zavagno, and A. G. G. M. Tielens. "Self-absorption in [C II], 12CO, and H I in RCW120". In: *Astronomy and Astrophysics* 659 (Mar. 2022), A36. DOI: 10.1051/0004-6361/202142575.

[10] Nicola Schneider, Lars Bonne, Sylvain Bontemps, Slawa Kabanovic, Robert Simon, Volker Ossenkopf-Okada, Christof Buchbender, Juergen Stutzki, Marc Mertens, Oliver Ricken, Timea Csengeri, and Alexander G.G.M. Tielens. "Ionized Carbon Tracing the Assembly of Interstellar Clouds". In: *Nature Astronomy (Accepted for Publication)* (2023). DOI: 10.21203/rs.3.rs-2060493/v1.

[11] Keisuke Shinohara, Dean C Regan, Yan Tang, Andrea L Corrion, David F Brown, Joel C Wong, John F Robinson, Helen H Fung, Adele Schmitz, Thomas C Oh, et al. "Scaling of GaN HEMTs and Schottky diodes for submillimeter-wave MMIC applications". In: *IEEE Transactions on Electron Devices* 60.10 (2013), pp. 2982–2996.

[12] Masayoshi Tonouchi. "Cutting-edge terahertz technology". In: *Nature photonics* 1.2 (2007), p. 97.

[13] Stephan Schlemmer, Thomas Giesen, Frank Lewen, and Gisbert Winnewisser. "High-Resolution Laboratory Terahertz Spectroscopy and Applications to Astrophysics". In: *Frontiers of Molecular Spectroscopy*. Elsevier, 2009, pp. 241–265. DOI: 10.1016/b978-0-444-53175-9.00008-8.

[14] Kei Takeya and Kodo Kawase. "Research on Hydrogen-Bonded Materials Using Terahertz Technology". In: *Terahertz Spectroscopy - A Cutting Edge Technology*. InTech, Mar. 2017. DOI: 10.5772/67640.

[15] Zhengping Fu and Masashi Yamaguchi. "Coherent excitation of optical phonons in GaAs by broadband terahertz pulses". In: *Scientific reports* 6 (2016), p. 38264.

[16] PT Greenland, Stephen Anthony Lynch, AFG Van der Meer, BN Murdin, CR Pidgeon, B Redlich, NQ Vinh, and G Aeppli. "Coherent control of Rydberg states in silicon". In: *Nature* 465.7301 (2010), pp. 1057–1061.

[17] Tobias Kampfrath, Alexander Sell, Gregor Klatt, Alexej Pashkin, Sebastian Mährlein, Thomas Dekorsy, Martin Wolf, Manfred Fiebig, Alfred Leitenstorfer, and Rupert Huber. "Coherent terahertz control of antiferromagnetic spin waves". In: *Nature Photonics* 5.1 (Nov. 2010), pp. 31–34. DOI: 10.1038/nphoton.2010.259.

[18] A. Pais. "Einstein and the quantum theory". In: *Reviews of Modern Physics* 51.4 (Oct. 1979), pp. 863–914. DOI: 10.1103/revmodphys.51.863.

[19] Heinrich Rubens. "Ueber Dispersion ultrarother Strahlen". In: *Annalen der Physik und Chemie* 281.2 (1892), pp. 238–261. DOI: 10.1002/andp.18922810204.

[20] A. Rogalski. "History of infrared detectors". In: *Opto-Electronics Review* 20.3 (Jan. 2012). DOI: 10.2478/s11772-012-0037-7.

[21] C. E. Cleeton and N. H. Williams. "Electromagnetic Waves of 1.1 cm Wave-Length and the Absorption Spectrum of Ammonia". In: *Physical Review* 45.4 (Feb. 1934), pp. 234–237. DOI: 10.1103/physrev.45.234.

[22] J. A. Klein, J. H. N. Loubser, A. H. Nethercot, and C. H. Townes. "Magnetron Harmonics at Millimeter Wavelengths". In: *Review of Scientific Instruments* 23.2 (Feb. 1952), pp. 78–82. DOI: 10.1063/1.1746183.

[23] Pierre Connes. "Early history of fourier transform spectroscopy". In: *Infrared Physics* 24.2-3 (May 1984), pp. 69–93. DOI: 10.1016/0020-0891(84)90052-6.

[24] James W. Cooley and John W. Tukey. "An algorithm for the machine calculation of complex Fourier series". In: *Mathematics of Computation* 19.90 (1965), pp. 297–301. DOI: 10.1090/s0025-5718-1965-0178586-1.

[25] J. R. Pierce. “Traveling-Wave Tubes”. In: *Bell System Technical Journal* 29.1 (Jan. 1950), pp. 1–59. DOI: 10.1002/j.1538-7305.1950.tb00932.x.

[26] H. Johnson. “Backward-Wave Oscillators”. In: *Proceedings of the IRE* 43.6 (1955), pp. 684–697. DOI: 10.1109/jrproc.1955.278054.

[27] Gregory S. Nusinovich, Manfred K. A. Thumm, and Michael I. Petelin. “The Gyrotron at 50: Historical Overview”. In: *Journal of Infrared, Millimeter, and Terahertz Waves* 35.4 (Feb. 2014), pp. 325–381. DOI: 10.1007/s10762-014-0050-7.

[28] A. CROCKER, H. A. GEBBIE, M. F. KIMMITT, and L. E. S. MATHIAS. “Stimulated Emission in the Far Infra-Red”. In: *Nature* 201.4916 (Jan. 1964), pp. 250–251. DOI: 10.1038/201250a0.

[29] G Dodel. “On the history of far-infrared (FIR) gas lasers: Thirty-five years of research and application”. In: *Infrared Physics & Technology* 40.3 (June 1999), pp. 127–139. DOI: 10.1016/s1350-4495(99)00005-5.

[30] W. J. Witteman and R. Bleekrode. “Pulsed and continuous molecular far infrared gaslaser”. In: *Zeitschrift für angewandte Mathematik und Physik ZAMP* 16.1 (Jan. 1965), pp. 87–88. DOI: 10.1007/bf01589060.

[31] L. Esaki and R. Tsu. “Superlattice and Negative Differential Conductivity in Semiconductors”. In: *IBM Journal of Research and Development* 14.1 (Jan. 1970), pp. 61–65. DOI: 10.1147/rd.141.0061.

[32] RF Kazarinov and R.A. Suris. “Possible amplification of electromagnetic waves in a semiconductor with a superlattice”. In: *Soviet Physycs. Semiconductors* 5 (Oct. 1971), pp. 707–709.

[33] Raymond Dingle. “Confined carrier quantum states in ultrathin semiconductor heterostructures”. In: *Advances in Solid State Physics*. Springer Berlin Heidelberg, pp. 21–48. DOI: 10.1007/bfb0107373.

[34] J. P. van der Ziel, R. Dingle, R. C. Miller, W. Wiegmann, and W. A. Nordland. “Laser oscillation from quantum states in very thin GaAs-Al0.2Ga0.8As multilayer structures”. In: *Applied Physics Letters* 26.8 (Apr. 1975), pp. 463–465. DOI: 10.1063/1.88211.

[35] G_ Bastard. “Superlattice band structure in the envelope-function approximation”. In: *Physical Review B* 24.10 (1981), p. 5693.

[36] Tsuneya Ando, Alan B. Fowler, and Frank Stern. “Electronic properties of two-dimensional systems”. In: *Reviews of Modern Physics* 54.2 (Apr. 1982), pp. 437–672. DOI: 10.1103/revmodphys.54.437.

[37] L. C. West and S. J. Eglash. "First observation of an extremely large-dipole infrared transition within the conduction band of a GaAs quantum well". In: *Applied Physics Letters* 46.12 (June 1985), pp. 1156–1158. DOI: 10.1063/1.95742.

[38] M. Helm, P. England, E. Colas, F. DeRosa, and S. J. Allen. "Intersubband emission from semiconductor superlattices excited by sequential resonant tunneling". In: *Physical Review Letters* 63.1 (July 1989), pp. 74–77. DOI: 10.1103/physrevlett.63.74.

[39] J. Faist, F. Capasso, D. L. Sivco, C. Sirtori, A. L. Hutchinson, and A. Y. Cho. "Quantum Cascade Laser". In: *Science* 264.5158 (Apr. 1994), pp. 553–556. DOI: 10.1126/science.264.5158.553.

[40] J. Faist, F. Capasso, C. Sirtori, D.L. Sivco, A.L. Hutchinson, and A.Y. Cho. "Room temperature mid-infrared quantum cascade lasers". In: *Electronics Letters* 32.6 (1996), p. 560. DOI: 10.1049/el:19960395.

[41] Rüdeger Köhler, Alessandro Tredicucci, Fabio Beltram, Harvey E. Beere, Edmund H. Linfield, A. Giles Davies, David A. Ritchie, Rita C. Iotti, and Fausto Rossi. "Terahertz semiconductor-heterostructure laser". In: *Nature* 417.6885 (May 2002), pp. 156–159. DOI: 10.1038/417156a.

[42] Miriam Serena Vitiello, Giacomo Scalari, Benjamin Williams, and Paolo De Natale. "Quantum cascade lasers: 20 years of challenges". In: *Optics Express* 23.4 (Feb. 2015), p. 5167. DOI: 10.1364/oe.23.005167.

[43] Kazuue Fujita, Seungyong Jung, Yifan Jiang, Jae Hyun Kim, Atsushi Nakanishi, Akio Ito, Masahiro Hitaka, Tadataka Edamura, and Mikhail A. Belkin. "Recent progress in terahertz difference-frequency quantum cascade laser sources". In: *Nanophotonics* 7.11 (Sept. 2018), pp. 1795–1817. DOI: 10.1515/nanoph-2018-0093.

[44] H. R. Fetterman, B. J. Clifton, P. E. Tannenwald, and C. D. Parker. "Submillimeter detection and mixing using Schottky diodes". In: *Applied Physics Letters* 24.2 (Jan. 1974), pp. 70–72. DOI: 10.1063/1.1655098.

[45] G. J. Dolan, T. G. Phillips, and D. P. Woody. "Low-noise 115-GHz mixing in superconducting oxide-barrier tunnel junctions". In: *Applied Physics Letters* 34.5 (Mar. 1979), pp. 347–349. DOI: 10.1063/1.90783.

[46] T. Phillips, D. Woody, G. Dolan, R. Miller, and R. Linke. "Dayem-Martin (SIS tunnel junction) mixers for low noise heterodyne receivers". In: *IEEE Transactions on Magnetics* 17.1 (Jan. 1981), pp. 684–689. DOI: 10.1109/tmag.1981.1060994.

[47] Urs U. Graf, Cornelia E. Honingh, Karl Jacobs, and Jürgen Stutzki. "Terahertz Heterodyne Array Receivers for Astronomy". In: *Journal of Infrared, Millimeter, and Terahertz Waves* 36.10 (June 2015), pp. 896–921. DOI: 10.1007/s10762-015-0171-7.

[48] EM Gershenzon, GN Gol'tsman, IG Gogidze, YP Gusev, AI Elant'ev, BS Karasik, and AD Semenov. "Millimeter and submillimeter range mixer based on electronic heating of superconducting films in the resistive state". In: *Sov. Phys. Superconductivity* 3 (1990), p. 1582.

[49] R. W. Wilson, K. B. Jefferts, and A. A. Penzias. "Carbon Monoxide in the Orion Nebula". In: *The Astrophysical Journal* 161 (July 1970), p. L43. DOI: 10.1086/180567.

[50] T. G. Phillips and K. B. Jefferts. "A Low Temperature Bolometer Heterodyne Receiver for Millimeter Wave Astronomy". In: *Review of Scientific Instruments* 44.8 (Aug. 1973), pp. 1009–1014. DOI: 10.1063/1.1686288.

[51] F. J. Lovas, D. R. Johnson, and L. E. Snyder. "Recommended rest frequencies for observed interstellar molecular transitions". In: *The Astrophysical Journal Supplement Series* 41 (Nov. 1979), p. 451. DOI: 10.1086/190626.

[52] E.C. Sutton. "A Superconducting Tunnel Junction Receiver for 230 GHz". In: *IEEE Transactions on Microwave Theory and Techniques* 31.7 (1983), pp. 589–592. DOI: 10.1109/tmtt.1983.1131549.

[53] E. C. Sutton, G. A. Blake, C. R. Masson, and T. G. Phillips. "Molecular line survey of Orion A from 215 to 247 GHz". In: *The Astrophysical Journal Supplement Series* 58 (July 1985), p. 341. DOI: 10.1086/191045.

[54] T.G. Phillips and J. Keene. "Submillimeter astronomy (heterodyne spectroscopy)". In: *Proceedings of the IEEE* 80.11 (1992), pp. 1662–1678. DOI: 10.1109/5.175248.

[55] Hans Peter Roeser, Johannes Schmid-Burgk, Gerhard W. Schwaab, and Ruth U. Titz. "Airborne heterodyne receiver for the range 600 GHz to 3,000 GHz". In: *Liege International Astrophysical Colloquia*. Ed. by B. Kaldeich. Vol. 29. Liege International Astrophysical Colloquia. Dec. 1990, pp. 369–373. URL: https://ui.adsabs.harvard.edu/abs/1990LIACo..29..369R.

[56] D. J. Hollenbach and A. G. G. M. Tielens. "Photodissociation regions in the interstellar medium of galaxies". In: *Reviews of Modern Physics* 71.1 (Jan. 1999), pp. 173–230. DOI: 10.1103/revmodphys.71.173.

[57] A. Dalgarno and R. A. McCray. "Heating and Ionization of HI Regions". In: *Annual Review of Astronomy and Astrophysics* 10.1 (Sept. 1972), pp. 375–426. DOI: 10.1146/annurev.aa.10.090172.002111.

[58] J. L. Pineda, W. D. Langer, and P. F. Goldsmith. "AHerschel[C II] Galactic plane survey". In: *Astronomy & Astrophysics* 570 (Oct. 2014), A121. DOI: 10.1051/0004-6361/201424054.

[59] Javier R. Goicoechea, D. Teyssier, M. Etxaluze, P. F. Goldsmith, V. Ossenkopf, M. Gerin, E. A. Bergin, J. H. Black, J. Cernicharo, S. Cuadrado, P. Encrenaz, E. Falgarone, A. Fuente, A. Hacar, D. C. Lis, N. Marcelino, G. J. Melnick, H. S. P. Müller, C. Persson, J. Pety, M. Röllig, P. Schilke, R. Simon, R. L. Snell, and J. Stutzki. "VELOCITY-RESOLVED [C ii] EMISSION AND [C ii]/FIR MAPPING ALONG ORION WITHHERSCHEL". In: *The Astrophysical Journal* 812.1 (Oct. 2015), p. 75. DOI: 10.1088/0004-637x/812/1/75.

[60] Paul. F. Goldsmith, William D. Langer, Youngmin Seo, Jorge Pineda, Jürgen Stutzki, Christian Guevara, Rebeca Aladro, and Matthias Justen. "Interstellar Cloud Conditions Based on 63 um [O i] Emission and Absorption in W3". In: *The Astrophysical Journal* 916.1 (July 2021), p. 6. DOI: 10.3847/1538-4357/abfb69.

[61] Christophe Risacher, Rolf Gusten, Jurgen Stutzki, Heinz-Wilhelm Hubers, Denis Buchel, Urs U. Graf, Stefan Heyminck, Cornelia E. Honingh, Karl Jacobs, Bernd Klein, Thomas Klein, Christian Leinz, Patrick Putz, Nicolas Reyes, Oliver Ricken, Hans-Joachim Wunsch, Paul Fusco, and Stefan Rosner. "First Supra-THz Heterodyne Array Receivers for Astronomy With the SOFIA Observatory". In: *IEEE Transactions on Terahertz Science and Technology* 6.2 (Mar. 2016), pp. 199–211. DOI: 10.1109/tthz.2015.2508005.

[62] David M. Slocum, Elizabeth J. Slingerland, Robert H. Giles, and Thomas M. Goyette. "Atmospheric absorption of terahertz radiation and water vapor continuum effects". In: *Journal of Quantitative Spectroscopy and Radiative Transfer* 127 (Sept. 2013), pp. 49–63. DOI: 10.1016/j.jqsrt.2013.04.022.

[63] Peter Hargrave, Stafford Withington, Stefan A. Buehler, Lukas Kluft, Ben Flatman, and Prateek Kumar Dongre. "THz spectroscopy of the atmosphere for climatology and meteorology applications". In: *Next-Generation Spectroscopic Technologies X*. Ed. by Mark A. Druy, Richard A. Crocombe, Steven M. Barnett, and Luisa T. Profeta. SPIE, May 2017. DOI: 10.1117/12.2263626.

[64] P.H. Siegel. "Terahertz Technology in Biology and Medicine". In: *IEEE Transactions on Microwave Theory and Techniques* 52.10 (Oct. 2004), pp. 2438–2447. DOI: 10.1109/tmtt.2004.835916.

[65] Peter H. Siegel and Robert J. Dengler. "Terahertz heterodyne imager for biomedical applications". In: *Terahertz and Gigahertz Electronics and Photonics III*. Ed. by R. Jennifer Hwu. SPIE, Apr. 2004. DOI: 10.1117/12.540027.

[66] Karsten J Siebert, Torsten L ffler, Holger Quast, Mark Thomson, Tobias Bauer, Rainer Leonhardt, Stephanie Czasch, and Hartmut G Roskos. "All-optoelectronic continuous wave THz imaging for biomedical applications". In: *Physics in Medicine and Biology* 47.21 (Oct. 2002), pp. 3743–3748. DOI: 10.1088/0031-9155/47/21/310.

[67] Andrea Markelz, Scott Whitmire, Jay Hillebrecht, and Robert Birge. "THz time domain spectroscopy of biomolecular conformational modes". In: *Physics in Medicine and Biology* 47.21 (Oct. 2002), pp. 3797–3805. DOI: 10.1088/0031-9155/47/21/318.

[68] P Haring Bolivar, M Brucherseifer, M Nagel, H Kurz, A Bosserhoff, and R B ttner. "Label-free probing of genes by time-domain terahertz sensing". In: *Physics in Medicine and Biology* 47.21 (Oct. 2002), pp. 3815–3821. DOI: 10.1088/0031-9155/47/21/320.

[69] Leili Afsah-Hejri, Parvaneh Hajeb, Parsa Ara, and Reza J. Ehsani. "A Comprehensive Review on Food Applications of Terahertz Spectroscopy and Imaging". In: *Comprehensive Reviews in Food Science and Food Safety* 18.5 (Aug. 2019), pp. 1563–1621. DOI: 10.1111/1541-4337.12490.

[70] Michael C. Kemp, P. F. Taday, Bryan E. Cole, J. A. Cluff, Anthony J. Fitzgerald, and William R. Tribe. "Security applications of terahertz technology". In: *Terahertz for Military and Security Applications*. Ed. by R. Jennifer Hwu and Dwight L. Woolard. SPIE, Aug. 2003. DOI: 10.1117/12.500491.

[71] John F. O'Hara, Sabit Ekin, Wooyeol Choi, and Ickhyun Song. "A Perspective on Terahertz Next-Generation Wireless Communications". In: *Technologies* 7.2 (June 2019), p. 43. DOI: 10.3390/technologies7020043.

[72] Jérôme Faist. *Quantum Cascade Lasers*. Oxford University Press, Mar. 2013. DOI: 10.1093/acprof:oso/9780198528241.001.0001.

[73] Gérald Bastard and Joel Schulman. "Wave Mechanics Applied to Semiconductor Heterostructures". In: *Physics Today* 45.2 (Feb. 1992), pp. 103–105. DOI: 10.1063/1.2809545.

[74] Manuel Cardona and Fred H. Pollak. "Energy-Band Structure of Germanium and Silicon: The k·p Method". In: *Physical Review* 142.2 (Feb. 1966), pp. 530–543. DOI: 10.1103/physrev.142.530.

[75] Peter Y. Yu and Manuel Cardona. *Fundamentals of Semiconductors*. Springer Berlin Heidelberg, 2010. DOI: 10.1007/978-3-642-00710-1.

[76] Morten Willatzen and Lok C. Lew Yan Voon. *The k p Method*. Springer Berlin Heidelberg, 2009. DOI: 10.1007/978-3-540-92872-0.

[77] Evan O. Kane. "Band structure of indium antimonide". In: *Journal of Physics and Chemistry of Solids* 1.4 (Jan. 1957), pp. 249–261. DOI: 10.1016/0022-3697(57)90013-6.

[78] E. O. Kane. "Band structure of narrow gap semiconductors". In: *Narrow Gap Semiconductors Physics and Applications*. Springer Berlin Heidelberg, pp. 13–31. DOI: 10.1007/3-540-10261-2_33.

[79] G. Bastard and J. Brum. "Electronic states in semiconductor heterostructures". In: *IEEE Journal of Quantum Electronics* 22.9 (Sept. 1986), pp. 1625–1644. DOI: 10.1109/jqe.1986.1073186.

[80] Carl R Pidgeon and RN Brown. "Interband magneto-absorption and Faraday rotation in InSb". In: *Physical Review* 146.2 (1966), p. 575.

[81] Leroy L. Chang and Klaus Ploog, eds. *Molecular Beam Epitaxy and Heterostructures*. Springer Netherlands, 1985. DOI: 10.1007/978-94-009-5073-3.

[82] G Bastard. "Heterostructures and superlattices, semiconductor". In: *digital Encyclopedia of Applied Physics* (2003).

[83] DJ BenDaniel and CB Duke. "Space-charge effects on electron tunneling". In: *Physical review* 152.2 (1966), p. 683.

[84] Manfred Helm. "Chapter 1 The Basic Physics of Intersubband Transitions". In: *Semiconductors and Semimetals*. Elsevier, 1999, pp. 1–99. DOI: 10.1016/s0080-8784(08)60304-x.

[85] H. C. Liu, M. Buchanan, and Z. R. Wasilewski. "How good is the polarization selection rule for intersubband transitions?" In: *Applied Physics Letters* 72.14 (Apr. 1998), pp. 1682–1684. DOI: 10.1063/1.121151.

[86] Claude Cohen-Tannoudji, Jacques Dupont-Roc, and Gilbert Grynberg. *Photons and Atoms*. Wiley, Mar. 1997. DOI: 10.1002/9783527618422.

[87] Takeya Unuma, Masahiro Yoshita, Takeshi Noda, Hiroyuki Sakaki, and Hidefumi Akiyama. "Intersubband absorption linewidth in GaAs quantum wells due to scattering by interface roughness, phonons, alloy disorder, and impurities". In: *Journal of Applied Physics* 93.3 (Feb. 2003), pp. 1586–1597. DOI: 10.1063/1.1535733.

[88] H. C. Liu. *Intersubband transitions in quantum wells : Physics and device applications II*. San Diego, CA: Academic Press, 2000. ISBN: 9780080864648.

[89] R. Ferreira and G. Bastard. "Evaluation of some scattering times for electrons in unbiased and biased single- and multiple-quantum-well structures". In: *Physical Review B* 40.2 (July 1989), pp. 1074–1086. DOI: 10.1103/physrevb.40.1074.

[90] P.J Price. "Two-dimensional electron transport in semiconductor layers. I. Phonon scattering". In: *Annals of Physics* 133.2 (May 1981), pp. 217–239. DOI: 10.1016/0003-4916(81)90250-5.

[91] D. Y. Oberli, D. R. Wake, M. V. Klein, J. Klem, T. Henderson, and H. Morkoç. "Time-resolved Raman scattering in GaAs quantum wells". In: *Physical Review Letters* 59.6 (Aug. 1987), pp. 696–699. DOI: 10.1103/physrevlett.59.696.

[92] Chun Wang I. Chan, Asaf Albo, Qing Hu, and John L. Reno. "Tradeoffs between oscillator strength and lifetime in terahertz quantum cascade lasers". In: *Applied Physics Letters* 109.20 (Nov. 2016), p. 201104. DOI: 10.1063/1.4967244.

[93] Tsuneya Ando. "Line Width of Inter-Subband Absorption in Inversion Layers: Scattering from Charged Ions". In: *Journal of the Physical Society of Japan* 54.7 (July 1985), pp. 2671–2675. DOI: 10.1143/jpsj.54.2671.

[94] G. Scalari, C. Walther, M. Fischer, R. Terazzi, H. Beere, D. Ritchie, and J. Faist. "THz and sub-THz quantum cascade lasers". In: *Laser & Photonics Review* 3.1-2 (Feb. 2009), pp. 45–66. DOI: 10.1002/lpor.200810030.

[95] Jerome Faist, Carlo Sirtori, Federico Capasso, Loren Pfeiffer, and Ken W. West. "Phonon limited intersubband lifetimes and linewidths in a two-dimensional electron gas". In: *Applied Physics Letters* 64.7 (Feb. 1994), pp. 872–874. DOI: 10.1063/1.110980.

[96] M. Hartig, S. Haacke, P. E. Selbmann, B. Deveaud, R. A. Taylor, and L. Rota. "Efficient Intersubband Scattering via Carrier-Carrier Interaction in Quantum Wells". In: *Physical Review Letters* 80.9 (Mar. 1998), pp. 1940–1943. DOI: 10.1103/physrevlett.80.1940.

[97] M. Fischer, G. Scalari, K. Celebi, M. Amanti, Ch. Walther, M. Beck, and J. Faist. "Scattering processes in terahertz InGaAs/InAlAs quantum cascade lasers". In: *Applied Physics Letters* 97.22 (Nov. 2010), p. 221114. DOI: 10.1063/1.3504251.

[98] Jerome Faist, Federico Capasso, Carlo Sirtori, Deborah L. Sivco, and Alfred Y. Cho. "Chapter 1 Quantum Cascade Laser". In: *Semiconductors and Semimetals*. Elsevier, 1999, pp. 1–83. DOI: 10.1016/s0080-8784(08)60204-5.

[99] Amnon Yariv. *Optical Electronics*. en. Saunders College Publishing, 1991. DOI: 10.7907/5R87-M275.

[100] Carlo Sirtori, Peter Kruck, Stefano Barbieri, Philippe Collot, Julien Nagle, Mattias Beck, Jérôme Faist, and Ursula Oesterle. "GaAs/AlxGa1-xAs quantum cascade lasers". In: *Applied Physics Letters* 73.24 (Dec. 1998), pp. 3486–3488. DOI: 10.1063/1.122812.

[101] K. Ohtani and H. Ohno. "InAs-AlSb quantum cascade lasers operating at 10 um". In: *Applied Physics Letters* 82.7 (Feb. 2003), pp. 1003–1005. DOI: 10.1063/1.1545151.

[102] Sushil Kumar, Chun Wang I. Chan, Qing Hu, and John L. Reno. "Two-well terahertz quantum-cascade laser with direct intrawell-phonon depopulation". In: *Applied Physics Letters* 95.14 (Oct. 2009), p. 141110. DOI: 10.1063/1.3243459.

[103] Hermann Detz, Aaron M. Andrews, Martin A. Kainz, Sebastian Schönhuber, Tobias Zederbauer, Donald MacFarland, Michael Krall, Christoph Deutsch, Martin Brandstetter, Pavel Klang, Werner Schrenk, Karl Unterrainer, and Gottfried Strasser. "Evaluation of Material Systems for THz Quantum Cascade Laser Active Regions". In: *physica status solidi (a)* (Sept. 2018), p. 1800504. DOI: 10.1002/pssa.201800504.

[104] Lassaad Ajili, Giacomo Scalari, Nicolas Hoyler, Marcella Giovannini, and Jérôme Faist. "InGaAs/AlInAs/InP terahertz quantum cascade laser". In: *Applied Physics Letters* 87.14 (Oct. 2005), p. 141107. DOI: 10.1063/1.2081122.

[105] Jérôme Faist, Federico Capasso, Carlo Sirtori, Deborah L. Sivco, James N. Baillargeon, Albert L. Hutchinson, Sung-Nee G. Chu, and Alfred Y. Cho. "High power mid-infrared quantum cascade lasers operating above room temperature". In: *Applied Physics Letters* 68.26 (June 1996), pp. 3680–3682. DOI: 10.1063/1.115741.

[106] H. Luo, S. R. Laframboise, Z. R. Wasilewski, G. C. Aers, H. C. Liu, and J. C. Cao. "Terahertz quantum-cascade lasers based on a three-well active module". In: *Applied Physics Letters* 90.4 (Jan. 2007), p. 041112. DOI: 10.1063/1.2437071.

[107] Daniel Hofstetter, Mattias Beck, Thierry Aellen, and Jérôme Faist. "High-temperature operation of distributed feedback quantum-cascade lasers at 5.3 um". In: *Applied Physics Letters* 78.4 (Jan. 2001), pp. 396–398. DOI: 10.1063/1.1340865.

[108] Benjamin S. Williams. "Terahertz quantum-cascade lasers". In: *Nature Photonics* 1.9 (Sept. 2007), pp. 517–525. DOI: 10.1038/nphoton.2007.166.

[109] Jérôme Faist, Mattias Beck, Thierry Aellen, and Emilio Gini. "Quantum-cascade lasers based on a bound-to-continuum transition". In: *Applied Physics Letters* 78.2 (Jan. 2001), pp. 147–149. DOI: 10.1063/1.1339843.

[110] Giacomo Scalari, Lassaad Ajili, Jérôme Faist, Harvey Beere, Edmund Linfield, David Ritchie, and Giles Davies. "Far-infrared (87um) bound-to-continuum quantum-cascade lasers operating up to 90 K". In: *Applied Physics Letters* 82.19 (May 2003), pp. 3165–3167. DOI: 10.1063/1.1571653.

[111] Lassaad Ajili, Giacomo Scalari, Marcella Giovannini, Nicolas Hoyler, and Jérôme Faist. "Doping in quantum cascade lasers. II. GaAs/Al0.15Ga0.85As terahertz devices". In: *Journal of Applied Physics* 100.4 (Aug. 2006), p. 043102. DOI: 10.1063/1.2234805.

[112] John David Jackson. *Classical Electrodynamics*. WILEY, Aug. 1, 1998. 832 pp. ISBN: 047130932X. URL: https://www.ebook.de/de/product/3240907/john_david_jackson_classical_electrodynamics.html.

[113] Stephen Kohen, Benjamin S. Williams, and Qing Hu. "Electromagnetic modeling of terahertz quantum cascade laser waveguides and resonators". In: *Journal of Applied Physics* 97.5 (Mar. 2005), p. 053106. DOI: 10.1063/1.1855394.

[114] Michel Rochat, Lassaad Ajili, Harald Willenberg, Jérôme Faist, Harvey Beere, Giles Davies, Edmund Linfield, and David Ritchie. "Low-threshold terahertz quantum-cascade lasers". In: *Applied Physics Letters* 81.8 (Aug. 2002), pp. 1381–1383. DOI: 10.1063/1.1498861.

[115] Mikhail A. Belkin, Jonathan A. Fan, Sahand Hormoz, Federico Capasso, Suraj P. Khanna, Mohamed Lachab, A. G. Davies, and Edmund H. Linfield. "Terahertz quantum cascade lasers with copper metal-metal waveguides operating up to 178 K". In: *Optics Express* 16.5 (2008), p. 3242. DOI: 10.1364/oe.16.003242.

[116] Martin Franckie, Lorenzo Bosco, Elena Mavrona, Andreas Wacker, and Jerome Faist. "THz Quantum Cascade Lasers Operating up to 210 K". In: *2019 44th International Conference on Infrared, Millimeter, and Terahertz Waves (IRMMW-THz)*. IEEE, Sept. 2019. DOI: 10.1109/irmmw-thz.2019.8874366.

[117] Matthias Justen, Christopher Bonzon, Keita Ohtani, Mathias Beck, Urs Graf, and Jerome Faist. "2D patch antenna array on a double metal quantum cascade laser with greater than 90 percent coupling to a Gaussian beam and selectable facet transparency at 1.9THz". In: *Optics Letters* 41.19 (Sept. 2016), p. 4590. DOI: 10.1364/ol.41.004590.

[118] U. Senica, E. Mavrona, T. Olariu, A. Forrer, M. Shahmohammadi, M. Beck, J. Faist, and G. Scalari. "An antipodal Vivaldi antenna for improved far-field properties and polarization manipulation of broadband terahertz quantum cascade lasers". In: *Applied Physics Letters* 116.16 (Apr. 2020), p. 161105. DOI: 10.1063/5.0004038.

[119] Minoru Yamada. *Theory of Semiconductor Lasers*. Springer Japan, 2014. DOI: 10.1007/978-4-431-54889-8.

[120] Markus Geiser, Christian Pflügl, Alexey Belyanin, Qi Jie Wang, Nanfang Yu, Tadanaka Edamura, Masamichi Yamanishi, Hirofumi Kan, Milan Fischer, Andreas Wittmann, Jérôme Faist, and Federico Capasso. "Gain competition in dual wavelength quantum cascade lasers". In: *Optics Express* 18.10 (Apr. 2010), p. 9900. DOI: 10.1364/oe.18.009900.

[121] Ariel Gordon, Christine Y. Wang, L. Diehl, F. X. Kärtner, A. Belyanin, D. Bour, S. Corzine, G. Höfler, H. C. Liu, H. Schneider, T. Maier, M. Troccoli, J. Faist, and Federico Capasso. "Multimode regimes in quantum cascade lasers: From coherent instabilities to spatial hole burning". In: *Physical Review A* 77.5 (May 2008). DOI: 10.1103/physreva.77.053804.

[122] D. A. B. Miller, D. S. Chemla, T. C. Damen, A. C. Gossard, W. Wiegmann, T. H. Wood, and C. A. Burrus. "Band-Edge Electroabsorption in Quantum Well Structures: The Quantum-Confined Stark Effect". In: *Physical Review Letters* 53.22 (Nov. 1984), pp. 2173–2176. DOI: 10.1103/physrevlett.53.2173.

[123] Jrme Faist, Federico Capasso, Carlo Sirtori, Deborah L. Sivco, Albert L. Hutchinson, and Alfred Y. Cho. "Laser action by tuning the oscillator strength". In: *Nature* 387.6635 (June 1997), pp. 777–782. DOI: 10.1038/42872.

[124] L. Andrea Dunbar, Romuald Houdré, Giacomo Scalari, Lorenzo Sirigu, Marcella Giovannini, and Jérôme Faist. "Small optical volume terahertz emitting microdisk quantum cascade lasers". In: *Applied Physics Letters* 90.14 (Apr. 2007), p. 141114. DOI: 10.1063/1.2719674.

[125] Jérome Faist, Claire Gmachl, Federico Capasso, Carlo Sirtori, Deborah L. Sivco, James N. Baillargeon, and Alfred Y. Cho. "Distributed feedback quantum cascade lasers". In: *Applied Physics Letters* 70.20 (May 1997), pp. 2670–2672. DOI: 10.1063/1.119208.

[126] M. I. Amanti, M. Fischer, G. Scalari, M. Beck, and J. Faist. "Low-divergence single-mode terahertz quantum cascade laser". In: *Nature Photonics* 3.10 (Sept. 2009), pp. 586–590. DOI: 10.1038/nphoton.2009.168.

[127] Peter Fuchs, Jochen Friedl, Sven Höfling, Johannes Koeth, Alfred Forchel, Lukas Worschech, and Martin Kamp. "Single mode quantum cascade lasers with shallow-etched distributed Bragg reflector". In: *Optics Express* 20.4 (Feb. 2012), p. 3890. DOI: 10.1364/oe.20.003890.

[128] Stefano Barbieri, Marco Ravaro, Pierre Gellie, Giorgio Santarelli, Christophe Manquest, Carlo Sirtori, Suraj P. Khanna, Edmund H. Linfield, and A. Giles Davies. "Coherent sampling of active mode-locked terahertz quantum cascade lasers and frequency synthesis". In: *Nature Photonics* 5.5 (Apr. 2011), pp. 306–313. DOI: 10.1038/nphoton.2011.49.

[129] D. G. Revin, M. Hemingway, Y. Wang, J. W. Cockburn, and A. Belyanin. "Active mode locking of quantum cascade lasers in an external ring cavity". In: *Nature Communications* 7.1 (May 2016). DOI: 10.1038/ncomms11440.

[130] Mario Bertolotti, Victor Bogdanov, Aldo Ferrari, Andrei Jascow, Natalia Nazorova, Alexander Pikhtin, and Luigi Schirone. "Temperature dependence of the refractive index in semiconductors". In: *Journal of the Optical Society of America B* 7.6 (June 1990), p. 918. DOI: 10.1364/josab.7.000918.

[131] Asif Ahmed, Orchi Hassan, Md. Shahadat Hasan Sohel, Fariah Hayee, Rafatul Faria, and Muhammad Anisuzzaman Talukder. "Quantum cascade laser wavelength tuning due to temperature-dependent index of refraction". In: *2012 Photonics Global Conference (PGC)*. IEEE, Dec. 2012. DOI: 10.1109/pgc.2012.6457941.

[132] L. Schrottke, X. Lü, B. Röben, K. Biermann, M. Wienold, H. Richter, H.-W. Hübers, and H. T. Grahn. "Intrinsic frequency tuning of terahertz quantum-cascade lasers". In: *Journal of Applied Physics* 123.21 (June 2018), p. 213102. DOI: 10.1063/1.5024480.

[133] A. Bismuto, R Terazzi, M. Beck, and Jerome Faist. "Electrically tunable, high performance quantum cascade laser". In: *Applied Physics Letters* 96.14 (Apr. 2010), p. 141105. DOI: 10.1063/1.3377008.

[134] Ferdous K. Khan and Daniel T. Cassidy. "Widely tunable coupled-cavity semiconductor laser". In: *Applied Optics* 48.19 (June 2009), p. 3809. DOI: 10.1364/ao.48.003809.

[135] K. Pierściński, D. Pierścińska, M. Pluska, P. Gutowski, I. Sankowska, P. Karbownik, A. Czerwinski, and M. Bugajski. "Room temperature, single mode emission from two-section coupled cavity InGaAs/AlGaAs/GaAs quantum cas-

cade laser". In: *Journal of Applied Physics* 118.13 (Oct. 2015), p. 133103. DOI: 10.1063/1.4932141.

[136] Iman Kundu, Paul Dean, Alexander Valavanis, Li Chen, Lianhe Li, John E. Cunningham, Edmund H. Linfield, and A. Giles Davies. "Quasi-continuous frequency tunable terahertz quantum cascade lasers with coupled cavity and integrated photonic lattice". In: *Optics Express* 25.1 (Jan. 2017), p. 486. DOI: 10.1364/oe.25.000486.

[137] Xiaoqiong Qi, Iman Kundu, Paul Dean, Gary Agnew, Thomas Taimre, Alexander Valavanis, Andrew T. Grier, Edmund H. Linfield, Alexander Giles Davies, Dragan Indjin, and Aleksandar D. Rakic. "Mode Selection and Tuning Mechanisms in Coupled-Cavity Terahertz Quantum Cascade Lasers". In: *IEEE Journal of Selected Topics in Quantum Electronics* 23.4 (July 2017), pp. 1–12. DOI: 10.1109/jstqe.2017.2668600.

[138] Michael G. Littman and Harold J. Metcalf. "Spectrally narrow pulsed dye laser without beam expander". In: *Applied Optics* 17.14 (July 1978), p. 2224. DOI: 10.1364/ao.17.002224.

[139] Qi Qin, Benjamin S. Williams, Sushil Kumar, John L. Reno, and Qing Hu. "Tuning a terahertz wire laser". In: *Nature Photonics* 3.12 (Nov. 2009), pp. 732–737. DOI: 10.1038/nphoton.2009.218.

[140] Qi Qin, John L. Reno, and Qing Hu. "MEMS-based tunable terahertz wire-laser over 330 GHz". In: *Optics Letters* 36.5 (Feb. 2011), p. 692. DOI: 10.1364/ol.36.000692.

[141] B.R. Bennett, R.A. Soref, and J.A. Del Alamo. "Carrier-induced change in refractive index of InP, GaAs and InGaAsP". In: *IEEE Journal of Quantum Electronics* 26.1 (1990), pp. 113–122. DOI: 10.1109/3.44924.

[142] Martin Hempel, Benjamin Röben, Lutz Schrottke, Heinz-Wilhelm Hübers, and Holger T. Grahn. "Fast continuous tuning of terahertz quantum-cascade lasers by rear-facet illumination". In: *Applied Physics Letters* 108.19 (May 2016), p. 191106. DOI: 10.1063/1.4949528.

[143] T. Alam, M. Wienold, X. Lü, K. Biermann, L. Schrottke, H. T. Grahn, and H.-W. Hübers. "Wideband, high-resolution terahertz spectroscopy by light-induced frequency tuning of quantum-cascade lasers". In: *Optics Express* 27.4 (Feb. 2019), p. 5420. DOI: 10.1364/oe.27.005420.

[144] T. Alam, M. Wienold, X. Lü, K. Biermann, L. Schrottke, H. T. Grahn, and H.-W. Hübers. "Frequency and power stabilization of a terahertz quantum-cascade laser using near-infrared optical excitation". In: *Optics Express* 27.25 (Dec. 2019), p. 36846. DOI: 10.1364/oe.27.036846.

[145] L. Bosco, C. Bonzon, K. Ohtani, M. Justen, M. Beck, and J. Faist. "A patch-array antenna single-mode low electrical dissipation continuous wave terahertz quantum cascade laser". In: *Applied Physics Letters* 109.20 (Nov. 2016), p. 201103. DOI: 10.1063/1.4967836.

[146] Etienne Perret, Nicolas Zerounian, Sylvain David, and Frédéric Aniel. "Complex permittivity characterization of benzocyclobutene for terahertz applications". In: *Microelectronic Engineering* 85.11 (Nov. 2008), pp. 2276–2281. DOI: 10.1016/j.mee.2008.07.008.

[147] H. Zhang, Giacomo Scalari, Jérôme Faist, L. Andrea Dunbar, and Romuald Houdré. "Design and fabrication technology for high performance electrical pumped terahertz photonic crystal band edge lasers with complete photonic band gap". In: *Journal of Applied Physics* 108.9 (Nov. 2010), p. 093104. DOI: 10.1063/1.3476565.

[148] R.A. Khabibullin, N.V. Shchavruk, D.S. Ponomarev, D.V. Ushakov, A.A. Afonenko, K.V. Maremyanin, O.Yu. Volkov, V.V. Pavlovskiy, and A.A. Dubinov. "The operation of THz quantum cascade laser in the region of negative differential resistance". In: *Opto-Electronics Review* 27.4 (Dec. 2019), pp. 329–333. DOI: 10.1016/j.opelre.2019.11.002.

[149] Benjamin Röben, Xiang Lü, Klaus Biermann, Lutz Schrottke, and Holger T Grahn. "Effective group dispersion of terahertz quantum-cascade lasers". In: *Journal of Physics D: Applied Physics* 54.2 (Oct. 2020), p. 025110. DOI: 10.1088/1361-6463/abbde3.

[150] Wolfgang Parz, Thomas Müller, Juraj Darmo, Maximilian Austerer, Gottfried Strasser, Luke Wilson, John Cockburn, Andrey Krysa, John Roberts, and Karl Unterrainer. "Intersubband gain-induced dispersion". In: *Optics Letters* 34.2 (Jan. 2009), p. 208. DOI: 10.1364/ol.34.000208.

[151] Vittorio Degiorgio. "Phase shift between the transmitted and the reflected optical fields of a semireflecting lossless mirror is pi/2". In: *American Journal of Physics* 48.1 (Jan. 1980), pp. 81–81. DOI: 10.1119/1.12238.

Appendix A.

Microscopy Images

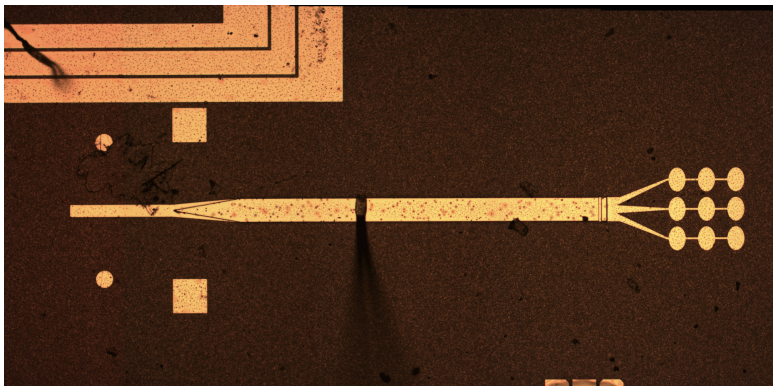

Figure A.0.1.: Microscopy image of QCL 5

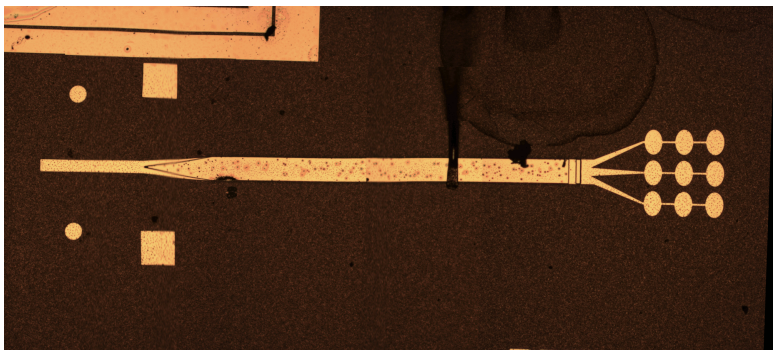

Figure A.0.2.: QCL 6 is comparatively clean around the tuning section. Some image distortion on the left side is an optical artifact from the microscopy.

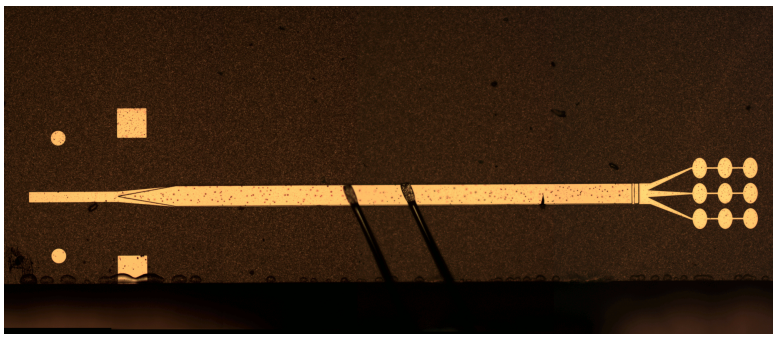

Figure A.0.3.: Microscopy image of QCL 7.

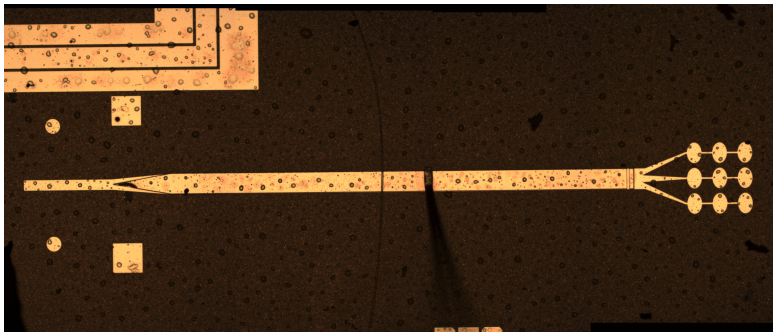

Figure A.0.4.: QCL 9 (shown here) and QCL 10 are widely covered in large spots.

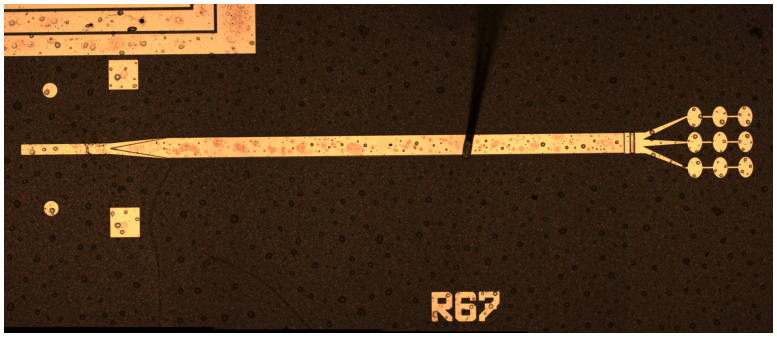

Figure A.0.5.: Microscopy image of QCL 10.

Appendix B.

QCL Measurements

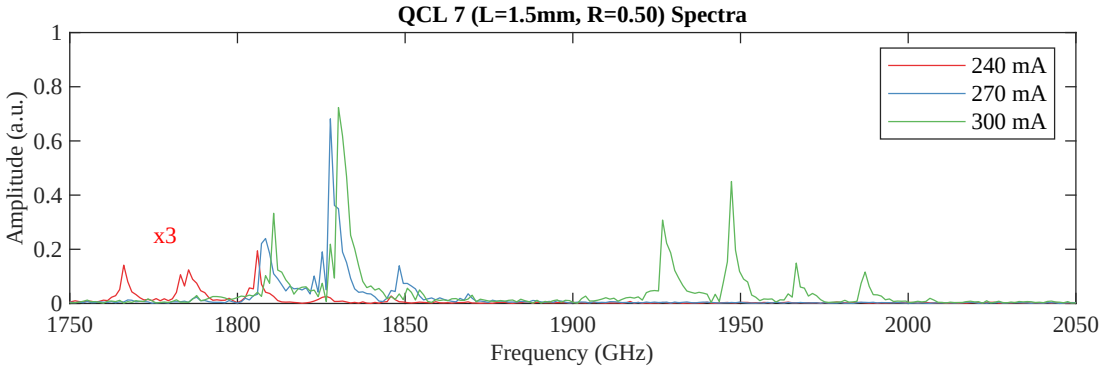

Figure B.0.1.: A range from 1.85 THz to 1.92 THz is found in the QCL 7 spectra where no lasing occurs. Mode spacing is 20.3 GHz.

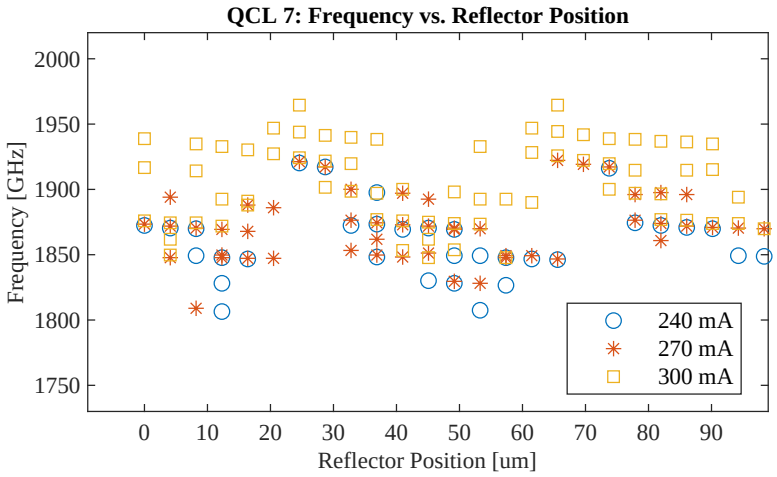

Figure B.0.2.: This dataset is less educational with many datapoints scattered between modes and generally disordered.

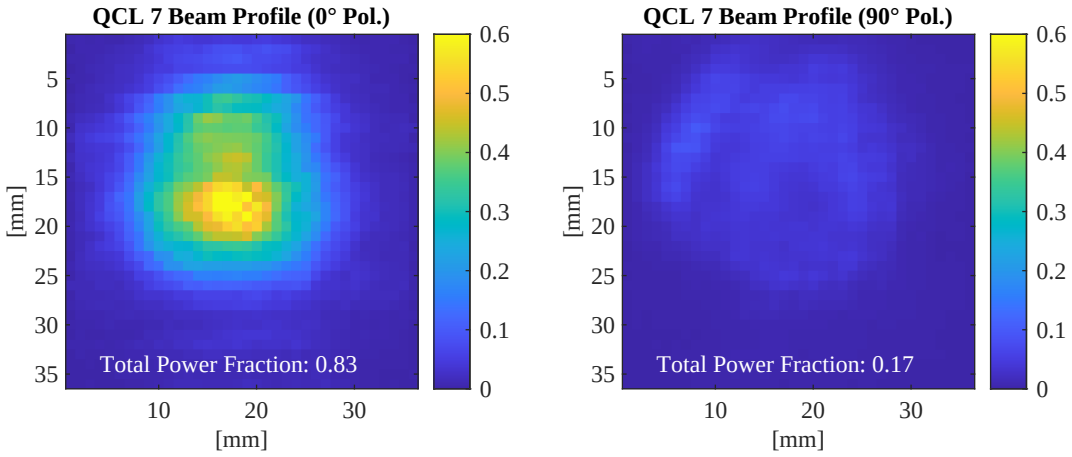

Figure B.0.3.: Far field of QCL 7.

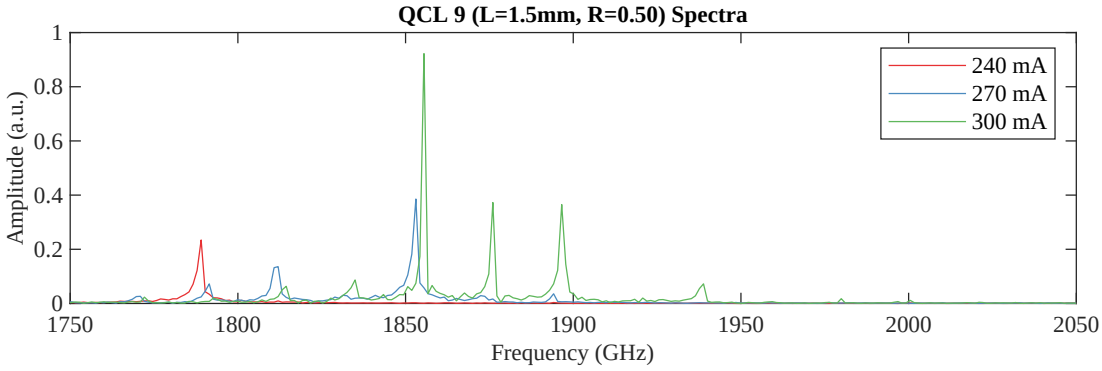

Figure B.0.4.: Spectra of QCL 9. Mode spacing is 20.7 GHz.

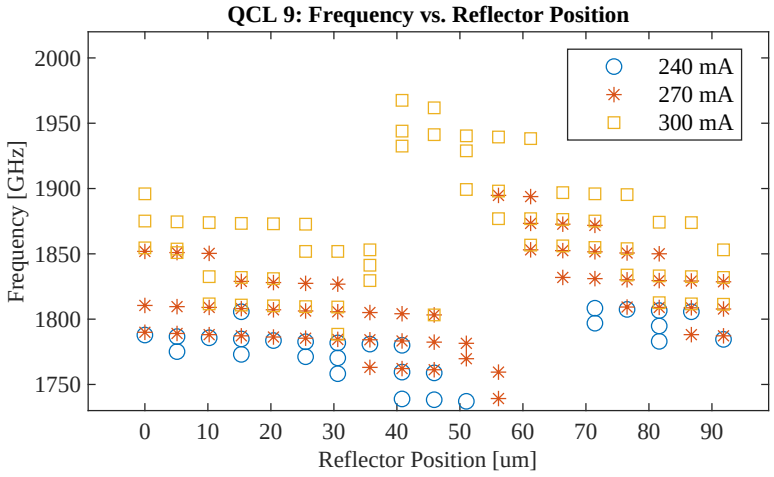

Figure B.0.5.: Modal gain modulation is the main effect of the reflector position with ca. 7 GHz of continuous tuning.

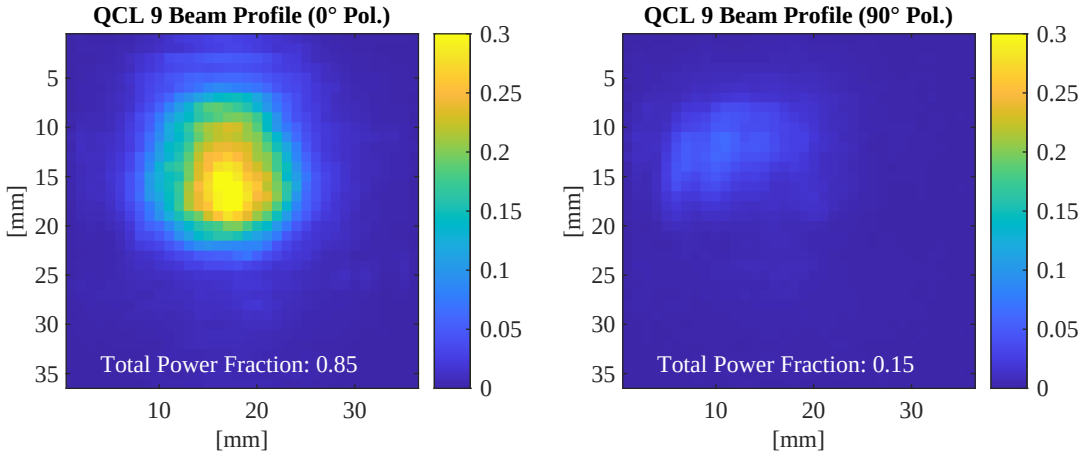

Figure B.0.6.: No surprises in the Far field of this device. 15% of the emitted power is found in the "wrong" polarization.

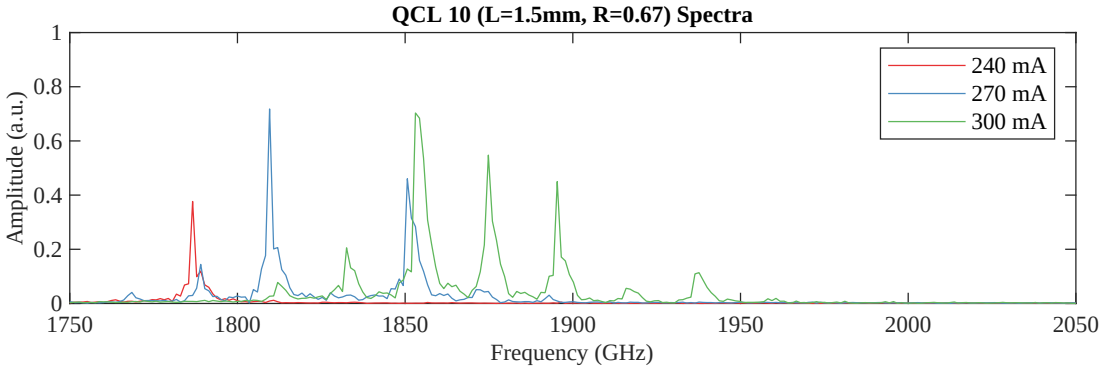

Figure B.0.7.: Spectra of QCL 10. Mode spacing is 20.2 GHz.

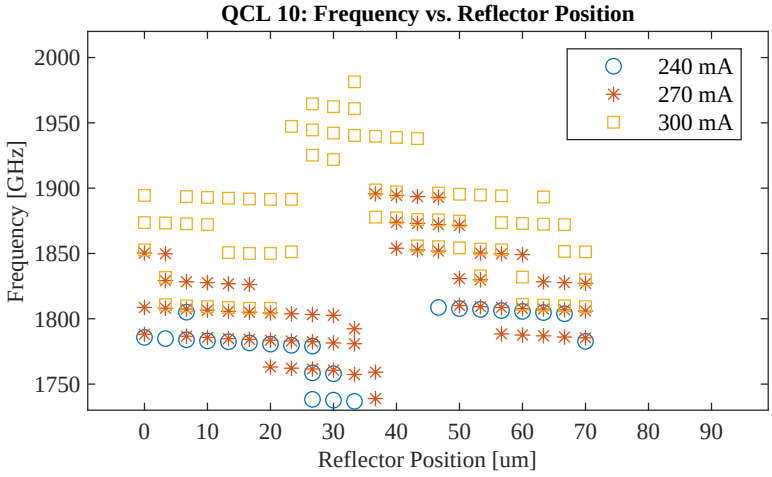

Figure B.0.8.: Similar to QCL 9 on the same chip continuous tuning of a few GHz is observed within lasing parameters.

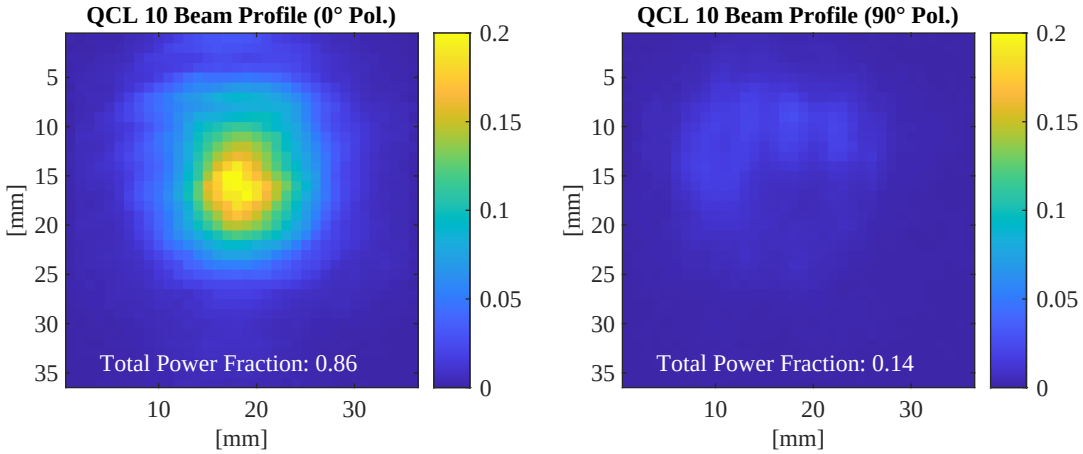

Figure B.0.9.: Far field of QCL 10.